2013

Interaction Of The Cyclonic Winds With The Infrasonic Signal Generated By A Large Maritime Storm

Philip Stephen Blom
University of Mississippi

Interaction of the Cyclonic Winds with the Infrasonic Signal Generated by a Large Maritime Storm

A Dissertation
presented in partial fulfillment of requirements
for the degree of Doctor of Philosophy
in the Department of Physics and Astronomy
The University of Mississippi

by PHILIP S. BLOM

May, 2013

ABSTRACT

The collision of counter propagating ocean surface waves of like periods is known to produce an infrasonic signal termed a microbarom. It has been suggested that microbaroms associated with large maritime storms are generated far from the storm center at a location in which the storm swell and background swell have equal period and are counter-propagating. It is shown in this work that the interaction of the atmospheric microbarom signal generated by a large maritime storm with the cyclonic winds of the storm results in a characteristic acoustic signal far from the storm which could potentially be used to estimate storm intensity from infrasonic measurements.

Numerical propagation modeling has predicted that one particular characteristic, back azimuth, might be analyzed to estimate storm intensity. For a storm in the open Atlantic, microbaroms which have strongly interacted with the storm winds are predicted to have back azimuths oriented towards the storm center and are only expected to be observed in a localized region to the northwest of the storm. Microbaroms which have weakly interacted with the storm are predicted to have back azimuths oriented towards the source region and are expected to be observed most clearly from the south of the storm. The size of the region in which the strongly interacting signal is observed has been found to be strongly dependent on wind speeds in the storm center and therefore observation of this signal might allow estimation of storm intensity from infrasonic data.

Acoustic data has been collected during the 2010 and 2011 Atlantic hurricane seasons using infrasound arrays deployed in Florida, North and South Carolina, New Jersey, New York, and Connecticut. Observations of microbaroms which have not interacted strongly with the storm are in agreement with the prediction that the location of the microbarom source region is far from the storm center. Additionally, observations of microbaroms with back azimuths such that interaction with the storm is likely are in strong agreement with predictions from propagation modeling.

DEDICATION

This dissertation is dedicated to my grandmother, Geraldine J. Froelicher Wolff, who instilled in me a love and appreciation for knowledge and education.

ACKNOWLEDGEMENTS

I would like to thank Dr Roger Waxler, Dr William Garth Frazier, and Claus Hetzer for their guidance and assistance in this research. Additionally, I would thank my wife, Sarah, for her support and assistance in preparing and editing this document and her constant patience and support during my years working towards this goal. Finally, I would thank Tom and Beth Blom and Dave and Pam Szymanski for their support and encouragement.

TABLE OF CONTENTS

LIST OF TABLES

LIST OF FIGURES

CHAPTER 1

INTRODUCTION

Infrasonics involves the study of acoustic radiation at frequencies below the range of human hearing. Acoustic energy refers to the presence of elastic longitudinal waves in a fluid. Displacement of a boundary surface or localized compression or rarefaction causes a disturbance of the particle locations within the fluid. Such displacement results in a restoring force on the particles which can produce traveling waves in an unbounded fluid or standing waves in a contained fluid. The human ear can detect sound with frequencies as low as 20 Hz, and the human body can sense vibrations at even lower frequencies. This 20 Hz threshold defines the upper limit of infrasonic frequencies. Infrasound can be generated by both natural and anthropomorphic sources. Severe weather, surf, avalanches, earthquakes, bolides, aurorae, and lightning are known to produce natural infrasound. Sonic booms, chemical and nuclear explosions, and large machinery are known sources of man-made infrasound.

The Objective of This Work

The goal of this project is to extend the understanding of the continuous infrasonic signals, termed microbaroms, generated by large maritime storms in the open ocean and to develop a physical model for the interaction between the microbaroms and the strong winds of the storm. The general mathematical theory describing microbarom generation by colliding ocean waves has been established since the 1950's and is straightforward [1]. However, the surface wave structure around a large maritime storm can be complex and highly energetic leading to difficulty in identifying how and where the microbaroms associated with a large storm are generated [2, 3]. Here, the microbarom generating model suggested by Hetzer et al. has been examined using an axially

symmetric storm wind model to approximate the surface wave structure beneath the storm [3]. It is expected that the interaction of the storm induced swell with the background swell will produce the counter propagating waves required to generate microbaroms at a location far from the storm center.

The microbaroms propagate away from this source region in all directions. The energy that propagates away from the storm center interacts with the weaker storm winds in the region, while the energy that propagates towards the storm center interacts with the much stronger wind field around the storm eye. The propagation of the microbaroms from the source region through the storm winds has not been investigated previously and is the primary focus of this research. Geometric acoustics has been used to model the propagation of the microbaroms through the storm wind structure and measure the refraction effects due to the strong wind gradients in the storm center. Strong horizontal refraction is predicted for microbaroms which propagate near the eye column and the severity of the refraction has been found to be dependent on storm intensity. From this result, it is expected that by monitoring this refraction one could infer some measure of the storm intensity from the characteristics of the acoustic signal.

The signal far from the storm is expected to contain some contribution which has weakly interacted with the storm wind field away from the eye and, possibly, a second contribution which has been strongly refracted by the storm winds around the eye. The back azimuths of these two signals are expected to differ by a measurable separation far from the storm. Therefore, by monitoring the back azimuth of microbaroms observed far from the storm, it could be possible to extract information regarding the storm's wind structure from the signal characteristics. The propagation model predictions have been compared with observations taken during the 2010 and 2011 Atlantic hurricane seasons. These experimental results have been promising, however, additional observations are necessary in order to better understand if the model developed here is an accurate physical description of the interaction. Recommendations are provided regarding array design and data processing for future experiments designed to more thoroughly investigate the storm produced microbarom signal.

Alternate methods to probe the interior structure of a large maritime are difficult and can be dangerous. The first direct measurements of a large maritime storm were performed by an American Army Air Corps pilot, Joseph Duckworth, who flew into the eye of a hurricane on July

27th, 1943 [4]. Since that time, instrumentation has advanced to include improved reconnaissance aircraft, land-based radar, and weather satellites. The physical model describing the microbarom interaction with the storm developed here provides the framework to develop a method to extract information regarding the wind structure in the boundary layer of the storm using the characteristics of the infrasonic signal far from the storm. Such information is not intended to replace any of these other data sources, but to provide an additional source of data regarding the storm structure.

The predictive tools used to forecast maritime storm dynamics have advanced substantially in the past decades, however the accuracy of such predictions are limited by the accuracy of the measurements used to parameterize the predictive models. One of the most difficult phenomena to predict in the dynamics of a large maritime storm is a rapid intensification such as that observed by a number of strong storms which made landfall in the United States in past decades [5]. Such phenomena could likely be monitored using the microbarom signal. Unlike the periodic measurements taken by aircraft, the microbarom signal which interacts with the internal wind structure of a hurricane can provide a continuous, near-real-time measure of the storm interior which can be analyzed quickly. Additionally, the primary delay involved is due to propagation time. As a large storm approaches a coast-line, the propagation distance to infrasonic arrays along the coast decreases and the infrasonic monitoring becomes even closer to a real-time data source.

Acoustic Propagation and Past Microbarom Research

In a uniform medium, acoustic energy radiates spherically away from a source. Variations in the temperature and flow velocity of the medium can greatly alter the propagation of the acoustic signal [6, 7, 8, 9]. The speed at which sound propagates through a stationary, ideal gas is given by the thermodynamic sound speed $c = \sqrt{\gamma RT}$, where γ is the adiabatic index, R is the universal gas constant, and T is the temperature of the gas in Kelvin [6, 7]. For reference, $\gamma R = 402.8 \frac{\mathrm{m}^2}{\mathrm{s}^2 \mathrm{K}}$ in air. In a medium which varies in temperature, an acoustic wave is deformed due to some portions of the wavefront traveling faster than others. Consider, as an example, a stratified atmosphere. In the case that temperature increases with altitude, the portion of the wavefront slightly higher in the atmosphere travels faster and the sound is refracted downward. Alternately, if temperature decreases with altitude the portion of the wavefront slightly higher up will travel slower and the

sound is refracted upward. Similar refraction occurs in the case of changes in fluid flow speed in the direction that the wave is propagating.

The result of this refraction can be measured using an array of microphones. As an acoustic signal moves across the array, it arrives at each microphone with some delay in time due to its finite propagation velocity. The time delays between multiple pairs of microphones can be used to estimate the speed at which the signal moved across the array, termed its trace velocity, and the direction in which it was traveling, termed its direction of arrival (DOA) or back azimuth. The vertical refraction of the signal will produce some change in the angle at which the signal arrives at the ground, which influences its trace velocity. Horizontally, the acoustic signal can be displaced by strong cross winds or refracted by horizontal gradients in the winds, producing differences between the back azimuth and the azimuth to the true source location. In most cases, horizontal gradients in the atmosphere are too weak to produce any significant propagation effects and most horizontal propagation effects are due to cross winds. However, in the case of a large maritime storm, the large wind gradients near the eye wall are expected to produce strong horizontal refraction.

In addition to the refraction of the sound, acoustic energy is absorbed by the propagation medium resulting in attenuation of the signal as it propagates. In general, this attenuation is approximately proportional to $\frac{1}{\sqrt{f}}$ where f is the frequency of the acoustic energy [6]. Because of this dependence, lower frequency signals, such as those in infrasonics, are very weakly attenuated as they propagate in the atmosphere and can be detected at very large distances from the source. Attenuation of sound by the propagation medium is due to two types of processes: classical effects and relaxation effects. Classical effects include molecular diffusion, internal friction, and heat conduction in the fluid [6]. In the case of relaxation effects, some of the acoustic energy is lost in the kinetic, vibrational, and rotational energy of the particles in the fluid [6].

The microbarom signal of interest to this project is a continuous form of infrasonic energy produced by active regions of the ocean surface which radiates into the ocean and atmosphere. Typical amplitudes of the microbarom signal are $\sim 0.1 \frac{\text{Pa}}{\sqrt{\text{Hz}}}$ and $\sim 100 \frac{\text{Pa}}{\sqrt{\text{Hz}}}$ for atmospheric and oceanic microbaroms respectively. Microbaroms typically have a maximum amplitude at a frequency of 0.2 Hz with energy distributed between 0.15 and 0.3 Hz. This band is in the detection range for 1-kiloton nuclear explosion tests and therefore the microbarom signal complicates observation of such signals [10]. Applications have been proposed by a number of scientists to use the micro-

barom background as a passive probe of ocean surface activity, weather phenomena, and acoustic tomography of the atmosphere [11, 12, 13, 14, 15, 16].

The study of microbaroms and microseisms, a seismic signal now known to be generated by the same mechanism, began with observations by Benioff and Gutenberg in 1939 and Baird in 1940 [17, 18]. A mathematical theory for the generation of microseisms was developed several years later during the 1950's by Longuet-Higgins [1]. Additional research showed correlations of the locations of microbarom and microseism sources [19, 20, 21]. Comparison of these correlations with meteorological and oceanographic data lead to speculation that strong storms over the open ocean and the resulting active ocean surface dynamics are a driving mechanism of both microbaroms and microseisms.

A more thorough derivation of the generating mechanism for microbaroms and microseisms was presented by Waxler and Gilbert in 2006 [22]. The mathematical theory describing the radiation of atmospheric and ocean microbaroms is constructed by expanding the equations of fluid mechanics at the air-water interface to second order in small perturbations. At linear order, the interface conditions result in evanescent perturbations and no acoustic radiation occurs. At second order a wave equation is found with a source term containing the linear order velocity (that is, a source term which is only non-zero near the interface) [22]. From this result, it can be shown that microbaroms are excited by the collision of ocean surface waves of equal period [22, 1, 23].

As mentioned previously, infrasonic signal observed some distance away from the the source are dependent on the propagation medium and the characteristics of the source. The strength and direction of the wind in the stratosphere greatly affects the strength of the microbarom signal detected at at given receiver location. Some regions of the oceans continuously generate microbaroms due to colliding currents or interaction with continental shelves and coast lines. A number of studies have been published using microbaroms to monitor seasonal variations in the atmospheric winds and temperature [12, 24, 14, 16, 15, 13]. Studies published by Donn and Rind in the 1970s demonstrated a correlation of microbarom amplitude variability to solar tide fluctuations and stratospheric warmings using microbaroms generated by storm sources from the North Atlantic [12, 16]. More recent studies by Le Pichon et al. used microbarom signals to study winds over horizontal distances of several thousand kilometers [14]. Seasonal trends in observations have been studied using a geometric propagation model and high-resolution atmosphere specifications

by Dessa et.al [25].

It has been found by Walker that the strength of the microbarom source region is critically important in predicting observations. During the boreal winter months in the North Pacific, open ocean and near-coastal microbaroms can be produced and observed regardless of propagation direction due to the high energy levels of the signal. During the summer months, the energy level decreases and observations are limited to arrays downwind in the stratospheric duct [26]. Walker has demonstrated that there is a high correlation between inferred microbarom source regions and counter propagating waves predicted by the NOAA Wave Watch 3 (NWW3) directional wave spectra from bouy locations. It is proposed that the microbarom observations could be used to validate the results of NWW3 [26].

In addition to the model proposed by Hetzer et al., research in 2011 by Stopa et al. has suggested that microbaroms can be generated by a large, stationary maritime storm regardless of ambient conditions due to the convergence of the cyclonic waves near the storm center. For a non-stationary storm, the forward motion of the storm produced opposing waves from the front and rear quadrants which radiate microbaroms [27]. Applying this method to NWW3 data for cyclones Felicia and Neki from 2009, Stopa et al. have been able to recreate the observed tropical cyclone and ambient wave conditions for microbarom sources due to the storms and predict microbarom source regions around the storms [28]. The resulting model predicts the possibility of microbarom sources ahead and alongside the storm due to the interaction of the storm swell and ambient swell. The model proposed by Stopa et al. predicts the microbarom source theorized by Hetzer et al., however, it also allows for a large number of additional sources to form depending on ambient ocean swell, storm intensity, and storm velocity. In this work, the model proposed by Hetzer et al., will be discussed and used to model the generation of microbaroms by a large maritime storm.

Outline of the Thesis

The structuring of the work presented here is as follows. Chapter 2 contains a derivation of the generating mechanism of infrasonic energy by colliding sea surface waves and an explanation of how such a wave structure is generated by a large maritime storm. The exact location of the source region relative to the storm center can be predicted using these results. Chapter 3

includes a background on the approximation of geometric acoustics used to model the propagation of the microbarom signal. Using the results of this propagation model, an in depth discussion of the predicted interaction of the infrasonic energy with the storm winds in both two and three dimensional models is presented. Chapter 4 summarizes the deployments of infrasonic microphones along the Atlantic coast of the United States along with overviews of the 2010 and 2011 Atlantic Hurricane seasons. The data processing methods developed and used in this project are discussed in Chapter 5 including a robust multi-signal classification method with statistical model selection, a most simplified processing method for sparse arrays, and recommendations regarding future deployments. Analysis of the data collected during 2010 and 2011 is summarized in Chapter 6. Finally, conclusions and recommendations for future work related to studies of microbaroms generated by and interacting with large maritime storms are listed in Chapter 7.

CHAPTER 2

GENERATION OF MICROBAROMS BY A LARGE MARITIME STORM

Longuet-Higgins developed a theory for the generation of oceanic microbaroms and, through interactions with the ocean floor, microseisms [1]. Hasselmann extended Longuet-Higgins' theory to a general sea state and developed a connection between the stochastic model used to describe ocean waves and the statistics of the observed microseism signal [21]. Brekhovskikh demonstrated that a large part of atmospheric microbarom signal is due to radiation of sound by pressure fluctuations produced in the water by the motion of the ocean surface [29]. Waxler and Gilbert extended the work of Longuet-Higgins, Hasselmann, and Brekhovskikh to develop a rigorous mathematical description of the mechanism which generates atmospheric and oceanic microbaroms via the fluctuations discussed by Brekhovskikh as well as compression of the air by the ocean surface motion [22].

Here we summarize the theoretical basis published by Waxler and Gilbert for the generation of microbarom radiation from an active sea state, discuss the coupling mechanism by which the cyclonic winds of a large maritime storm generates the ocean surface wave pattern necessary to generate microbaroms, and demonstrate the manner in which the interaction of the surface waves of a maritime storm and the background ocean swell can generate microbarom radiation.

The Microbarom Generation Mechanism

We set up the source region description as follows. Two fluids of different densities (air and water) are under the influence of gravity and therefore a stratified medium is formed with the interface between the air and water defining a plane at $z = 0$. Energy in the system can produce

displacement of the interface surface which we describe as $\zeta(\vec{x}_H, t)$ where $\vec{x}_H$ is some location in the horizontal plane $\vec{x}_H = (x, y)$.

The Sea State

The sea state is typically described statistically and therefore it is often expressed using its Fourier components [30, 31],

$$\zeta(\vec{x}_H, t) = \mathrm{Re}\left[\int \hat{\zeta}\left(\vec{k}\right) e^{i(\vec{k}\cdot\vec{x}_H - \omega(\vec{k})t)} d^2k\right]. \tag{1}$$

Assuming, further, that the process is Gaussian with mean zero, we can denote the expectation value by

$$\left\langle \hat{\zeta}\left(\vec{k}\right)\hat{\zeta}(\vec{q})\right\rangle = \left\langle \hat{\zeta}^*\left(\vec{k}\right)\hat{\zeta}^*(\vec{q})\right\rangle = 0, \tag{2a}$$

$$\left\langle \hat{\zeta}\left(\vec{k}\right)\hat{\zeta}^*(\vec{q})\right\rangle = \mathcal{F}\left(\vec{k}\right)\delta\left(\vec{k}-\vec{q}\right), \tag{2b}$$

where we've defined $\mathcal{F}\left(\vec{k}\right)$ to be the wave number spectral density function. The physical interpretation of this is that the wind field over the ocean surface provides some energy to the ocean surface which develops some steady state described by a superposition of linear waves whose statistics are described by $\mathcal{F}\left(\vec{k}\right)$.

Additionally, if the sea state dispersion relation $2\pi f = \omega\left(\vec{k}\right)$ is known, one can relate the wave vector density function to the directional spectral density function $F(f, \theta)$ by [30, 31]

$$\mathcal{F}\left(\vec{k}\right) d^2k = F(f, \theta)\, df\, d\theta, \tag{3}$$

where f is frequency in Hz and θ is a direction of propagation relative to some fixed reference direction. As a function of θ, $F(f, \theta)$ is generally strongly peaked at angles near those of the direction of the prevailing winds. Integrating over θ, one can find the frequency spectrum,

$$\bar{F}(f) = \int_0^{2\pi} F(f, \theta)\, d\theta,$$

which can then be used to calculate the "significant wave height",

$$H = 4\sqrt{\int \mathcal{F}\left(\vec{k}\right) d^2k} = 4\sqrt{\int_0^\infty \bar{F}(f)\, df}. \tag{4}$$

In the case of deep water, one can show that $\omega\left(\vec{k}\right) = \sqrt{gk}$ where g is the gravitational acceleration [32]. Observations have shown that $\hat{\zeta}$ in Eq. (1) is strongly peaked at 0.1 Hz, which produces a surface wavelength of $\frac{2\pi}{k} \approx 150$ meters. The nonlinear nature of the microbarom generation results in frequency doubling and a dominant microbarom peak at 0.2 Hz. This corresponds to acoustic wavelengths of 1.7 and 7.5 kilometers in air and water respectively. Thus, the ocean surface wavelength is much shorter than the acoustic wavelengths and the values of $\vec{k}$ for which $\mathcal{F}\left(\vec{k}\right)$ are significant satisfy,

$$\frac{\omega}{c_w} < \frac{\omega}{c_a} \ll k. \tag{5}$$

Equations of Motion in the Source Region

Consider some region around the air-water interface which we will denote as S. The region extends above and below the interface to a greater extent than the ocean surface wavelengths, but much less than the acoustic wavelengths in air and water. Within this region the air and water obey the equations of lossless fluid mechanics. One has the continuity of mass, Euler, and adiabatic state equations [7],

$$\frac{\partial \rho}{\partial t} + \vec{\nabla} \cdot (\rho \vec{v}) = 0, \tag{6a}$$

$$\rho\left(\frac{\partial \vec{v}}{\partial t} + \left(\vec{v} \cdot \vec{\nabla}\right)\vec{v}\right) + \vec{\nabla} p = -\rho g \vec{\hat{z}}, \tag{6b}$$

$$\rho = f_\sigma(p), \quad \sigma = a \text{ (air)}, w \text{ (water)}. \tag{6c}$$

Note that the equation of state differs in the two media. These equations must hold in the bulk of each fluid separately. In addition to the conditions in Eq. (6), the pressure and normal velocity must be continuous across the interface,

$$p\left(\vec{x}_H, \zeta + 0^+, t\right) = p\left(\vec{x}_H, \zeta - 0^+, t\right), \tag{7a}$$

$$\vec{n}\left(\vec{x}_H, t\right) \cdot \left[\vec{v}\left(\vec{x}_H, \zeta + 0^+, t\right) - \vec{v}\left(\vec{x}_H, \zeta - 0^+, t\right)\right] = 0, \tag{7b}$$

where $\vec{n}$ is an upward pointing normal vector to the interface which can be defined as,

$$\vec{n}\left(\vec{x}_H, t\right) = \begin{pmatrix} -\vec{\nabla}_H \zeta \\ 1 \end{pmatrix}, \qquad \vec{\nabla}_H = \begin{pmatrix} \frac{\partial}{\partial x} \\ \frac{\partial}{\partial y} \end{pmatrix}.$$

Lastly, the vertical component of the interface motion must equal that of the adjacent fluid,

$$v_z\left(\vec{x}_H, \zeta \pm 0^{\pm}, t\right) = \frac{\partial \zeta}{\partial t} + \vec{v}\left(\vec{x}_H, \zeta \pm 0^{+}, t\right) \cdot \vec{\nabla}\zeta = \frac{D\zeta}{Dt}_{z=\zeta \pm 0^{+}}, \tag{8}$$

where $\frac{D}{Dt} = \frac{\partial}{\partial t} + \vec{v} \cdot \vec{\nabla}$ is the convective derivative.

Solving by Perturbation

Solving Eq. (6) and (7) with $\zeta \neq 0$ requires an approximation of some kind. The nonlinearities in such a description are best treated using perturbative expansion about some ambient state [33, 34]. The pressure, density, velocity, and displacement can be expanded about the ambient state as

$$p = p_0 + p_1 + p_2 + \ldots, \tag{9}$$

with similar expansions for ρ, $\vec{v}$, and ζ. It is assumed that in the ambient state, $\zeta_0 = 0$. Here we've denoted solutions of the linear approximation by subscript 1's and terms quadratic in linear solutions as subscript 2's. Keeping terms up to second order, the equations of fluid mechanics become,

$$\frac{\partial \rho_0}{\partial t} + \vec{\nabla} \cdot (\rho_0 \vec{v}_0) \tag{10a}$$

$$+ \frac{\partial \rho_1}{\partial t} + \vec{\nabla} \cdot (\rho_1 \vec{v}_0 + \rho_0 \vec{v}_1) \tag{10b}$$

$$+ \frac{\partial \rho_2}{\partial t} + \vec{\nabla} \cdot (\rho_2 \vec{v}_0 + \rho_0 \vec{v}_2 + \rho_1 \vec{v}_1) + \ldots = 0, \tag{10c}$$

$$\rho_0 \frac{D\vec{v}_0}{Dt} + \vec{\nabla} p_0 + \rho_0 g\vec{\hat{z}} \tag{11a}$$

$$+ \rho_0 \left(\frac{D\vec{v}_1}{Dt} + \left(\vec{v}_1 \cdot \vec{\nabla}\right) \vec{v}_0 \right) + \rho_1 \frac{D\vec{v}_0}{Dt} + \vec{\nabla} p_1 + \rho_1 g\vec{\hat{z}} \tag{11b}$$

$$+ \rho_0 \left(\frac{D\vec{v}_2}{Dt} + \left(\vec{v}_2 \cdot \vec{\nabla}\right) \vec{v}_0 + \left(\vec{v}_1 \cdot \vec{\nabla}\right) \vec{v}_1 \right) + \rho_1 \left(\frac{D\vec{v}_1}{Dt} + \left(\vec{v}_1 \cdot \vec{\nabla}\right) \vec{v}_0 \right)$$

$$+ \vec{\nabla} p_2 + \rho_2 g\vec{\hat{z}} + \ldots = 0, \tag{11c}$$

and the state equation can be written as a Taylor series expansion in the pressure. Additionally, the boundary conditions become,

$$p_0\Big|_{\pm 0^+} \tag{12a}$$

$$+ \left[p_1 + \zeta_1 \frac{\partial p_0}{\partial z} \right]_{\pm 0^+} \tag{12b}$$

$$+ \left[p_2 + \zeta_2 \frac{\partial p_0}{\partial z} + \zeta_1 \frac{\partial p_1}{\partial z} + \frac{1}{2} \zeta_1^2 \frac{\partial^2 p_0}{\partial z^2} \right]_{\pm 0^+} + \ldots = 0, \tag{12c}$$

$$v_{0z}\Big|_{\pm 0^+} \tag{13a}$$

$$+ \left[v_{1z} + \zeta_1 \frac{\partial v_{0z}}{\partial z} \right]_{\pm 0^+} \tag{13b}$$

$$+ \left[v_{2z} + \zeta_1 \frac{\partial v_{1z}}{\partial z} - \vec{v}_1 \cdot \vec{\nabla} \zeta_1 \right]_{\pm 0^+} + \ldots = 0, \tag{13c}$$

$$v_{0z}\Big|_{\pm 0^+} \tag{14a}$$

$$+ v_{1z}\Big|_{\pm 0^+} - \frac{\partial \zeta_1}{\partial t} \tag{14b}$$

$$+ \left[v_{2z} + \zeta_1 \frac{\partial v_{1z}}{\partial z} - \vec{v}_1 \cdot \vec{\nabla} \zeta_1 \right]_{\pm 0^+} - \frac{\partial \zeta_2}{\partial t} + \ldots = 0, \tag{14c}$$

where we've used the simplification that $\zeta_0 = 0$ in the unperturbed ambient state. In each of these equations (a) denotes the zeroth order unperturbed state, (b) denotes the linear perturbation, and

(c) denotes the second order perturbations.

Ambient State. With ζ_0 set to zero, the only forcing on the system in the zeroth order state is gravity and one has $p_0(z)$, $\rho_0(z)$, and $\vec{v}_0(z)$ with $v_z(z) = 0$. This reduces the equations of fluid mechanics to the simple conditions

$$\frac{dp_0}{dz} = -\rho_0 g \quad \rightarrow \quad \int_{p_0(0)}^{p_0(z)} = \frac{1}{f(p_0)} dp_0 = -gz. \tag{15}$$

The state equations in the source region for the ambient state is given by $\rho_\sigma = f_\sigma(p_0(0))$ which allows one to use the adiabatic small-signal sound speeds at the interface, $c_\sigma = \sqrt{\frac{1}{f'_\sigma(p_0(0))}}$, where the prime denotes differentiation with respect to p_0. The expansion of the pressure can be written,

$$p_0(z) = p_0(0) - \rho_\sigma g z + \frac{\rho_\sigma g^2}{2c_\sigma^2} z^2 + \ldots. \tag{16}$$

For the case here we assume that $\vec{v}_0 = 0$ and from the above we note that ρ_0 and c_0 are discontinuous but approximately piece-wise constant at the interface.

Linear Response. At linear order, the equation of state simply relates $c_\sigma^2 \rho_1 = p_1$ and the linear equations in Eq. (10b) and (11b) can be written as,

$$\frac{\partial p_1}{\partial t} + \rho_\sigma c_\sigma^2 \vec{\nabla} \cdot \vec{v}_1 = 0, \tag{17a}$$

$$\vec{\nabla} p_1 + \rho_\sigma \frac{\partial \vec{v}_1}{\partial t} + g\rho_1 \vec{\hat{z}} = 0. \tag{17b}$$

The interface conditions can be simplified by the results of the zeroth order state, yielding

$$[p_1 - \rho_\sigma g \zeta_1]_{\pm 0^+} = 0, \tag{18a}$$

$$\frac{\partial \zeta_1}{\partial t} = v_{1z}\left(\vec{x}_H, 0^+, t\right) = v_{1z}\left(\vec{x}_H, -0^+, t\right). \tag{18b}$$

A velocity potential, ϕ_1, can be introduced which satisfies

$$\vec{v}_1 = \vec{\nabla}\phi_1 + \vec{w}_1, \qquad \vec{\nabla} \cdot \vec{w}_1 = 0, \tag{19a}$$

$$p_1(\vec{x}, z, t) = -\rho_\sigma \frac{\partial \phi_1}{\partial t}. \tag{19b}$$

Eq. (17b) can be satisfied by requiring $\rho_\sigma \frac{\partial \vec{w}_1}{\partial t} = -\frac{g}{c_\sigma^2} p_1 \vec{\hat{z}}$. Combining this with Eq. (17a) results in a wave equation for the velocity potential,

$$\left(\nabla^2 - \frac{1}{c_\sigma^2}\frac{\partial^2}{\partial t^2}\right)\phi_1 = 0. \tag{20}$$

The source driving the system is the interface motion through the pressure boundary condition. The interface displacement can once again be expanded into Fourier components,

$$\zeta_1\left(\vec{x}_H, t\right) = \mathrm{Re}\left[\int \hat{\zeta}_1\left(\vec{k}\right) e^{i\left(\vec{k}\cdot\vec{x}_H - \omega\left(\vec{k}\right)t\right)} d^2k\right], \tag{21}$$

where $\hat{\zeta}$ that from Eq. (2). Expanding ϕ_1 in the same manner and substituting it into Eq. (20) yields,

$$\phi_1\left(\vec{x}_H, t\right) = \mathrm{Re}\left[\int \hat{\phi}_1^{(\sigma)}\left(\vec{k}\right) e^{i\left(\vec{k}\cdot\vec{x}_H - \omega\left(\vec{k}\right)t\right) - \sqrt{k^2 - \frac{\omega^2}{c_\sigma^2}}|z|} d^2k\right], \tag{22}$$

and from the above results we can determine that,

$$\rho_\sigma \frac{\partial \vec{w}_1}{\partial t} = -\frac{g}{c_\sigma^2} p_1 \vec{\hat{z}} \quad \rightarrow \quad w_{1z} \sim \frac{g}{\omega_0 c_\sigma}\frac{p_1}{\rho_\sigma c_\sigma}, \tag{23a}$$

$$p_1\left(\vec{x}, z, t\right) = -\rho_\sigma \frac{\partial \phi_1}{\partial t} \quad \rightarrow \quad \frac{\partial \phi_1}{\partial z} \sim \frac{k_0 c_\sigma}{\omega_0}\frac{p_1}{\rho_\sigma c_\sigma},$$

$$\rightarrow \quad w_{1z} \sim \frac{g}{\omega_0 c_\sigma}\frac{\omega_0}{k_0 c_\sigma}\frac{\partial \phi_1}{\partial z}. \tag{23b}$$

And thus $\vec{w}_1$ is negligible compared to $\vec{\nabla}\phi_1$. The resulting pressure and velocity fields can be written

$$p_1\left(\vec{x}, t\right) = \mathrm{Re}\left[\int \hat{p}_1^{(\sigma)}\left(\vec{k}\right) e^{i\left(\vec{k}\cdot\vec{x}_H - \omega\left(\vec{k}\right)t\right) - \sqrt{k^2 - \frac{\omega^2}{c_\sigma^2}}|z|} d^2k\right], \tag{24a}$$

$$\vec{v}_1\left(\vec{x}, t\right) = \mathrm{Re}\left[\int \vec{\hat{v}}_1^{(\sigma)}\left(\vec{k}\right) e^{i\left(\vec{k}\cdot\vec{x}_H - \omega\left(\vec{k}\right)t\right) - \sqrt{k^2 - \frac{\omega^2}{c_\sigma^2}}|z|} d^2k\right]. \tag{24b}$$

Substituting these forms into the interface conditions and letting $(-1)^\sigma$ be 1 in air and -1 in water, one obtains

$$\hat{\phi}_1^{(\sigma)}\left(\vec{k}\right) = (-1)^\sigma \frac{i\omega}{\sqrt{k^2 - \frac{\omega^2}{c_\sigma^2}}} \hat{\zeta}_1\left(\vec{k}\right), \tag{25a}$$

$$\hat{p}_1^{(\sigma)}\left(\vec{k}\right) = -\left(-1\right)^{\sigma}\frac{\rho_\sigma \omega^2}{\sqrt{k^2-\frac{\omega^2}{c_\sigma^2}}}\hat{\zeta}_1\left(\vec{k}\right), \tag{25b}$$

$$\hat{\vec{v}}_1^{(\sigma)}\left(\vec{k}\right) = \omega\left[-\left(-1\right)^{\sigma}\frac{\vec{k}}{\sqrt{k^2-\frac{\omega^2}{c_\sigma^2}}} - i\vec{\hat{z}}\right]\hat{\zeta}_1\left(\vec{k}\right). \tag{25c}$$

It was previously shown that $\frac{\omega}{c_w} < \frac{\omega}{c_a} \ll k$. Because of this, the oscillations of the interface which are driving the perturbations can only produce evanescent solutions. The physical pictures of this result is that the motion of the ocean surface is simply too slow for compression of the air to generate acoustic radiation [22].

Several useful relations can still be produced from these results. The pressure continuity requires

$$0 = \left(\rho_w - \rho_a\right)g + \frac{\omega^2}{k}\left(\frac{\rho_w}{\sqrt{1-\frac{\omega^2}{k^2c_w^2}}} + \frac{\rho_a}{\sqrt{1-\frac{\omega^2}{k^2c_a^2}}}\right), \tag{26}$$

which approximates the expected dispersion relation for surface waves $\omega = \sqrt{gk}$. It is worth noting that with this condition, the two parameters $\frac{\omega_0}{k_0 c_\sigma}$ and $\frac{g}{\omega_0 c_\sigma}$ are identical. Lastly, we can show that the first order velocity and pressure can be written in terms of the significant wave height H_S,

$$v_1 \sim c_\sigma \frac{\omega H_S}{c_\sigma}, \qquad p_1 \sim \rho_\sigma c_\sigma^2 \frac{\omega_0}{k_0 c_\sigma}\frac{\omega_0 H_2}{c_\sigma}. \tag{27}$$

which are both first order in Mach number, $\frac{\omega_0 H_S}{c_\sigma}$, while the pressure is also first order in the small parameter $\frac{\omega_0}{k_0 c_\sigma}$.

Second Order Response. At second order, the equation of state becomes $\rho_2 - \frac{1}{c_\sigma^2}p_2 = \frac{f''(p_0)}{2}p_1^2$ and the second order equations in Eq. (10c) and (11c) can be written as,

$$\frac{\partial p_2}{\partial t} + \rho_\sigma c_\sigma^2 \vec{\nabla}\cdot\vec{v}_2 = \frac{1-\rho_\sigma c_\sigma^4 f''\left(p_0\right)}{\rho_\sigma c_\sigma^2}p_1\frac{\partial p_1}{\partial t} - \vec{v}_1\cdot\vec{\nabla}p_1, \tag{28a}$$

$$\vec{\nabla}p_2 + \rho_\sigma\frac{\partial \vec{v}_2}{\partial t} + g\rho_2\vec{\hat{z}} = -\frac{p_1}{c_\sigma^2}\frac{\partial \vec{v}_1}{\partial t} - \frac{\rho_\sigma}{2}\vec{\nabla}\left(\vec{v}_1\cdot\vec{v}_1\right). \tag{28b}$$

Near the interface, one can use the nonlinear form of the equation of state, $f''\left(p_0\right) \approx -\frac{B}{A}\frac{1}{\rho_\sigma c_\sigma^4}$ [6]. Combining this with the linear result for the order estimate of p_1, the right hand sides of the state

and continuity equations can be estimated,

$$\frac{1}{2}f''\left(p_0\right)p_1^2 \sim \frac{B}{A}\rho_\sigma\left(\frac{\omega_0}{k_0 c_\sigma}\right)^2\left(\frac{\omega_0 H_S}{c_\sigma}\right)^2,$$

$$\frac{1-\rho_\sigma c_\sigma^4 f''\left(p_0\right)}{\rho_\sigma c_\sigma^2}p_1\frac{\partial p_1}{\partial t} \sim \left(1+\frac{B}{A}\right)\rho_\sigma c_\sigma^2\omega_0\left(\frac{\omega_0}{k_0 c_\sigma}\right)^2\left(\frac{\omega_0 H_S}{c_\sigma}\right)^2,$$

$$\vec{v}_1\cdot\vec{\nabla}p_1 \sim \rho_\sigma c_\sigma^2\omega_0\left(\frac{\omega_0 H_S}{c_\sigma}\right)^2.$$

These results are all second order in Mach number, $\frac{\omega_0 H_S}{c_\sigma}$. Additionally, the two terms containing $f''\left(p_0\right)$ are second-order in the small parameter, $\frac{\omega_0}{k_0 c_\sigma}$, and therefore can be neglected. Similarly, on the right hand side of the Euler equation one has

$$\frac{1}{c_\sigma^2}p_1\frac{\partial\vec{v}_1}{\partial t} \sim \rho_\sigma c_\sigma\omega_0\frac{\omega_0}{k_0 c_\sigma}\left(\frac{\omega_0 H_S}{c_\sigma}\right)^2,$$

$$\frac{1}{2}\rho_\sigma\vec{\nabla}{v_1}^2 \sim \rho_\sigma c_\sigma^2 k_0\left(\frac{\omega_0 H_S}{c_\sigma}\right)^2.$$

The first of these is again smaller by two orders of the small parameter $\frac{\omega_0}{k_0 c_\sigma}$ and can be dropped. Thus we can ignore some terms in the above system of equations and instead solve the simplified system of equations in which the equation of state has the form $c_\sigma^2\rho_2 = p_2$, and the continuity and Euler equations are

$$\frac{\partial p_2}{\partial t} + \rho_\sigma c_\sigma^2\vec{\nabla}\cdot\vec{v}_2 = -\vec{v}_1\cdot\vec{\nabla}p_1, \tag{31a}$$

$$\vec{\nabla}p_2 + \rho_\sigma\frac{\partial\vec{v}_2}{\partial t} + g\rho_2\hat{\vec{z}} = -\frac{\rho_\sigma}{2}\vec{\nabla}\left(\vec{v}_1\cdot\vec{v}_1\right). \tag{31b}$$

Given this set of equations, all that remains is to determine the interface conditions. The third term in Eq. (12c) can be simplified by referencing Eq. (17b),

$$\zeta_1\frac{\partial p_1}{\partial z} = -\rho_\sigma\zeta_1\frac{\partial v_{1z}}{\partial t} \sim \rho_\sigma c_\sigma^2\left(\frac{\omega_0 H_S}{c_\sigma}\right)^2.$$

The last term in the pressure boundary condition can be simplified with Eq. (16),

$$\frac{1}{2}\zeta_1^2\frac{\partial^2 p_0}{\partial z^2} = \frac{1}{2}\frac{\rho_\sigma g^2}{c_\sigma^2}\zeta_1^2 \sim \rho_\sigma c_\sigma^2\left(\frac{g}{\omega_0 c_\sigma}\right)^2\left(\frac{\omega_0 H_S}{c_\sigma}\right)^2.$$

The last term is second order in both Mach number and the small parameter $\frac{g}{\omega_0 c_\sigma}$ and therefore can be neglected. Thus one obtains

$$\left(p_2 - \rho_\sigma g\zeta_2\right)\Big|_{-0^+}^{0^+} = \rho_\sigma\zeta_1\frac{\partial v_{1z}}{\partial t}\Big|_{-0^+}^{0^+}. \tag{32}$$

The second order velocity and interface conditions are given by Eq. (13c) and (14c).

The problem now reduces to substituting the linear solutions into the second order wave equations and determining the outgoing solutions which satisfy the interface conditions. This process can be simplified by assuming that compressibility is insignificant in the linear approximation, $\sqrt{k^2 - \frac{\omega^2(\vec{k})}{c_\sigma^2}} \approx k$. The source terms in the velocity and interface displacement conditions can be written alternately as,

$$-\zeta_1\frac{\partial v_{1z}}{\partial z} + \vec{v}_1\cdot\vec{\nabla}_H\zeta_1 = -\zeta_1\vec{\nabla}\cdot\vec{v}_1 + \vec{\nabla}_H\cdot\left(\zeta_1\vec{v}_1\right), \tag{33}$$

which, in the incompressible approximation, reduces to only $\vec{\nabla}_H\cdot(\zeta_1\vec{v}_1)$. This remaining term is zero since, in the case of microbarom generation, $\zeta_1\vec{v}_1$ is constant for counter propagating waves with equal period (frequency). Thus, while the right hand side of the v_{2z} condition appears to be quite large (of order $\frac{k_0 c_\sigma}{\omega_0}\left(\frac{\omega_0 H_S}{c_\sigma}\right)^2$), its contribution in the case of microbarom radiation will be small.

Once again we choose to write $\vec{v}_2$ in terms of a velocity potential ϕ_2 which satisfies,

$$\vec{\nabla}\phi_2 + \vec{w}_2, \qquad \vec{\nabla}\cdot\vec{w}_2 = 0, \tag{34a}$$

$$\rho_\sigma\frac{\partial\vec{w}_2}{\partial t} + \frac{g}{c_\sigma^2}p_2\vec{\hat{z}} = 0, \tag{34b}$$

$$p_2 + \rho_\sigma\frac{\partial\phi_2}{\partial t} = -\frac{1}{2}\rho_\sigma\vec{v}_1\cdot\vec{v}_1, \tag{34c}$$

which satisfies the second order Euler equation. As in the linear case, one can show that $\vec{w}_2 \ll \vec{\nabla}\phi_2$

and therefore this extra contribution to $\vec{v}_2$ is ignored and one is left with $\vec{v}_2 = \vec{\nabla}\phi_2$. Combining the above with the second order continuity and first order Euler equations, one obtains

$$\left(\nabla^2 - \frac{1}{c_\sigma^2}\frac{\partial^2}{\partial t^2}\right)\phi_2 = \frac{1}{c_\sigma^2}\frac{\partial}{\partial t}\left(\vec{v}_1 \cdot \vec{v}_1\right). \tag{35}$$

Because the linear solution, $\vec{v}_1$, decreases exponentially away from the interface, the driving function on the right hand side of this wave equation is nonzero only near the interface. Using the form of the source function on the right hand side and the coupling of the near surface winds with the ocean surface wave field (which will be discussed in more detail later), one can demonstrate that microbaroms are produced only in the case of counter propagating waves of equal magnitude. In the case of two interacting waves $\vec{k}_1$ and $\vec{k}_2$ with equal magnitude but different directions,

$$\zeta_1\left(\vec{x}_\perp, t\right) = Z_0\left[e^{i\vec{k}_1\cdot\vec{x}_\perp - i\omega t} + e^{i\vec{k}_2\cdot\vec{x}_\perp - i\omega t}\right]. \tag{36}$$

Comparing this with the relation between $\zeta_1\left(\vec{x}_\perp, t\right) \leftrightarrow \hat{\zeta}_1\left(\vec{k}, \omega\right)$,

$$\zeta_1\left(\vec{x}_\perp, t\right) = \mathrm{Re}\left[\int \hat{\zeta}_1\left(\vec{k}, \omega\right) e^{i\vec{k}\cdot\vec{x}_\perp - i\omega t} d^2k\right] \quad \rightarrow \quad \hat{\zeta}_1 = Z_0\left[\delta\left(\vec{k} - \vec{k}_1\right) + \delta\left(\vec{k} - \vec{k}_2\right)\right],$$

which produces a linear velocity perturbation in the atmosphere of the form,

$$\hat{\vec{v}}_1 = -Z_0\omega\left[\frac{\vec{k}}{\sqrt{k^2 - \frac{\omega^2}{c_a^2}}} + i\vec{\hat{z}}\right]\left[\delta\left(\vec{k} - \vec{k}_1\right) + \delta\left(\vec{k} - \vec{k}_2\right)\right].$$

$$\begin{aligned}
\vec{v}_1\left(\vec{x}, t\right) &= \mathrm{Re}\left[\int \vec{\hat{v}}_1^{(\sigma)}\left(\vec{k}\right) e^{i\left(\vec{k}\cdot\vec{x}_H - \omega\left(\vec{k}\right)t\right) - \sqrt{k^2 - \frac{\omega^2}{c_\sigma^2}}|z|} d^2k\right]. \\
&= -Z_0\omega e^{-\sqrt{k^2 - \frac{\omega^2}{c_a^2}}|z|} \\
&\qquad \times \ \mathrm{Re}\left[\left[\frac{\vec{k}_1}{\sqrt{k^2 - \frac{\omega^2}{c_a^2}}} + i\vec{\hat{z}}\right] e^{i\vec{k}_1\cdot\vec{x}_\perp - i\omega t} + \left[\frac{\vec{k}_2}{\sqrt{k^2 - \frac{\omega^2}{c_a^2}}} + i\vec{\hat{z}}\right] e^{i\vec{k}_2\cdot\vec{x} - i\omega t}\right],
\end{aligned}$$

and the source term in Eq. (35) goes as

$$\frac{1}{c_a^2}\frac{\partial}{\partial t}\vec{v}_1\cdot\vec{v}_1 = -2i\omega Z_0^2\frac{\omega^2}{c_a^2}e^{-2\sqrt{k^2-\frac{\omega^2}{c_a^2}}|z|} \times \mathrm{Re}\Big[|\vec{C}_1|^2 e^{2i\vec{k}_1\cdot\vec{x}_\perp - 2i\omega t} + |\vec{C}_2|^2 e^{2i\vec{k}_2\cdot\vec{x}-2i\omega t} + 2\left(\vec{C}_1\cdot\vec{C}_2\right)e^{i(\vec{k}_1+\vec{k}_2)\cdot\vec{x}-2i\omega t}\Big], \tag{37}$$

where $\vec{C}_j = \frac{\vec{k}_j}{\sqrt{k^2-\frac{\omega^2}{c_a^2}}} + i\hat{z}$. In order to obtain a radiating solution, a source term which oscillates independently of $\vec{k}$ must be present (otherwise solutions will be evanescent as in the linear case). Examining the third term, it is immediately clear that such a source term is only possible if $\vec{k}_1 = -\vec{k}_2$. Thus only counter propagating waves of equal period will generate the source term necessary to radiate microbaroms into the ocean and atmosphere. This results also produces the frequency doubling effect observed in the microbarom spectra compared with the ocean surface wave spectra [30, 31].

The second order wave equation, Eq. (35), contains the effects of nonlinearities in the air and water themselves. Additionally, the second-order interface conditions in Eq. (32), (13c), and (14c) contain nonlinear effects due to the motion of the fluid interface. As is usually the practice in solving any inhomogeneous differential equation, one expands the solution into a particular solution, ϕ_p and a solution to the homogeneous equation, ϕ_h [35]. In order to obtain ϕ_p, one takes the first order solution form of $\vec{v}_1$ and plugs them into the second order wave equation using the incompressible approximation $\sqrt{k^2-\frac{\omega^2(\vec{k})}{c_\sigma^2}} \approx k$. The resulting source term has the form

$$\frac{1}{c_\sigma^2}\frac{\partial}{\partial t}\left(\vec{v}_1\cdot\vec{v}_1\right) = \iint\Big[\mathcal{R}_\sigma^{(+)}\left(\vec{k},\vec{q}\right)\hat{\zeta}_1\left(\vec{k}\right)\hat{\zeta}_1\left(\vec{q}\right)e^{i\left((\vec{k}+\vec{q})\cdot\vec{x}_H-\left(\omega(\vec{k})+\omega(\vec{q})\right)t\right)} + \mathcal{R}_\sigma^{(-)}\left(\vec{k},\vec{q}\right)\hat{\zeta}_1\left(\vec{k}\right)\hat{\zeta}_1\left(\vec{q}\right)e^{i\left((\vec{k}-\vec{q})\cdot\vec{x}_H-\left(\omega(\vec{k})-\omega(\vec{q})\right)t\right)}\Big] \times e^{-(k+q)z}d^2k\,d^2q + \text{complex conjugate}, \tag{38}$$

where,

$$\mathcal{R}_\sigma^{(\pm)}\left(\vec{k},\vec{q}\right) = -\frac{i}{c_\sigma^2}\omega\left(\vec{k}\right)\omega\left(\vec{q}\right)\left[\omega\left(\vec{k}\right)\pm\omega\left(\vec{q}\right)\right]\left(\frac{\vec{k}\cdot\vec{q}}{kq}\mp 1\right). \tag{39}$$

From this, the particular and homogeneous solutions can be written in the forms

$$\phi_p\left(\vec{x}_H,z,t\right)=\iint\Big[\mathcal{Q}_\sigma^{(+)}\left(\vec{k},\vec{q}\right)\hat{\zeta}_1\left(\vec{k}\right)\hat{\zeta}_1\left(\vec{q}\right)e^{i\left(\left(\vec{k}+\vec{q}\right)\cdot\vec{x}_H-\left(\omega\left(\vec{k}\right)+\omega\left(\vec{q}\right)\right)t\right)-(k+q)|z|}$$
$$+\mathcal{Q}_\sigma^{(-)}\left(\vec{k},\vec{q}\right)\hat{\zeta}_1\left(\vec{k}\right)\hat{\zeta}_1^*\left(\vec{q}\right)e^{i\left(\left(\vec{k}-\vec{q}\right)\cdot\vec{x}_H-\left(\omega\left(\vec{k}\right)-\omega\left(\vec{q}\right)\right)t\right)-(k+q)|z|}\Big]d^2k\,d^2q$$
$$+\ \text{complex conjugate},\tag{40}$$

$$\mathcal{Q}_\sigma^{(\pm)}\left(\vec{k},\vec{q}\right)=\frac{\mathcal{R}_\sigma^{(\pm)}\left(\vec{k},\vec{q}\right)}{\left[\frac{\left(\omega\left(\vec{k}\right)\pm\omega\left(\vec{q}\right)\right)^2}{c_\sigma^2}\right]+2\left(kq\mp\vec{k}\cdot\vec{q}\right)},\tag{41}$$

$$\phi_h\left(\vec{x}_H,z,t\right)=\iint\Big[\mathcal{C}_\sigma^{(+)}\left(\vec{k},\vec{q}\right)\hat{\zeta}_1\left(\vec{k}\right)\hat{\zeta}_1\left(\vec{q}\right)e^{i\left(\left(\vec{k}+\vec{q}\right)\cdot\vec{x}_H-\left(\omega\left(\vec{k}\right)+\omega\left(\vec{q}\right)\right)t\right)+i\Omega^{(+)}\left(\vec{k},\vec{q}\right)|z|}$$
$$+\mathcal{C}_\sigma^{(-)}\left(\vec{k},\vec{q}\right)\hat{\zeta}_1\left(\vec{k}\right)\hat{\zeta}_1^*\left(\vec{q}\right)e^{i\left(\left(\vec{k}-\vec{q}\right)\cdot\vec{x}_H-\left(\omega\left(\vec{k}\right)-\omega\left(\vec{q}\right)\right)t\right)+i\Omega^{(-)}\left(\vec{k},\vec{q}\right)|z|}\Big]d^2k\,d^2q$$
$$+\ \text{complex conjugate},\tag{42}$$

$$\Omega^{(\pm)}\left(\vec{k},\vec{q}\right)=\sqrt{\frac{\left(\omega\left(\vec{k}\right)\pm\omega\left(\vec{q}\right)\right)^2}{c_\sigma^2}-\left(\vec{k}\pm\vec{q}\right)^2}.\tag{43}$$

The resulting second order contribution to the sea state is given by

$$\zeta_2\left(\vec{x}_H,t\right)=\iint\Big[\hat{\zeta}^{(+)}\left(\vec{k},\vec{q}\right)\hat{\zeta}_1\left(\vec{k}\right)\hat{\zeta}_1\left(\vec{q}\right)e^{i\left(\left(\vec{k}+\vec{q}\right)\cdot\vec{x}_H-\left(\omega\left(\vec{k}\right)+\omega\left(\vec{q}\right)\right)t\right)}$$
$$+\hat{\zeta}^{(-)}\left(\vec{k},\vec{q}\right)\hat{\zeta}_1\left(\vec{k}\right)\hat{\zeta}_1^*\left(\vec{q}\right)e^{i\left(\left(\vec{k}-\vec{q}\right)\cdot\vec{x}_H-\left(\omega\left(\vec{k}\right)-\omega\left(\vec{q}\right)\right)t\right)}\Big]d^2k\,d^2q$$
$$+\,\text{complex conjugate}.\tag{44}$$

The coefficients $\mathcal{C}^{(\pm)}\left(\vec{k},\vec{q}\right)$ and $\hat{\zeta}^{(\pm)}\left(\vec{k},\vec{q}\right)$ are determined by the conditions on the interface. Explicit evaluation of these coefficients in general is difficult, however as discussed previously, in the case of microbaroms one can make a significant simplification by noting that only the coefficients with $\vec{q}=-\vec{k}$ will contribute to microbarom radiation.

The use of a particular solution and homogeneous solution separates the second order velocity potential into a term, ϕ_p, which is negligible outside of the source region and a second term, ϕ_h, which radiates into the atmosphere and ocean. The particular solution describes

the nonlinear effects produced in the bulk of the air or water, while the coupling of the homogeneous solution and particular solution by the interface conditions produces the radiation. That is, the solution, ϕ_p, is produced by the counter propagating waves but does not propagate away from the interface. Rather, the interface conditions couple ϕ_p to the radiation solution, ϕ_h, and through the non-linearities in the interface the microbaroms are generated [22].

The Microbarom Source Associated with a Large Maritime Storm

From the analysis in the previous section, specifically in Eq. (37), it is evident that a microbarom source region is characterized by counter propagating waves of equal period. There are a number of possible phenomena which could generate such a state, including interacting ocean currents, reflections due to continental shelves and coast lines, and cyclonic surface waves induced by large maritime storms. The last of these is the focus of this study. Here we intend to develop a formal physical explanation for the expected location of a microbarom source region produced by a large maritime storm.

Flow Above a Fluid-Fluid Interface

The driving force of surface waves due to a maritime storm is the interaction of the storm winds with the ocean surface. This interaction is generally overly complicated due to the complexity of the wind near the surface, however some simple analysis can be used to demonstrate how the flow couples into the surface wave field. The interaction of a steady flow with a fluid-fluid interface requires one to include viscosity in the description of the system. That is, the Euler equation, (6b), is replaced by the Navier-Stokes equation [7, 32, 36],

$$\rho\left[\frac{\partial\vec{v}}{\partial t}+\left(\vec{v}\cdot\vec{\nabla}\right)\vec{v}\right]=-\vec{\nabla}p+\nu\nabla^2\vec{v}+\rho g\hat{z}, \tag{45}$$

where we've assumed the fluid to be incompressible and denoted the kinematic coefficient of viscosity by $\frac{\mu}{\rho}=\nu$. Consider then a two dimensional treatment of two fluids bounded at $z=0$ and all horizontal variations contained in the x direction. The Navier-Stokes equation in such a case

reduces to,

$$\frac{\partial v_x}{\partial t} = -\frac{1}{\rho}\frac{\partial p}{\partial x} + \nu\nabla^2 v_x, \tag{46a}$$

$$\frac{\partial v_z}{\partial t} = -\frac{1}{\rho}\frac{\partial p}{\partial z} + \nu\nabla^2 v_z - g, \tag{46b}$$

$$\frac{\partial v_x}{\partial x} + \frac{\partial v_z}{\partial z} = 0. \tag{46c}$$

Vector potentials can be used to solve this problem by requiring,

$$v_x = -\frac{\partial \phi_x}{\partial x} - \frac{\partial \phi_z}{\partial z}, \qquad v_z = -\frac{\partial \phi_x}{\partial x} + \frac{\partial \phi_z}{\partial z}, \tag{47a}$$

$$\frac{p}{\rho} = \frac{\partial \phi}{\partial t} - gz, \tag{47b}$$

$$\vec{\nabla}_H^2 \phi_x = 0, \qquad \frac{\partial \phi_z}{\partial t} = \nu\nabla^2 \phi_z. \tag{47c}$$

The vector potentials can then be expanded in normal modes,

$$\phi_x = \left(Ae^{kz} + Be^{-kz}\right) e^{ikx - i\omega t}, \tag{48a}$$

$$\phi_z = \left(Ce^{mz} + De^{-mz}\right) e^{imx - i\omega t}, \tag{48b}$$

which results in the condition $m^2 = k^2 - i\frac{\omega}{\nu}$. For this analysis we are interested only in the behavior near the interface and can assume the lower fluid extends to an infinite depth. In order to maintain finite solutions, $B = 0$ and $D = 0$. Thus the velocity of the fluids are given by,

$$v_x = -\left(ikAe^{kz} + mCe^{mz}\right) e^{ikx - i\omega t}, \tag{49a}$$

$$v_z = -\left(kAe^{kz} - ikCe^{mz}\right) e^{ikx - i\omega t}. \tag{49b}$$

If we again denote $\zeta(x,t)$ to be the interface displacement from $z = 0$, we require $\frac{\partial \zeta}{\partial t} = v_z|_{z=0}$ which results in the interface displacement,

$$\zeta(x,t) = -i\frac{k}{\omega}(A - iC) e^{ikx - i\omega t}. \tag{50}$$

In a system without forcings, the stress conditions at the interface are given by [32, 36],

$$p_{zz} = -p + 2\mu\frac{\partial v_z}{\partial z} = T\frac{\partial^2\zeta}{\partial x^2}, \tag{51a}$$

$$p_{xz} = \mu\left(\frac{\partial v_x}{\partial z} + \frac{\partial v_z}{\partial x}\right) = 0, \tag{51b}$$

where T is the surface tension at the fluid-fluid interface. Combining these conditions with Eq. (49) and (50), one finds,

$$\begin{aligned}\frac{p_{zz}}{\rho} - \frac{T}{\rho}\frac{\partial^2\zeta}{\partial x^2} &= -\frac{\partial\phi_x}{\partial t} + \left(g + \frac{T}{\rho}k^2\right)\zeta + 2\nu\frac{\partial v_z}{\partial z} \\ &= \frac{1}{i\omega}\Big[\left(\omega^2 + 2i\nu k^2\omega - gk - \frac{T}{\rho}k^2\right)A \\ &\qquad - i\left(2i\nu km\omega - gk - \frac{T}{\rho}k^2\right)C\Big],\end{aligned} \tag{52a}$$

$$\frac{p_{xz}}{\rho} = -\left[2i\nu k^2 A + \left(-i\omega + 2\nu k^2\right)C\right]. \tag{52b}$$

Consider the case that arbitrary forcings given by p'_{zz}, $p'_{xz} \sim e^{ikx - i\omega_0 t}$ are acting on the interface with known parameters k and ω_0. It can be shown that in the deep ocean result, the dispersion relation is given by $\omega^2 = gk$ while the inclusion of surface tension results in the second term which modifies the dispersion relation resulting in $\omega^2 = gk + \frac{T}{\rho}k^3$ [7, 32]. Therefore, scaling these results by $\frac{1}{g\zeta}$ and simplifying,

$$\frac{p'_{zz}}{g\rho\zeta} = \frac{\left(-\omega^2 - 2i\nu k^2\omega + \omega_0^2\right)A - i\left(\omega_0^2 - 2i\nu km\omega\right)C}{gk\left(A - iC\right)}, \tag{53a}$$

$$\frac{p'_{xz}}{g\rho\zeta} = \frac{-i\omega}{gk}\frac{2i\nu k^2 A + \left(-i\omega + 2\nu k^2\right)C}{A - iC}. \tag{53b}$$

In the specific case that there is no vertical forcing on the surface, $p'_{zz} = 0$ in Eq. (53a) and one can solve for a relation between A and C. From this result, one can eliminate A and C in Eq. (53b) and determine the relation between p'_{xz} and ζ,

$$\frac{p'_{xz}}{g\rho\zeta} = \frac{\omega}{gk}\frac{\left(-i\omega + 2\nu k^2\right)^2 + \omega_0^2 - 4\nu^2 k^3 m}{-\omega^2 + 2\nu k^2 - 2\nu km}. \tag{54}$$

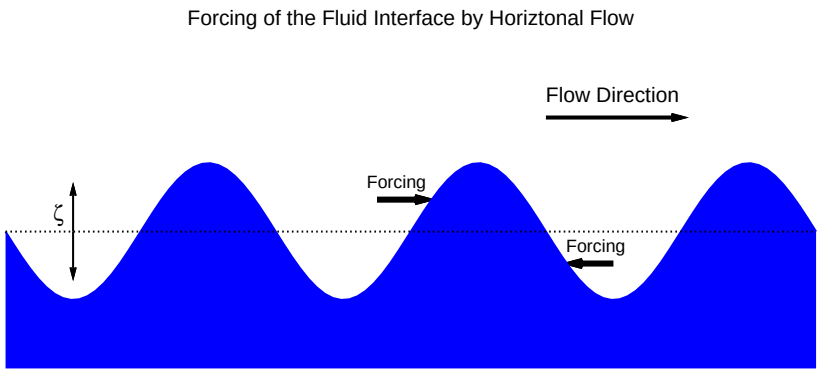

Fig. 1: The presence of flow at a fluid-fluid interface results in a forcing on the surface displacement given by Eq. (55).

In order to determine the forcing necessary to maintain a train of waves of given amplitude on the interface surface, we assume that $\omega = \omega_0$. This produces [36],

$$p'_{xz} = 4\nu k\omega_0\zeta. \tag{55}$$

Thus the tangential flow acts forwards on the crests of the waves (where ζ is positive) and backwards on the troughs (where ζ is negative) as seen in Fig. 1. This results in a transfer of energy from the flow into the surface wave amplitude. When the wind is directed parallel to the wavetrain with greater velocity than that of the wavetrain, an excess of pressure on the crests of the waveform produces an increase in the amplitude of the waves to a point at which the dissipation balances the work done by the surface forces. Alternately, if the wavetrain velocity is greater than that of the wind or the two are anti-parallel, the interaction results in a damping of the surface wave amplitude [36]. The result of this interaction is a strengthening of surface waves in the direction of flow and a dampening of the surface waves in other directions.

The Wind Field of a Large Maritime Storm

The result in Eq. (55) and the subsequent discussion indicates that the wind field near the ocean surface will produce a traveling wave train parallel to the wind. Therefore, one can infer that the strong cyclonic winds near the ocean surface generated by a large maritime storm will produce a cyclonic surface wave pattern underneath the storm. While such a cyclonic wave pattern alone does not produce the counter propagating waves necessary to produce microbaroms, the collision of the waves induced by the cyclonic winds with the background swell can produce the surface wave conditions necessary for microbarom generation at some location away from the storm center

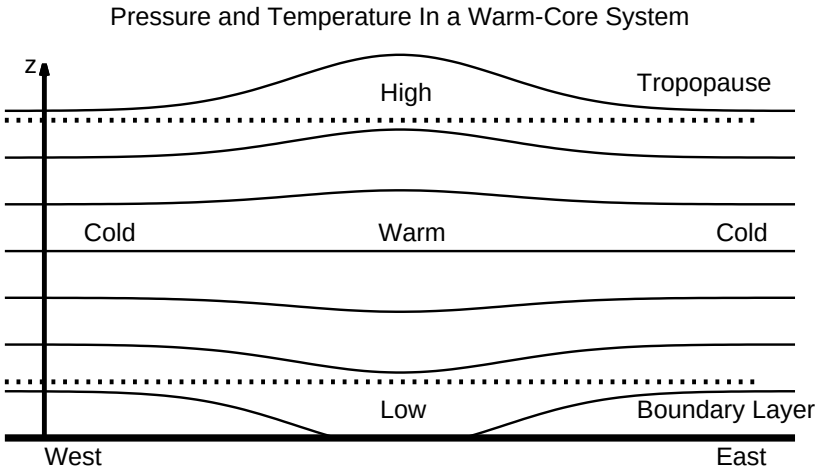

Fig. 2: The pressure and temperature in a large maritime storm. Thin lines denote isobaroms, dashed lines denote the upper and lower bounds of the storm system.

[3]. Thus, an approximation of the surface wave pattern around a large maritime storm can be constructed from the wind producing the background oceanic swell and the wind field of the storm near the ocean surface.

The dominant winds produced by a large maritime storm are the result of cyclonic flow around the low pressure at the base of the eye column and the inflow of air into this low pressure region. Large maritime storms are warm core cyclonic weather systems centered about an eye column which has low pressure at its base and high pressure at its peak [37]. An idealized model of the storm structure is shown in Fig. 2. The thin solid lines in the figure denote surfaces of constant pressure. The boundary layer extends from the ocean surface to the altitude at which the storm winds reach a maximum at approximately 1 kilometer above the ocean surface [37]. Large maritime storms typically extend through the troposphere, with cloud layers ending at the tropopause, 10 to 12 kilometers above the ocean surface.

In order to describe the cyclonic winds in the storm, one can write the Euler equation in cylindrical coordinates [37],

$$\frac{1}{\rho}\frac{\partial p}{\partial r} = f_c v_\phi + \frac{v_\phi^2}{r}, \tag{56}$$

where v_ϕ is the cyclonic wind speed and f_c is the Coriolis parameter. Once the storm has reached an intensity such that $f_c \ll \frac{v_\phi}{r}$, this reduces to the cyclostrophic wind equation [37],

$$v_\phi \cong \sqrt{\frac{r}{\rho}\frac{\partial p}{\partial r}}. \tag{57}$$

Differentiating Eq. (56) with respect to altitude allows one to relate the horizontal gradient of the average temperature to the cyclonic wind's vertical gradient. Consider first expanding out the vertical derivative,

$$\frac{\partial}{\partial z}\left[\frac{1}{\rho}\frac{\partial p}{\partial r}\right] = f_c\frac{\partial v_\phi}{\partial z} + 2\frac{v_\phi}{r}\frac{\partial v_\phi}{\partial z},$$
$$\frac{1}{\rho}\frac{\partial}{\partial r}\frac{\partial p}{\partial z} - \frac{1}{\rho^2}\frac{\partial p}{\partial r}\frac{\partial \rho}{\partial z} = \left(f_c + 2\frac{v_\phi}{r}\right)\frac{\partial v_\phi}{\partial z}.$$

From the hydrostatic equation in (15), one can replace $\frac{\partial p}{\partial z} = -\rho g$ while the second term can be simplified by the ideal gas law,

$$\frac{d\rho}{\rho} = \frac{dT}{T} + \frac{dp}{p}, \tag{58a}$$

with some additional approximation. In the troposphere, typical measures of pressure, temperature, and density are of the order 101 to 5.5 kPa, 288 to 216 K, and 1.23 to 0.088 $\frac{\text{kg}}{\text{m}^3}$ respectively [37]. Because the temperature variations are roughly a quarter of the pressure and density, one can approximate the above relation in the troposphere as nearly isothermal,

$$\frac{dp}{p} \cong \frac{d\rho}{\rho}, \tag{58b}$$

which in the case of vertical gradients reduces to $\frac{1}{\rho}\frac{\partial \rho}{\partial z} = \frac{1}{p}\frac{\partial p}{\partial z} = -\frac{\rho g}{p}$. Combining these results, the left hand side of the above simplifies as

$$\begin{aligned}
\frac{1}{\rho}\frac{\partial}{\partial r}\frac{\partial p}{\partial z} - \frac{1}{\rho^2}\frac{\partial p}{\partial r}\frac{\partial \rho}{\partial z} &= -\frac{1}{\rho}\frac{\partial}{\partial r}\rho g + \frac{1}{\rho}\frac{\partial p}{\partial r}\frac{\rho g}{p} \\
&= -\frac{g}{\rho}\frac{\partial \rho}{\partial r} + \frac{g}{p}\frac{\partial p}{\partial r} \\
&= -\frac{g}{\rho}\frac{\partial}{\partial r}\frac{p}{RT} + \frac{g}{p}\frac{\partial p}{\partial r} \\
&= -\frac{g}{\rho R}\left(\frac{1}{T}\frac{\partial p}{\partial r} - \frac{p}{T^2}\frac{\partial T}{\partial r}\right) + \frac{g}{p}\frac{\partial p}{\partial r}.
\end{aligned} \tag{59}$$

The first and last terms cancel and the remaining term can be simplified to give,

$$\left(2\frac{v_\phi}{r} + f_c\right)\frac{\partial v_\phi}{\partial z} = \frac{g}{T}\frac{\partial T}{\partial r}. \tag{60}$$

From this result it is evident that because the cyclonic winds decrease with altitude above the boundary layer, the temperature must decrease away from the eye, thus the storm is a warm core system as expected [37].

Combining the hydrostatic equation in Eq. (15) with the ideal gas law leads to the hypsometric equation [37],

$$(z_2 - z_1) = \frac{R}{g}\bar{T}\ln\left(\frac{p_1}{p_2}\right), \tag{61}$$

which can be used to describe the pressure gradient in a column of air between z_1 and z_2, with average temperature $\bar{T}$. Consider applying this equation to columns of air in the eye and some large distance from the storm,

$$p_{T,\infty} = p_{B,\infty}e^{-\frac{gz_T}{R\bar{T}_\infty}}, \qquad p_{T,\text{eye}} = p_{B,\text{eye}}e^{-\frac{gz_T}{R\bar{T}_\text{eye}}}, \tag{62a}$$

$$\begin{aligned}\Delta p_T &= p_{T,\infty} - p_{T,\text{eye}} = p_{B,\infty}e^{-\frac{gz_T}{R\bar{T}_\infty}} - p_{B,\text{eye}}e^{-\frac{gz_T}{R\bar{T}_\text{eye}}} \\ &= p_{B,\infty}e^{-\frac{gz_T}{R\bar{T}_\infty}} - \left(-\Delta p_B + p_{B,\infty}\right)e^{-\frac{gz_T}{R\bar{T}_\text{eye}}} \\ &= \Delta p_B e^{-\frac{gz_T}{R\bar{T}_\text{eye}}} + p_{B,\infty}\left(e^{-\frac{gz_T}{R\bar{T}_\infty}} - e^{-\frac{gz_T}{R\bar{T}_\text{eye}}}\right).\end{aligned} \tag{62b}$$

One can now define the difference between the ambient temperature and the eye column by $\bar{T}_\text{eye} = \bar{T}_\infty - \Delta\bar{T}$ with $\Delta\bar{T} \ll \bar{T}_\text{eye}, \bar{T}_\infty$. Therefore the term in brackets can be expanded to determine a relation between Δp_T, Δp_B, and $\Delta\bar{T}$ [37].

$$\begin{aligned}\Delta p_T &= \Delta p_B e^{-\frac{gz_T}{R\bar{T}_\text{eye}}} + p_{B,\infty}\left(e^{-\frac{gz_T}{R\bar{T}_\infty}} - e^{-\frac{gz_T}{R}\left(\frac{1}{\bar{T}_\infty} - \frac{\Delta\bar{T}}{\bar{T}_\infty^2} + \ldots\right)}\right) \\ &= \Delta p_B e^{-\frac{gz_T}{R\bar{T}_\text{eye}}} + p_{B,\infty}e^{-\frac{gz_T}{R\bar{T}_\infty}}\left(1 - e^{\frac{gz_T}{R\bar{T}_\infty}\frac{\Delta\bar{T}}{\bar{T}_\infty}}\right) + O\left(\Delta\bar{T}^2\right) \\ &= \Delta p_B e^{-\frac{gz_T}{R\bar{T}_\text{eye}}} - \frac{gz_T}{R\bar{T}_\infty^2}p_{B,\infty}e^{-\frac{gz_T}{R\bar{T}_\infty}}\Delta\bar{T} + O\left(\Delta\bar{T}^2\right).\end{aligned} \tag{62c}$$

Inserting approximate values of $z_T = 15$ km, $\bar{T}_\text{eye} = 293$ K, and ambient pressure $p_{B,\infty} = 101.3$ kPa, this result is approximately,

$$\Delta p_T \cong 0.15\Delta p_B - 0.7\frac{\text{kPa}}{\text{K}}\Delta\bar{T}.$$

This equation demonstrates that because the average temperature in the eye is larger than that outside the storm, Δp_T and Δp_B differ in sign, producing a low pressure region at the base of the eye column and a high pressure region at the top.

In order to proceed any further, a model for the storm energy cycle and dynamics is useful. A large maritime storm converts thermal energy absorbed from the ocean surface into mechanical energy and can therefore be described using an analog of a Carnot heat engine [38, 39, 37]. A thermodynamic diagram, such as that in Fig. 3, can be used to demonstrate how the cyclone extracts energy from the ocean.

Beginning at point (1) in the figure, air at the outer boundaries of the storm moves into the low pressure region at the base of the eye, at point (2). As the air moves across the sea surface in the storm's boundary layer, evaporation saturates the air and the absorbed heat coupled with the pressure decrease leads to an overall constant absolute temperature. That is, the air is drawn from the outer boundary of the storm into the base of the eye isothermally by the pressure gradient at the ocean surface. The moisture and heat absorbed from the active ocean surface are the primary energy source for the storm. From point (2), the air rises moist-adiabatically through the eye column wall. As the air increases in altitude, the temperature decreases, but at a slower rate than the ambient air outside of the storm. Air at the base of the eye may differ in temperature only slightly from air outside the storm at ocean level, however at increased altitudes the temperature difference increases. The temperature, pressure, and saturation of the air rising through the eye wall are coupled in such a way that this transition preserves entropy [37].

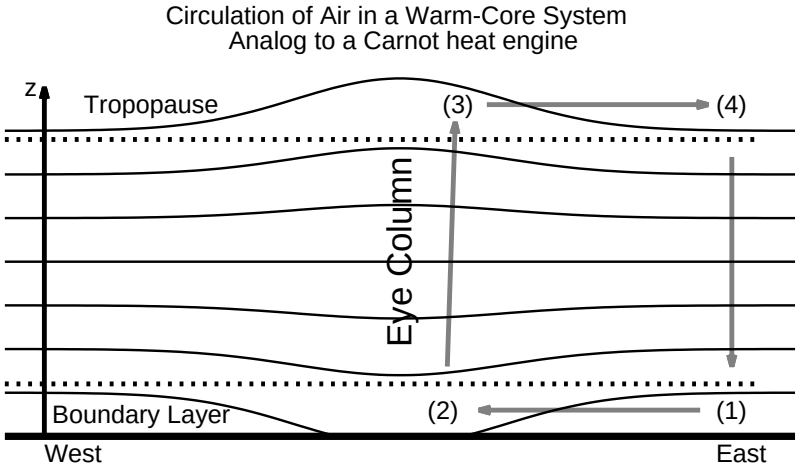

Fig. 3: Air circulation and thermodynamic diagram of a large maritime storm.

Once the air reaches the top of the eye column, point (3), the high pressure forces the air to spiral outward over the storm structure at roughly constant altitude. During this outflow, the air loses heat due to infrared radiation into the tropopause and the temperature decreases to the ambient value at that altitude. Lastly, the air subsides back dry-adiabatically towards the ocean surface, warming as it does so. This returns the air to the initial region at point (1), where the cycle continues until the storm moves over cooler water or a large land mass and the energy source is no longer present.

The gaining of entropy at one temperature (during inflow along the ocean surface) and the loss of entropy at another temperature (during outflow in the tropopause) allows the storm to produce mechanical energy at a rate according to [37]

$$E_{\text{mech}} = \Delta T \Delta s_B, \tag{63}$$

where ΔT is the different in average temperature at the base of the storm, between points (1) and (2), and the top of the storm, between points (3) and (4), and Δs is the entropy gained by the air in moving from point (1) to (2). This mechanical energy is the driving mechanism for the winds and resulting ocean surface waves

Given this simple model, we now seek some description of the temperature and winds in the boundary layer of the storm where a positive wind gradient is likely to produce an acoustic duct. As mentioned in the previous discussion, the movement of air from point (1) to (2) in Fig 3 is isothermal and therefore at the ocean surface and in the boundary layer the horizontal temperature gradients are negligible. Because the air moving from point (1) to (2) absorbs moisture from the ocean surface, a correction to the thermodynamic sound speed can be made due to the introduction of H_2O. At leading order, for a fraction, h, of H_2O molecules in air, the thermodynamic sound speed increases by [6],

$$c_{\text{wet}} = [1 + 0.16h]\, c_{\text{dry}}. \tag{64}$$

At 40^o C, 100% humidity corresponds to $h = 0.07$ which results in a moist thermodynamic sound speed correction of less than 1.5%. Such a small difference will be insignificant relative to the wind gradients. Thus for the purpose of this analysis, we will not consider any variations in the

thermodynamic sound speed due to the horizontal temperature and humidity gradients.

The cyclonic winds at the top of the boundary layer can be calculated using a model for the pressure distribution and Euler's equation in Eq. (56). The pressure distribution at the top of the boundary layer of a large maritime storm can be approximately fit by

$$r^B \ln \frac{p_\infty - p_{\text{eye}}}{p(r) - p_\infty} = A, \tag{65}$$

where A and B are scaling parameters [40]. Rearranging this equation,

$$p\,(r) = p_{\text{eye}} + \Delta p\, e^{-\frac{A}{r^B}}. \tag{66}$$

Combining this form of $p(r)$ with Eq. (56), the cyclonic wind profile at the top of the boundary layer is found to be

$$v_\phi\,(r) = \sqrt{\frac{AB\Delta p}{\rho r^B}\, e^{-\frac{A}{r^B}} + \frac{r^2 f_c^2}{4}} - \frac{r f_c}{2}, \tag{67}$$

which reduces to

$$v_\phi\,(r) = v_{\max}\sqrt{\left(\frac{r_m}{r}\right)^B e^{1-\left(\frac{r_m}{r}\right)^B}}, \tag{68}$$

when one neglects the Coriolis terms [40]. In this final form, we've written the cyclonic winds in terms of the maximum winds and radius of maximum winds which are given by

$$r_m = A^{\frac{1}{B}}, \qquad v_{\max} = \sqrt{\frac{B\,\Delta p}{\rho e}}.$$

This cyclonic wind model was developed by G. J. Holland in a 1980 publication and subsequently updated in 2010 by replacing the square root with an additional parameter x resulting in [40, 41],

$$v_\phi\,(r) = v_{\max}\left[\left(\frac{r_m}{r}\right)^B e^{1-\left(\frac{r_m}{r}\right)^B}\right]^x. \tag{69}$$

An explanation of how to compute B, x, and $v_{\max}$ from observations of Δp are given in the updated publication, however such methods are intended to assist in fitting measured wind data and are not applicable to this project. Here we will use the cyclonic wind profile in Eq. (68) with $B = 1.5$, $r_m = 50$ km, and $v_{\max}$ dependent on model storm strength. The value of r_m is chosen to fall within

the average of observed values which range between 30 and 60 km with observed extrema between 8 and 200 km [37]. The maximum winds chosen for each storm intensity are near the upper limit of the Saffir-Simpson scale for that strength storm. Exact wind speeds used in analysis are listed in Table 1 at the end of this section.

The model developed by Holland models only the cyclonic wind, v_ϕ. A more realistic storm model would also include the radial winds, v_r which are directed inwards, towards the eye column, and typically on the order of 1/5 the magnitude of the cyclonic wind [37]. A small vertical component of the wind exists in the eye column itself, but it is two orders of magnitude smaller than the cyclonic winds and has been neglected in the development of this storm model. In order to approximate the radial wind component near the ocean surface, we refer to the boundary layer equations for a axisymmetric vortex in a homogeneous fluid [42],

$$\frac{1}{r}\frac{\partial}{\partial r}\left(rv_r^2\right) + \frac{\partial}{\partial z}\left(v_r w\right) + \frac{v_{\mathrm{gr}}^2 - v_\phi^2}{r} + f_c\left(v_{\mathrm{gr}} - v_\phi\right) = \frac{\partial}{\partial z}\left(K\frac{\partial v_r}{\partial z}\right), \tag{70a}$$

$$\frac{1}{r^2}\frac{\partial}{\partial r}\left(r^2 v_r v_\phi\right) + \frac{\partial}{\partial z}\left(v_\phi w\right) + f_c v_r = \frac{\partial}{\partial z}\left(K\frac{\partial v_\phi}{\partial z}\right), \tag{70b}$$

$$\frac{1}{r}\frac{\partial}{\partial r}\left(rv_r\chi\right) + \frac{\partial}{\partial z}\left(v_z\chi\right) = \frac{\partial}{\partial z}\left(K\frac{\partial \chi}{\partial z}\right), \tag{70c}$$

$$\frac{\partial}{\partial r}\left(rv_r\right) + \frac{\partial}{\partial z}\left(rv_z\right) = 0, \tag{70d}$$

where v_r, v_ϕ, v_z are the three components of velocity, $v_{\mathrm{gr}}(r)$ is the tangential wind speed at the top of the boundary layer, f_c is again the Coriolis parameter, χ is a scalar quantity related to the dry static energy or specific humidity, and K is the eddy diffusivity. Some manipulation of these equations leads to,

$$v_{r,b}\frac{dv_{r,b}}{dr} = v_{r,b}\frac{v_{z,-}}{\delta} - \frac{v_{\mathrm{gr}}^2 - v_{\phi,b}^2}{r} - f_c\left(v_{\mathrm{gr}} - v_{\phi,b}\right) - \frac{C_D}{\delta}v_{r,b}\sqrt{v_{r,b}^2 + v_{\phi,b}^2}, \tag{71a}$$

$$v_{r,b}\frac{dv_{\phi,b}}{dr} = \frac{v_{z,-}}{\delta}\left(v_{\phi,b} - v_{\mathrm{gr}}\right) - \left(\frac{v_{\phi,b}}{r} + f_c\right)v_{r,b} - \frac{C_D}{\delta}v_{\phi,b}\sqrt{v_{r,b}^2 + v_{\phi,b}^2}, \tag{71b}$$

where the subscript b's denote the value at the top of the boundary layer, $w_{z,-}$ is the vertical wind component averaged below the boundary layer, C_D is the drag coefficient, and δ is the boundary layer depth [42]. In this second result, one can make an approximation by neglecting variations in

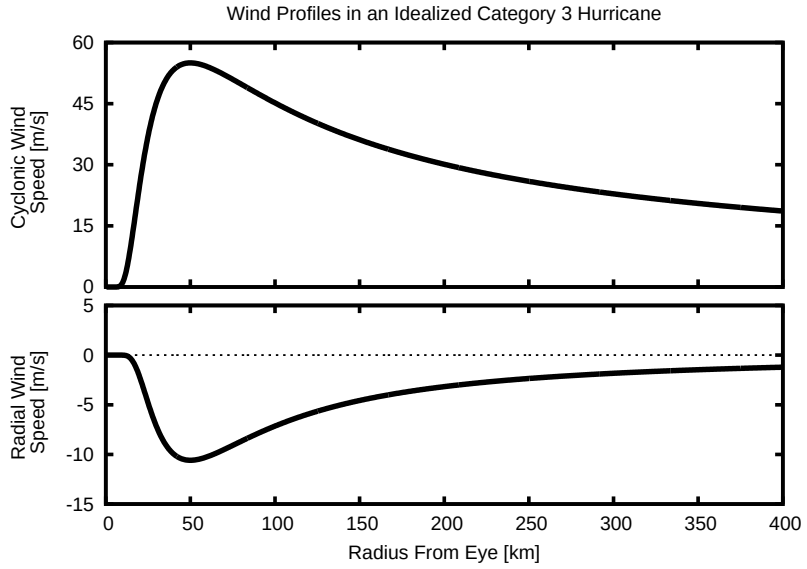

Fig. 4:
The cyclonic wind, $v_\phi(r)$, (upper) and radial wind, $v_r(r)$, (lower) at the top of the boundary layer, approximately 1 kilometer above the ocean surface, of a large maritime storm as expressed in Eq. (68) and (73) respectively.

the vertical advection term, resulting in [42, 43]

$$v_{r,b} = -\frac{C_D}{\delta}\frac{v_{\phi,b}^2}{\zeta_a}, \qquad \zeta_a = \frac{dv_{\phi,b}}{dr} + \frac{v_{\phi,r}}{r} + f_c. \tag{72}$$

Thus, the radial component of the winds varies approximately as the square of the cyclonic wind component, scaled by a factor depending on the drag coefficient, C_D, the boundary layer depth, δ, and the vertical component of the absolute vorticity in the boundary layer, ζ_a. Following the simplified storm model presented by Stull, we can approximate the radial winds by,

$$v_r\left(r\right) \cong -3.5 v_\phi^2\left(r\right), \tag{73}$$

which produces the observed coupling of $|v_{r,\max}| \sim \frac{1}{5}\left|v_{\phi,\max}\right|$ relation [37].

The resulting wind models are shown in Fig. 4 for a Category 3 storm. Note that while $v_\phi(r)$ decreases as $\left(\frac{r_m}{r}\right)^{\frac{b}{2}}$ for $r \gg r_m$, the radial winds, $v_r(r)$ decrease as $\left(\frac{r_m}{r}\right)^{b}$. In an idealized axisymmetric vortex, one sets $b = 1$, resulting in $v_\phi \sim \frac{1}{\sqrt{r}}$ and $v_r \sim \frac{1}{r}$ which are consistent with conservation of potential vorticity and mass inflow respectively [38, 44, 37]. In Holland's model, the variability in b allows one to allows some loss in vorticity and inflow and produce a more realistic wind profile.

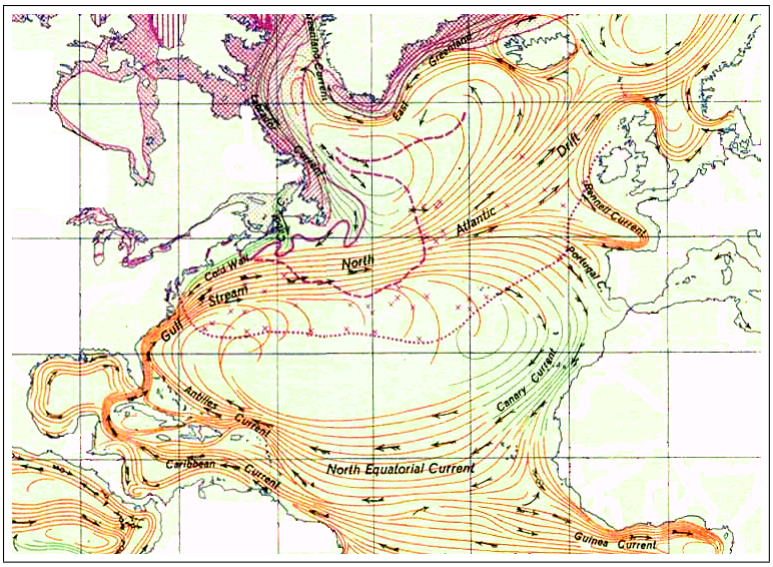

Fig. 5: The dominant currents in the northern Atlantic Ocean. The storms of interest to this project interact with the North Equatorial Current in the lower center of the figure.

Locating the Microbarom Source Region

We can now infer from the previous discussion that the storm winds in Eq. (68) and (73) will produce a surface wave field on the ocean surface beneath the storm with waves propagating in the direction of the winds and wavelengths dependent on the wind speed. In addition to these waves, a background swell exists in the open Atlantic which interacts with the swell produced by the storm.

In the open north Atlantic where low pressure regions form, the dominant background swell is due to the North Equatorial and Canary Currents shown in Fig. 5 [45, 46]. These currents produce a background swell in the open Atlantic which is dominated by flow from east to west. Nearer to the North American continent, the Gulf Stream and Antilles Currents complicate the background swell significantly. Additionally, reflections from the eastern coast of North America produce additional complications of the background swell. The complications of multiple currents contributing to the background swell and possible reflections from the continent could produce localized variations in the directionality of the background swell, however such concerns are beyond the scope of this preliminary investigation into the microbarom signal produced by the storm. For the purpose of this analysis, it is assumed that the storm is far from any land mass and the background swell is dominated by winds directed from east to west.

It was previously shown that a flow above a fluid-fluid interface generates a forcing in the direction of the flow. For a steady wind over an interface, the surface waves would asymptotically

reach a velocity equal to that of the wind. Therefore, one can use the deep water dispersion relation,

$$\frac{g\lambda}{2\pi} = c_{\text{surf}}^2, \tag{74}$$

to infer that, to leading order, a steady wind, $\vec{v}_0$, over the open ocean will generate propagating surface waves in the direction of the wind with wave length, $\lambda = 2\pi\frac{|v_0|^2}{g}$. Additional corrections can be made to account for surface tension of the interface and other effects, however this relation holds to leading order.

In the case of our model storm, this coupling produces two surface wave fields, shown in Fig. 6. The storm winds in Eq. (68) and (73) generate a surface wave field underneath the storm, shown in the upper row of the figure. The background oceanic swell and its associated wind are shown in the lower part of the figure. The two wave fields interact as seen in the right-most panel of the figure. The generation of microbaroms is dependent on the head-on collision of surface waves with equal wavelength. The red ring denotes the regions in which the wavelength of the storm wave field is equal to that of the background. Within this region, collisions between counter propagating waves is expected to produce microbarom radiation. The storm induced and background swell have waves propagating in directions denoted with black and blue arrows respectively. It is evident that the microbarom source region due to these interacting wave field is located approximately 500 kilometers south of the storm eye where the storm induced waves and background swell are both counter propagating and equal in wavelength.

Thus, for a large maritime storm producing a cyclonic ocean surface wave pattern due to the coupling of the storm winds to the ocean surface, there is expected to be a region outside of the strong storm winds in which the swell generated by the storm winds is equal in wavelength but opposite in propagation direction to the background ocean swell. In such a region, infrasonic energy can be radiated into the atmosphere and ocean. The acoustic energy radiated away from the storm winds will propagate with weak horizontal refraction and is observable at locations south of the storm in the case of a hurricane in the Atlantic. Alternately, the acoustic energy which propagates into the storm will interact with the strong storm winds and, possibly, be detectable on the far side of the storm.

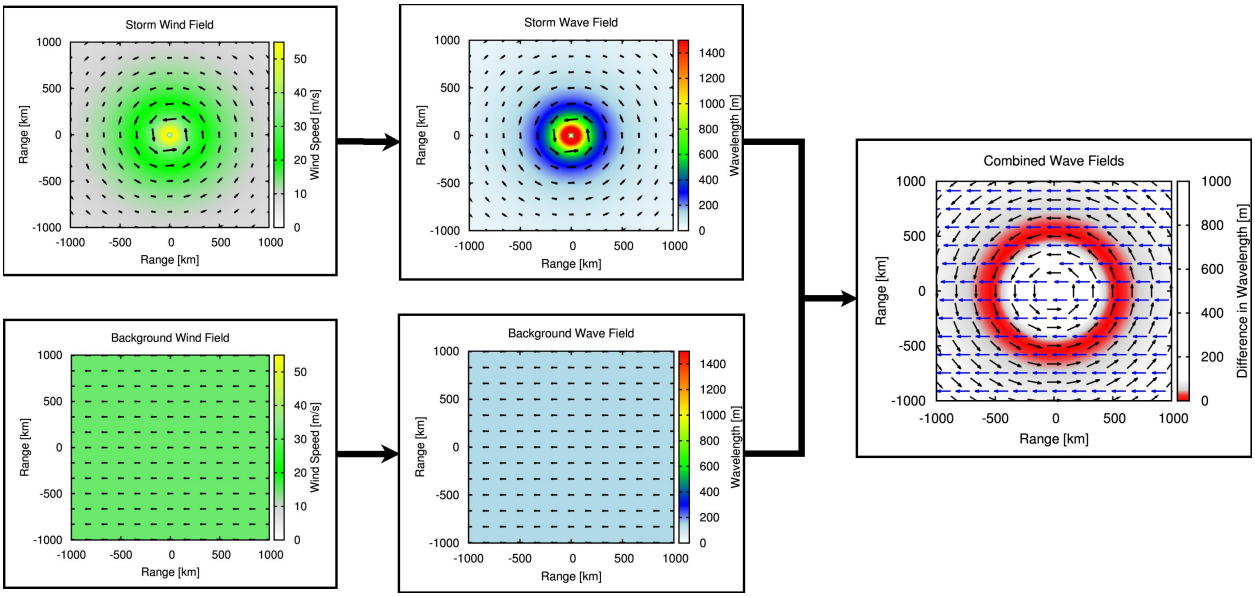

Fig. 6: The interaction of the wave fields produced by the storm winds with the background swell provides a method to infer where the microbaroms are generated by a large maritime storm.

Saffir-Simpson Hurricane Scale		
Storm Intensity	Cyclonic Wind Range	$v_{\max}$
Tropical Depression	$< 17 \frac{\mathrm{m}}{\mathrm{s}}$	Not Used
Tropical Storm	$17 - 32 \frac{\mathrm{m}}{\mathrm{s}}$	Not Used
Category 1	$33 - 42 \frac{\mathrm{m}}{\mathrm{s}}$	$40 \frac{\mathrm{m}}{\mathrm{s}}$
Category 2	$43 - 49 \frac{\mathrm{m}}{\mathrm{s}}$	$48 \frac{\mathrm{m}}{\mathrm{s}}$
Category 3	$50 - 57 \frac{\mathrm{m}}{\mathrm{s}}$	$55 \frac{\mathrm{m}}{\mathrm{s}}$
Category 4	$58 - 69 \frac{\mathrm{m}}{\mathrm{s}}$	$65 \frac{\mathrm{m}}{\mathrm{s}}$
Category 5	$> 70 \frac{\mathrm{m}}{\mathrm{s}}$	$75 \frac{\mathrm{m}}{\mathrm{s}}$

Table 1: The Saffir-Simpson Hurricane Scale classifies storms based on maximum cyclonic wind speed. (73).

CHAPTER 3

PROPAGATION OF MICROBAROMS THROUGH THE STORM WINDS

In a uniform motionless medium, acoustic energy radiates away from the source spherically. However, in the case of a medium with variations in temperature and flow velocity, the wavefront is deformed due to different regions propagating faster or slower than others. The approximation of geometric acoustics is a useful tool for visualizing this deformation of wavefronts in the high frequency limit. Geometric acoustics neglects effects of diffraction and scattering, however such phenomena are dominant only if the characteristic scale of variations in the medium are of the same scale as the wavelength of the acoustic waves propagating through the medium.

In the case of microbaroms, the wavelength is approximately 1.7 kilometers. The cyclonic wind field of a large maritime storm is characterized by a radius of maximum winds which is typically on the order of 50 kilometers. Therefore, the horizontal refraction effects of microbaroms propagating through the wind field of a large maritime storm is well described by geometric acoustics. Additionally, the orientation of the wavefront detected far from the storm winds, which we intend to use as a diagnostic of the storm, can be easily calculated with geometric acoustics.

Geometric Acoustics in Three Dimensions

The propagation of acoustic energy can be described by a linear perturbation of the fluid mechanics equations in Chapter 2. Using the results of the ambient state, the linear order continuity, Euler, and state equations have the forms [7],

$$\frac{D\rho}{Dt} + \rho\vec{\nabla}\cdot\vec{v}_0 + \vec{\nabla}\cdot(\rho_0\vec{v}) = 0, \tag{75a}$$

$$\frac{D\vec{v}}{Dt} + \left(\vec{v}\cdot\vec{\nabla}\right)\vec{v}_0 = -\frac{1}{\rho_0}\vec{\nabla}p + \rho\vec{\nabla}\frac{p_0}{\rho_0^2}, \tag{75b}$$

$$\vec{v}\cdot\vec{\nabla}p_0 + \frac{Dp}{Dt} = c^2\left[\vec{v}\cdot\vec{\nabla}\rho_0 + \frac{D\rho}{Dt}\right] + \left(c^2\right)'\vec{v}_0\cdot\vec{\nabla}\rho_0, \tag{75c}$$

where we've dropped the subscript 1's since there are no higher order terms. The approximation of geometric acoustics is constructed by expanding each variable with a spatially varying phase, $e^{ik_0\psi(\vec{x})}$, and Debye series, $\sum \frac{\mathcal{P}_j(\vec{x})}{(ik_0)^j}$. The phase function, $\psi(\vec{x})$, is termed the Eikonal and its solution provides information about the deformation of surfaces of constant phase. Expanding each linear variable,

$$\begin{pmatrix} p \\ \vec{v} \\ \rho \\ \left(c^2\right)' \end{pmatrix} = e^{ik_0\psi(\vec{x})}\sum_{j=0}^{\infty}\frac{1}{(ik_0)^j}\begin{pmatrix} \mathcal{P}_j(\vec{x}) \\ \vec{\mathcal{V}}_j(\vec{x}) \\ \mathcal{D}_j(\vec{x}) \\ \mathcal{C}_j(\vec{x}) \end{pmatrix}. \tag{76}$$

Under the further assumption of harmonic time dependence, $p \sim e^{-i\omega_0 t} = e^{-ik_0c_0t}$, one can reduce Eq. (75) to expansions in powers of k_0. For reference, whenever $\vec{\nabla}$ acts on one of the expanded variables in Eq. (76), one has

$$\vec{\nabla}p = \sum_{j=0}^{\infty}\frac{1}{(ik_0)^j}\left[ik_0\mathcal{P}_j\vec{\nabla}\psi + \vec{\nabla}\mathcal{P}_j\right]e^{ik_0\psi}. \tag{77}$$

The linearized fluid mechanics equations can then be written as,

$$\sum_{j=0}^{\infty}\frac{1}{(ik_0)^j}\Big\{ -ik_0\mathcal{D}_j\left(c_0 - \vec{v}_0\cdot\vec{\nu}\right) + \vec{v}_0\cdot\vec{\nabla}\mathcal{D}_j + \mathcal{D}_j\vec{\nabla}\cdot\vec{v}_0 + \rho_0\vec{\nabla}\cdot\vec{\mathcal{V}}_j + \rho_0 ik_0\vec{\mathcal{V}}_j\cdot\vec{\nu} + \vec{\mathcal{V}}_j\cdot\vec{\nabla}\rho_0\Big\} = 0, \tag{78a}$$

$$\sum_{j=0}^{\infty}\frac{1}{(ik_0)^j}\left\{-ik_0\vec{\mathcal{V}}_j\left(c_0 - \vec{v}_0\cdot\vec{\nu}\right) + \vec{v}_0\cdot\vec{\nabla}\vec{\mathcal{V}}_j + \vec{\mathcal{V}}_j\cdot\vec{\nabla}\vec{v}_0\right\} = \sum_{j=0}^{\infty}\frac{1}{(ik_0)^j}\left\{-\frac{ik_0}{\rho_0}\mathcal{P}_j\vec{\nu} - \frac{1}{\rho_0}\vec{\nabla}\mathcal{P}_j + \mathcal{D}_j\vec{\nabla}\frac{p_0}{{\rho_0}^2}\right\}, \tag{78b}$$

$$\sum_{j=0}^{\infty} \frac{1}{(ik_0)^j} \left\{ \vec{\mathcal{V}}_j \cdot \vec{\nabla} p_0 - ik_0 \mathcal{P}_j \left(c_0 - \vec{v}_0 \cdot \vec{\nu} \right) + \vec{v}_0 \cdot \vec{\nabla} \mathcal{P}_j \right\}$$

$$= \sum_{j=0}^{\infty} \frac{1}{(ik_0)^j} \Big\{ c^2 \left[\vec{\mathcal{V}}_j \cdot \vec{\nabla} \rho_0 - ik_0 \mathcal{D}_j \left(c_0 - \vec{v}_0 \cdot \vec{\nu} \right) + \vec{v}_0 \cdot \vec{\nabla} \mathcal{D}_j \right]$$

$$+ \mathcal{C}_j \vec{v}_0 \cdot \vec{\nabla} \rho_0 \Big\}, \tag{78c}$$

where we've simplified the notation by defining $\vec{\nu} = \vec{\nabla}\psi$. Collecting terms in powers of k_0 one finds the leading order contributions to be:

$$\left(1 - \frac{\vec{v}_0 \cdot \vec{\nu}}{c_0} \right) \mathcal{D}_0 = \frac{\rho_0}{c_0} \vec{\mathcal{V}}_0 \cdot \vec{\nu}, \tag{79a}$$

$$\left(1 - \frac{\vec{v}_0 \cdot \vec{\nu}}{c_0} \right) \vec{\mathcal{V}}_0 = \frac{1}{\rho_0 c_0} \mathcal{P}_0 \vec{\nu}, \tag{79b}$$

$$\mathcal{P}_0 = c^2 \mathcal{D}_0. \tag{79c}$$

Combining Eq. (79a) and (79c),

$$\left(1 - \frac{\vec{v}_0 \cdot \vec{\nu}}{c_0} \right) \mathcal{P}_0 = \frac{\rho_0 c^2}{c_0} \vec{\mathcal{V}}_0 \cdot \vec{\nu}. \tag{80}$$

Finally, combining Eq. (80) with (79b),

$$\nu^2 = \frac{c_0^2}{c^2} \left[1 - \frac{\vec{v}_0 \cdot \vec{\nu}}{c_0} \right]^2, \tag{81}$$

which is the Eikonal equation for propagation in three dimensions [8, 9]. A dispersion relation can be found by assuming a wave vector $\vec{k} = k_0 \vec{\nu}$. From Eq. (81),

$$\frac{k^2}{k_0^2} = \frac{k^2 c_0^2}{\omega^2} = \frac{c_0^2}{c^2} \left(1 - \frac{\vec{v}_0 \cdot \vec{k}}{\omega} \right)^2 \quad \rightarrow \quad \omega = kc + \vec{k} \cdot \vec{v}_0, \tag{82}$$

which results in a propagation velocity,

$$\vec{c}_p = \frac{\partial \omega}{\partial \vec{k}} = c \frac{\vec{\nu}}{\nu} + \vec{v}_0. \tag{83}$$

Thus the sound propagates in the direction defined by $\hat{n}_\nu c + \vec{v}_0$ where c is the thermodynamic sound

speed and $\vec{v}_0$ is the ambient wind in the propagation medium. From this result, it is immediately clear that $\vec{c}_p \cdot \vec{\nu} = \vec{v}_0 \cdot \vec{\nu} + c\nu = c_0$. The differential equations describing the geometric ray paths can be determined by using Hamilton-Jacobi relations,

$$\frac{\partial \vec{x}}{\partial \tau} = \frac{\partial H}{\partial \vec{\nu}}, \qquad \frac{\partial \vec{\nu}}{\partial \tau} = -\frac{\partial H}{\partial \vec{x}}, \tag{84a}$$

$$H = \frac{1}{2}\left[\nu^2 - \frac{1}{c^2}\left(c_0 - \vec{v}_0 \cdot \vec{\nu}\right)^2\right] = 0, \tag{84b}$$

which results in the coupled differential equations,

$$\frac{\partial \vec{x}}{\partial s} = \frac{\vec{c}_p}{c_p}, \tag{85a}$$

$$\frac{\partial \nu_j}{\partial s} = -\frac{1}{c_p}\left[\nu \frac{\partial c}{\partial x_j} + \vec{\nu} \cdot \frac{\partial \vec{v}_0}{\partial x_j}\right], \tag{85b}$$

where we've changed variables from the unitless quantity τ into physical ray length s. The next terms in the expansion, those proportional to k_0 in Eq. (78), can be used to construct the Transport equation defining $\mathcal{P}_0(\vec{x})$ [9]. The amplitude coefficient will not be used extensively in this analysis, and therefore we include the derivation and result of the Transport equation separately in Appendix A.

Before continuing with this analysis, it is critically important to identify the conditions in which the approximation of geometric acoustics is valid. It can be shown that the approximation is not an accurate description of the physics involved in propagation in the case that (1) the radius of curvature of the rays is of the order or smaller than the wavelength, (2) the velocity of propagation changes appreciably over the distance of a wavelength, or (3) the percentage change in amplitude is large over the distance of a wavelength [47]. The curvature of rays is determined by the gradients of the propagation medium, and as noted earlier, the storm winds increase radially at a rate which is within the limits of applicability for geometric acoustics. However, the vertical structure of the storm winds is less well defined. The storm winds increase from zero at the ocean surface to their maximum intensity at an altitude of 1-2 kilometers above the ocean surface. This produces a very thin, strongly downward refracting duct in the storm boundary layer. The results of geometric propagation modeling in this region will be discussed in the later part of this chapter,

with additional results using a full wave model to evaluate the effectiveness of the duct in Appendix B.

Initializing and Reflecting Ray Paths

The initial conditions for tracing a ray can be found using simple geometric analysis of the source region. Within a small region around the source, the medium can be approximated as homogeneous and the acoustic energy radiates spherically [9, 48, 49],

$$\begin{pmatrix} x\left(s,\theta,\phi\right) \\ y\left(s,\theta,\phi\right) \\ z\left(s,\theta,\phi\right) \end{pmatrix} = \begin{pmatrix} x_{\text{src}} + s\cos\theta\cos\phi + O\left(s^2\right) \\ y_{\text{src}} + s\cos\theta\sin\phi + O\left(s^2\right) \\ z_{\text{srs}} + s\sin\theta + O\left(s^2\right) \end{pmatrix}. \tag{86}$$

where θ is the angle the ray initially makes with the horizontal and ϕ is the azimuth angle defined relative to the x axis. The coordinate system defined by s, θ, ϕ are termed ray coordinates. In our case the source is located at the ocean surface some distance from the storm center,

$$\begin{pmatrix} x\left(0,\theta,\phi\right) \\ y\left(0,\theta,\phi\right) \\ z\left(0,\theta,\phi\right) \end{pmatrix} = \begin{pmatrix} x_{\text{src}} + O(s) \\ y_{\text{src}} + O(s) \\ O(s) \end{pmatrix} = \begin{pmatrix} x_{\text{src}} \\ y_{\text{src}} + \\ 0 \end{pmatrix}. \tag{87}$$

In order to determine initial conditions for $\vec{\nu}$, we reference Eq. (83) and (85a),

$$\begin{aligned} \frac{\partial \vec{r}}{\partial s} = \frac{\vec{c}_p}{c_p} &= \frac{c\frac{\vec{\nu}}{\nu} + \vec{v}_0}{\left| c\frac{\vec{\nu}}{\nu} + \vec{v}_0 \right|} \\ &= \frac{\frac{\vec{\nu}}{\nu} + \frac{\vec{v}_0}{c}}{\sqrt{1 + 2\frac{\vec{\nu}\cdot\vec{v}_0}{c\nu} + \frac{v_0^2}{c^2}}}. \end{aligned} \tag{88}$$

This equation cannot be solved explicitly for ν, and therefore we cannot find a direct relation for $\vec{\nu}_0\left(\theta,\phi\right)$. In practice this doesn't cause a problem because one can define an initial vector direction $\hat{\nu}$ and scale the vector so that it satisfies the eikonal equation at the source,

$$|\nu| = 1 - \vec{\nu}\cdot\frac{\vec{v}_0}{c_0} \quad \rightarrow |\nu| = \frac{1}{1 + \hat{\nu}\cdot\frac{\vec{v}_0}{c_0}}, \tag{89}$$

However, it must be noted that the direction of $\vec{\nu} = |\nu|\,\hat{\nu}$ and $\frac{\partial \vec{r}}{\partial s}$ are not parallel unless the wind is negligible at the source. This is true in the case of a source located at the ground or ocean surface where the winds go to zero, and therefore one finds,

$$\frac{\partial \vec{r}}{\partial s} = \frac{c\frac{\vec{\nu}}{\nu}}{\left|c\frac{\vec{\nu}}{\nu}\right|} = \frac{\vec{\nu}}{\nu} = \vec{\nu}\frac{c}{c_0}, \tag{90}$$

and near the source,

$$\vec{\nu}\Big|_0 = \frac{c_0}{c}\frac{\partial \vec{r}}{\partial s} = \begin{pmatrix} \cos\theta\cos\phi + O(s) \\ \cos\theta\sin\phi + O(s) \\ \sin\theta + O(s) \end{pmatrix}. \tag{91}$$

To determine the initialization values following a ground reflection, the spherical spreading method used to determine the values at the source can be applied, with the ray path length, s, and range, $r\,(x, y)$, shifted to those of the incident path,

$$\begin{pmatrix} x\,(s,\theta,\phi) \\ y\,(s,\theta,\phi) \\ z\,(s,\theta,\phi) \end{pmatrix} = \begin{pmatrix} x_0\,(\theta,\phi) + (s - s_0\,(\theta,\phi))\cos\theta_{\text{ref}}\cos\phi_{\text{ref}} + O\left([s - s_0(\theta,\phi)]^2\right) \\ y_0\,(\theta,\phi) + (s - s_0\,(\theta,\phi))\cos\theta_{\text{ref}}\sin\phi_{\text{ref}} + O\left([s - s_0(\theta,\phi)]^2\right) \\ |s - s_0\,(\theta,\phi)|\sin\theta_{\text{ref}} + O\left([s - s_0(\theta,\phi)]^2\right) \end{pmatrix}. \tag{92}$$

Additionally, in the case of a range dependent medium, the angle the ray paths makes with the ground at reflection is not necessarily equal to the angle made at the source. The known relations between $\frac{\partial \vec{r}}{\partial s}$ and $\vec{\nu}$ can be used to determine the angle at the reflection point. Some simple geometric analysis produces

$$\theta_{\text{ref}} = -\sin^{-1}\left(\nu_{z0}\right), \tag{93a}$$

$$\phi_{\text{ref}} = \tan^{-1}\left(\frac{\nu_{y0}}{\nu_{x0}}\right), \tag{93b}$$

where we've denoted quantities associated with ground intercept of the incident ray path with subscript zeros. Again making the assumption that the wind at the ground is negligible, the

conditions for $\vec{x}$ and $\vec{\nu} = \frac{c(0)}{c(\vec{x})}\frac{\partial \vec{x}}{\partial s}$ give,

$$\vec{x}\Big|_{s_0} = \begin{pmatrix} x_0(\theta,\phi) + O([s - s_0(\theta,\phi)]) \\ y_0(\theta,\phi) + O([s - s_0(\theta,\phi)]) \\ O([s - s_0(\theta,\phi)]) \end{pmatrix} = \begin{pmatrix} x_0(\theta,\phi) \\ y_0(\theta,\phi) \\ 0 \end{pmatrix}, \tag{94a}$$

$$\vec{\nu}\Big|_{s_0} = \begin{pmatrix} \cos\theta_{\text{ref}}\cos\phi_{\text{ref}} + O([s - s_0(\theta,\phi)]) \\ \cos\theta_{\text{ref}}\sin\phi_{\text{ref}} + O([s - s_0(\theta,\phi)]) \\ \text{sgn}[s - s_0(\theta,\phi)]\sin\theta_{\text{ref}} + O([s - s_0(\theta,\phi)]) \end{pmatrix} = \begin{pmatrix} \nu_{x0}(\theta,\phi) \\ \nu_{y0}(\theta,\phi) \\ -\nu_{z0}(\theta,\phi) \end{pmatrix}. \tag{94b}$$

The initialization and reflection conditions for the angular derivatives necessary to calculate the amplitude coefficient are presented in Appendix A.

Propagation Through the Wind Field of a Large Maritime Storm

In this section, the refraction of acoustic energy by the winds of a large maritime storm is discussed. Using the ray path equations in Eq. (85), a qualitative discussion of refraction effects of the storm winds is given, followed by a discussion of the numerically produced results describing propagation in a two dimensional axisymmetric planar model of sound propagating through the top of the boundary layer of a storm as well as a vertically varying storm. The physics of acoustic propagation through the storm winds, though complicated, can be physically modeled using the approximation of geometric acoustics.

The propagation equations in Eq. (85) provide a quantitative description of how variations in the propagation medium affect sound. From this pair of differential equations, one can produce a qualitative understanding of how ambient flow in the medium and gradients in the sound speed and ambient flow will affect propagating sound. Consider a small packet of an acoustic disturbance with leading and trailing edges described by surfaces of constant phase as given in Fig. 7. The packet of acoustic energy is localized such that the leading and trailing edges are parallel. Because we've defined $\vec{\nu} = \vec{\nabla}\psi(\vec{x})$, the vector $\vec{\nu}$ is perpendicular to the leading surface and indicates the direction in which the disturbance propagates in the absence of ambient flow. From Eq. (85a) and the definition of $\vec{c}_p$, it is evident that the disturbance propagates forward along $\hat{n}_\nu$ with speed c and is shifted in the direction of the winds $\vec{v}_0$. Note that the $\vec{v}_0$ term in Eq. (85a) does not produce a

refraction effect but merely displaces the packet of acoustic energy.

The differential relation in Eq. (85b) describes how gradients in c and $\vec{\nu} \cdot \vec{v}_0$ produce refraction effects, which change the propagation direction $\hat{n}_\nu$. In the left side of Fig. 7, ambient flow is neglected and a gradient is present in the propagation velocity. For a medium in which c increases to the left, the vector $\vec{\nu}$ is refracted to the right. The physical reason for this refraction is that the surface of constant phase is distorted by the left side propagating faster than the right side. Similar refraction occurs for gradients in the ambient flow, however only if the disturbance is propagating in the appropriate direction. If $\nu_j = 0$, refraction will not occur even if $\frac{\partial v_{0,j}}{\partial x_i}$ is non-zero.

The orientation of the signal as it passes through the upper region of the left and right sides of Fig. 7 demonstrates how the refraction can be measured. In each case, the plane perpendicular to $\tilde{\vec{\nu}}$ can be determined and used to determine the direction from which the signal appears to be emanating, shown as a blue arrow in the figure. As mentioned in Chapter 1, strong cross-winds and horizontal gradients can produce errors when using the back azimuth as the azimuth to true source location. In the left panel of the figure, the displacement of the signal results in a back azimuth indicating that the source is directly south. Alternately, in the right figure, the back

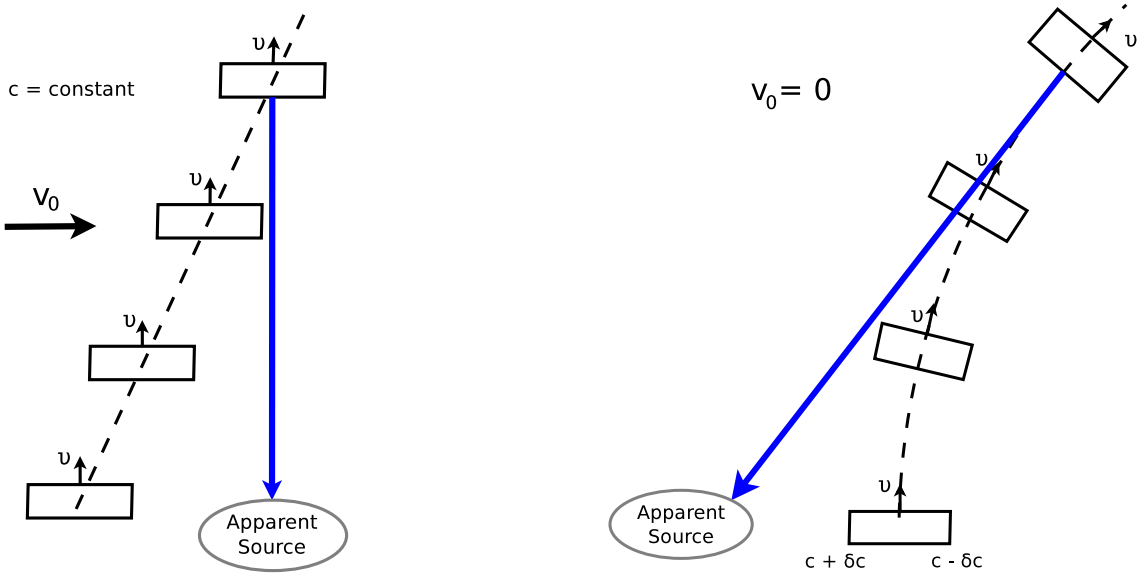

Fig. 7: The two types of effects in geometric propagation as described in Eq. (85) are visualized using a small packet of acoustic energy. The packet propagates in the direction $\hat{n}_\nu$ at speed c with additional propagation in the flow direction $\vec{v}_0$ (left). A gradient in the thermodynamic sound speed, c, (or flow velocity in the direction of propagation, $\vec{\nu} \cdot \vec{v}_0$) results in refraction of the sound (right).

azimuth would point to the south west, indicating an apparent source to the west of the actual one. Using geometric acoustics as a model for propagation, one is able to quantify how the propagation medium produces a given back azimuth at the receiver and correct the propagation effects in order to more accurately estimate the true source location.

This is the set up for most propagation problems, the received data is used along with the propagation characteristics to determine the location and characteristics of the source, or the data and source information are used to infer the characteristics of the propagation medium. In this case, the microbarom source location is either inferred from the model in Chapter 2, or known from arrays observing the storm from directions away from the storm winds. We aim to use the characteristics of the received signal and the propagation model presented here to infer some measure of the propagation medium.

Two-Dimensional Propagation

One can estimate the refraction of the microbarom signal propagating into the strong storm winds near the eye by neglecting vertical variations in the atmosphere and modeling the propagation in a horizontal plane at the top of the boundary layer. The source functions in the geometric equations for this simplified propagation scheme are,

$$c\left(\vec{x}\right) = c_0, \qquad \vec{v}_0\left(\vec{x}\right) = \begin{pmatrix} -v_\phi\left(r\right)\sin\phi + v_r\left(r\right)\cos\phi - v_{\text{bg}}\cos\theta_{\text{bg}} \\ v_\phi\left(r\right)\cos\phi + v_r\left(r\right)\sin\phi + v_{\text{bg}}\sin\theta_{\text{bg}} \\ 0 \end{pmatrix}, \tag{95}$$

where $r = \sqrt{x^2 + y^2}$ and $\phi = \tan^{-1}\left(\frac{y}{x}\right)$ are radial distance from the storm eye and azimuth around the storm in polar coordinates, respectively. The velocities $v_\phi\left(r\right)$ and $v_r\left(r\right)$ are the cyclonic and radial wind components given in Eq. (68) and (73), and v_{bg} and θ_{bg} are the magnitude and direction of the background wind associated with the background swell. Because propagation is assumed to be contained within the horizontal plane, all ray paths must have initial inclination angles of $\theta = 0$.

An example ray field for propagation through a Category 3 storm is shown in Fig. 8 as an overlay on the combined wind field of the storm and background. The source location has been inferred by locating the region in which $|\vec{v}_{\text{storm}} - \vec{v}_{\text{BG}}| \sim 0$, which is in agreement with the predicted source location from Chapter 2. Included in the figure are ray paths with ϕ between 15^o and 165^o

where $\phi = 90^o$ corresponds to north (into the storm eye). The ray paths in the figure were truncated at a radius of 2000 kilometers from the storm center. Note that the refraction along paths away from the strong storm winds is negligible. For ray paths near 15^o or 165^o, the propagation is nearly along straight lines radiating away from the source region. The ray paths which propagate into the strong winds around the eye are refracted strongly around the storm resulting in a region directly north of the storm where little acoustic energy is present due to strong geometric attenuation. To the north west of the storm eye there are multiple propagation paths of interest. There are some propagation paths which pass to the west of the strong winds in the eye and arrive at the 2000 kilometer radius with weak refraction. These arrivals have back azimuths directed towards the actual source region. Several additional arrivals are present in this north-western region which have been strongly refracted. The signal detected due to these propagation paths is expected to have back azimuths directed back towards the eye of the storm, which produces a false source associated with the region around the eye of the storm. In the following discussion, these strongly refracted arrivals are referred to as anomalous arrivals from the direction of the storm eye.

Using the direction of $\hat{\nu}$ at the outer radius where rays are ended, the back azimuth for signals at locations around the storm can be computed. The back azimuth relative to the direction to the storm eye is plotted in Figure 9 with the Category 3 storm in the previous figure corresponding to the blue line. The horizontal axis in the figure corresponds to the an azimuthal location around the storm with 90^o being north. The vertical axis shows the difference between the back azimuth

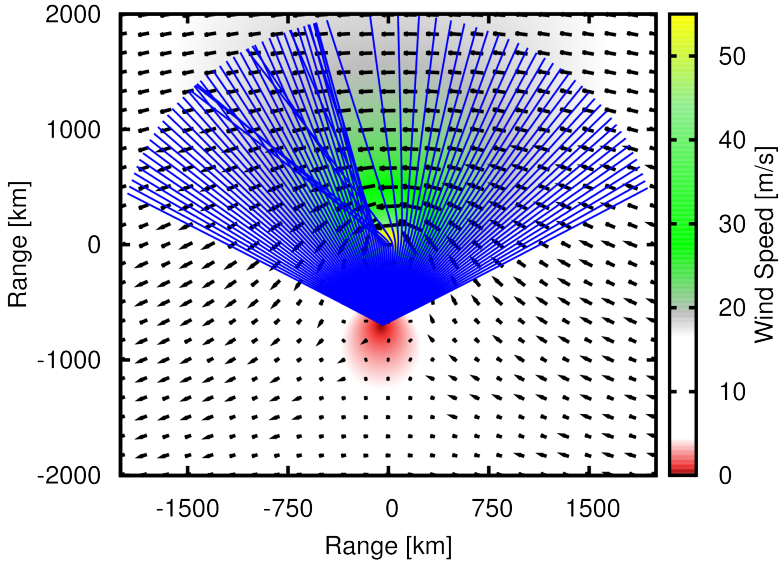

Fig. 8: Planar propagation paths through the boundary layer of a maritime storm and the wind field in the boundary layer.

detected at that location around the storm and the direction to the eye of the storm. As mentioned previously, the azimuths away from the strong winds are weakly refracted resulting in the positive and negative deviations in the figure for $\phi > 120^o$ and $\phi < 60^o$ respectively.

The other lines in the figure represent the arrival characteristics for propagation through stronger and weaker storm winds. For increased or decreased maximum wind speed, the source location changes to a new location where $|\vec{v}_{\text{storm}} - \vec{v}_{\text{BG}}| \sim 0$ produces counter propagating waves of equal period. Additionally, the refraction effects for propagation through the storm vary with storm intensity. The moving source region produces the variations in the positive and negative deviations for $\phi > 120^o$ and $\phi < 60^o$ respectively, while the wind speed variations produce a noticeable change in the propagation effects of the anomalous arrivals from the storm eye. For increased storm intensity, the refraction effect is intensified and the extent around the storm to which the anomalous arrivals are present increases. For a weaker, Category 1 storm, the anomalous arrivals extend only 35^o counterclockwise from north of the storm. Alternately, in a more intense Category 5 storm these anomalous arrivals extend over 70^o from north of the storm.

A clear physical explanation for this strong refraction can be elucidated by examining the propagation effects in Fig. 7. The strong cyclonic winds produce displacement of acoustic energy

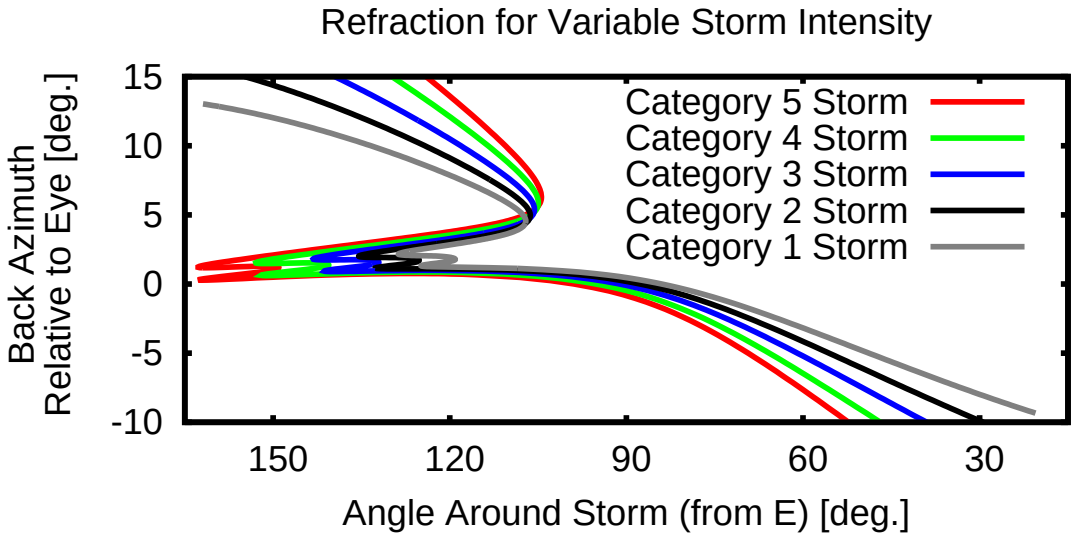

Fig. 9: The refraction of the sound produces detectable acoustic signal north west of the storm which seems to emanate from the eye itself. The extent around the storm that this anomalous signal is present is strongly dependent on the storm intensity.

as it propagates through the storm as in the left side of Fig. 7. Additionally, regions in which the wind varies rapidly produce refraction effects as in the right side of Fig. 7. The region near the eye in Fig. 8 has been enlarged and is shown in the left panel of Fig. 10. The gray ring in the figure shows the radius of maximum winds at 50 kilometers. It is immediately evident from this enlarged region that the anomalous arrivals from the storm eye are the result of strong refraction effects in the eye wall of the storm. These refraction effects in the eye wall are due to the rapid increase in the cyclonic wind speed. The right panel of Fig. 10 shows the cyclonic wind profile as a function of radius from the eye. Included in the figure are numerical values for the gradients in the eye wall region and at radii larger than the radius of maximum wind. For comparison, the upward refracting thermodynamic sound speed gradient in the troposphere due to the adiabatic lapse rate of $9.8\frac{\mathrm{K}}{\mathrm{km}}$ is 0.0058 s^{-1}.

The wind in the eye wall increases rapidly with radius producing a positive gradient which results in refraction of signal propagating in the $\hat{\phi}$ direction into the $-\hat{r}$ direction. This causes the rays to bend counterclockwise as they pass near the storm eye in the direction of the cyclonic winds. Thus, the reason that the anomalous arrivals from the eye extend further around the storm for stronger winds is due to the increasingly strong cyclonic wind gradient in the eye wall. Away from the eye column, the interaction of the wind and microbarom signal is dominated by

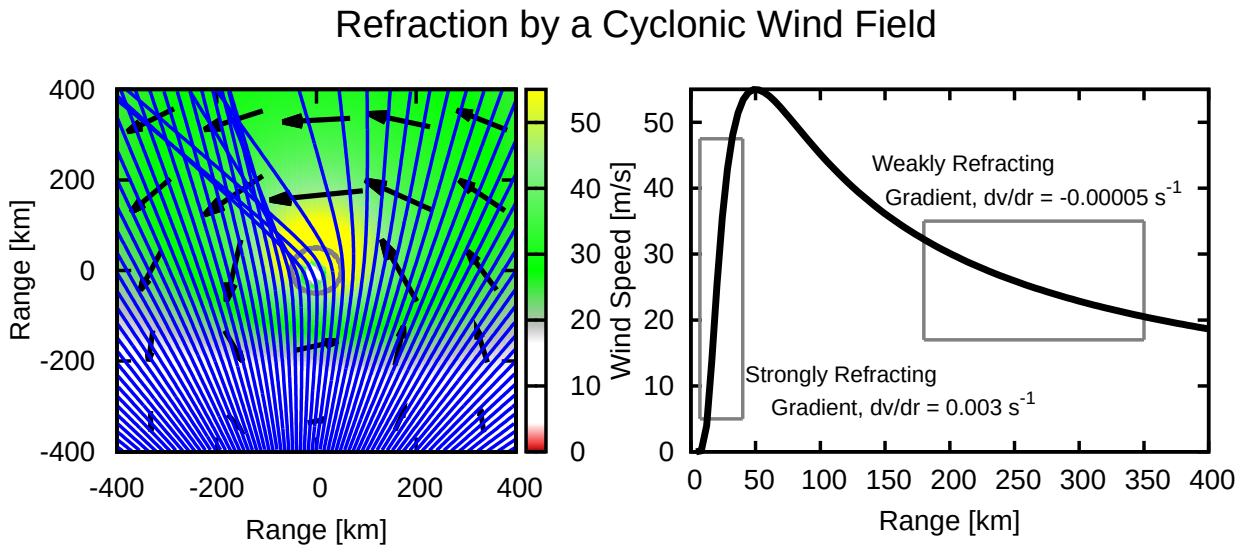

Fig. 10: A closer view of the refraction which occurs near the eye wall of the storm (left). The radial profile of the cyclonic component of the storm wind (right).

the displacement effect in the left panel of Fig. 10. The gradient in this region is two orders of magnitude smaller than the gradient in the eye wall where the wind increases from zero in the eye column to a maximum at the radius of maximum winds. Additionally, the direction of the refraction outside of the radius of maximum winds is away from the storm, in the $+\hat{r}$ direction since the wind is decreasing with range in this region.

To summarize, in the limit of propagation in a two dimensional plane at the top of the boundary layer of a large maritime storm, the refraction of infrasonic signal is produced by a refraction of the $\hat{\phi}$ component of $\vec{\nu}$ toward $-\hat{r}$ as a ray passes through the eye wall due to the large positive value of $\frac{\partial v_\phi}{\partial r}$ in this region. This produces an extended region north west of the storm characterized by anomalous microbarom signals which seem to emanate from the storm eye. The extent of this region around the storm is dependent on the strength of the refraction in the eye wall and therefore on the gradient of the cyclonic winds in this region between the eye column and the radius of maximum winds. A more intense storm generates a larger the wind gradient in the eye wall, resulting in increased refraction and an enlargement of the region containing anomalous arrivals.

Three-Dimensional Propagation

In the previous section, it was assumed that the microbarom signal would undergo refraction as it propagated through the entire boundary layer wind field of a large maritime storm. In actuality, the strong winds in the boundary layer form an acoustic duct which traps some of the microbarom energy beneath the storm where it will propagate and interact with the strong horizontal wind gradients. However, the two dimensional model neglected the directionality of this duct and various other complications associated with propagation in a vertically varying medium. In order to model propagation in three dimensions, the wind profiles in Eq. (68) and (73) must be modified to include the vertical variations between the ocean surface and the top of the storm at the tropopause. To accomplish this, we have elected to modify the wind models used previously by varying the coefficient, $v_{\max}$, with altitude. This produces wind models which are separable in r and z,

$$v_\phi(r,z) = v_{\max}(z)\sqrt{\left(\frac{r_m}{r}\right)^B e^{1-\left(\frac{r_m}{r}\right)^B}}, \qquad v_r(r,z) = -3.5v_\phi^2(r,z). \tag{96}$$

In the lowest few kilometers of the atmosphere, winds increase from zero at the ocean surface

to a maximum at the top of the layer, which we assume to be approximately two kilometers for this idealized model. Several studies have demonstrated that, for flow over the open ocean, the wind in the boundary layer increases logarithmically above the stagnation height, z_0,

$$v_{\mathrm{BL}}(z) = \begin{cases} 0 & z < z_0 \\ v_0 \left[\ln\left(\frac{z}{z_0}\right) + \psi(z, z_0, L) \right] & z > z_0 \end{cases}, \tag{97}$$

where v_0 is some overall scaling to produce the physical wind speed, L is the Monin-Obukov stability parameter, and ψ is a correction term [50, 51]. As in Reference [49], a modification is made to shift the z axis by z_0 which removes the non-smooth transition at $z = z_0$ by shifting it to $z = 0$ while maintaining the condition that $v_{\mathrm{BL}}(0) = 0$. The correction term is assumed to be linear, resulting in a boundary layer wind profile described by,

$$v_{\mathrm{BL}}(z) = v_0 \left[\ln\left(1 + \frac{z}{z_0}\right) - \beta z \right]. \tag{98}$$

Direct measurements of the vertical structure in the boundary layer of a large maritime storm are nearly nonexistent. One of the limited sources of measurements of the boundary layer of a storm is the Coupled Boundary Layers Air-Sea Transfer (CBLAST) experiment in 2003 which made measurements of the vertical structure of turbulence in the boundary layer between rain bands [52]. GPS dropsondes where launched from NOAA WP-3D Orion aircraft flying above the boundary layer regions between rain bands of Hurricanes Fabian and Isabel in early September of 2003. The wind speed data obtained from CBLAST in these experiments are shown in the left panel of Fig. 11. Other atmospheric data sources can provide some estimate of the wind structure in the lower troposphere. The center panel in Fig. 11 shows wind profiles during Hurricane Igor in 2010 from WRF [53]. The right panel in the figure contains the wind profiles from the same storm from the Ground-2-Space database [54]. In all of these data sources, the measurements extend to some minimum altitude tens of meters above the ocean surface and the winds are not assumed to go to zero at the ground surface, which is required in our model.

The wind profiles shown in Fig. 11, can be used to determine the range of possible surface roughnesses, z_0, and linear coefficients, β, in Eq. (98) which produce accurate profiles for the winds in the boundary layer. One finds that the surface roughness is typically of order 20 to 50 meters

with extrema from 1 to over 100 meters. The linear coefficient, β, ranges from 0.3 to 0.7 km^{-1}. The range of possible surface roughnesses is within the range of surface wave heights expected for the sub-hurricane force winds which would be present in the outer bands of the storm [37]. In the following examples and discussion, a surface roughness of 35 meters and linear coefficient $\beta = 0.4$ km^{-1} have been used to model the propagation in the duct under the storm. The physical wind speed, v_0, is determined by the maximum wind speed for a given storm intensity.

The vertically varying storm model needs to be combined with a background atmosphere model to produce a full propagation medium. The polynomial fit for atmospheric temperature developed by Lingevitch et al. can be used to calculate the ambient thermodynamic sound speed [56]. Additionally, a Gaussian wind jet with magnitude 60 meters per second, centered at 60 kilometers altitude, and directed towards the west can be used to produce a stratospheric duct for propagation downwind of the duct. Such an atmospheric state is typical of late summer and early autumn in the northern hemisphere [37]. The temperature and wind in this stratified background model are shown in the left panels of Fig. 12. The right panel of the figure shows some of the propagation paths in such an atmosphere. In the case of propagation towards the west, the stratospheric jet provides additional downward refraction and the shallower ray paths are ducted back towards the ground in the stratosphere. For energy propagating towards the east, there is no ducting in the stratosphere and all of the energy propagates into the thermosphere before being refracted by the large temperature gradient there. Thus, microbaroms which do not interact strongly with the storm winds will propagate into the upper atmosphere and be refracted back towards the ocean surface from the stratosphere or thermosphere depending on the propagation

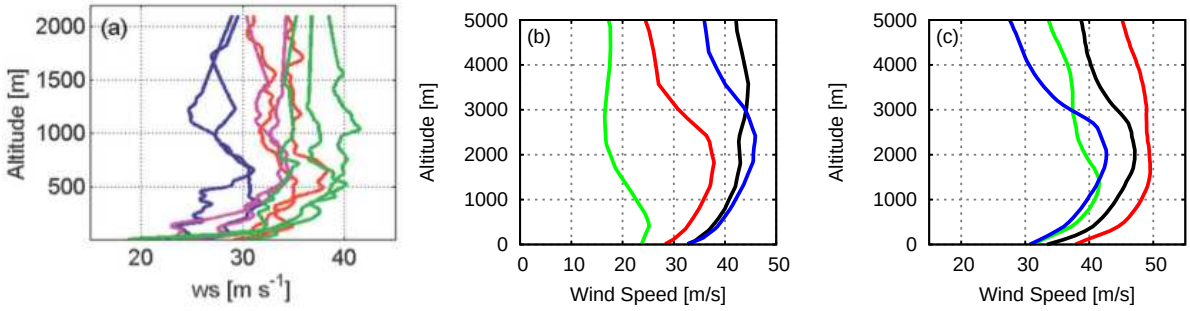

Fig. 11: (a) Wind speed profiles obtained during the CBLAST experiment in September of 2003, as reported in Ref. [55]. (b) Wind speed profiles obtained from WRF data during Hurricane Igor in 2010. (c) Wind speed profiles obtained from G2S data during Hurricane Igor in 2010. Note the differences in vertical range.

direction.

The winds in the boundary layer have been used to determine a source region for the microbaroms generated by the storm as in Chapter 2. Ray paths have been generated with initial inclinations of $5^o \leq \theta \leq 20^o$ and initial azimuths $60^o \leq \phi \leq 100^o$, where $\phi = 90^o$ is north. The propagation medium consists of the vertically dependent storm wind field described in Eq. (68), (73), and (98) for storms of varying intensity and the background temperature and wind shown in Fig. 12. The refraction effects observed are similar between storms of different intensity as one would expect, therefore only the results for a Category 3 storm will be discussed in detail. In order to analyze the back azimuth of signal arriving in the far field, only the geometric ray paths are necessary. However, the transmission loss due to the geometric spreading can be calculated to determine whether the refracted signal will contain sufficient energy to contribute to the measured acoustic energy far from the storm. The extension of geometric acoustics necessary to calculate the geometric spreading factor in a range dependent medium is presented in Appendix A.

Consider propagating a bundle of rays with identical azimuth and varying inclination angles. In this analysis, a bundle defined by $\phi = 84^o$ and $12.5^o \leq \theta \leq 13.5^o$ has been generated and used to elucidate the ducting and refraction effects. An overhead view of this ray bundle is shown on the left side of Fig. 13 along with an overlay showing the storm winds magnitude at the top of the boundary layer. Several of the ray paths are horizontally refracted by the storm winds near the eye as in the 2D propagation model. The resulting anomalous arrivals due to this refraction

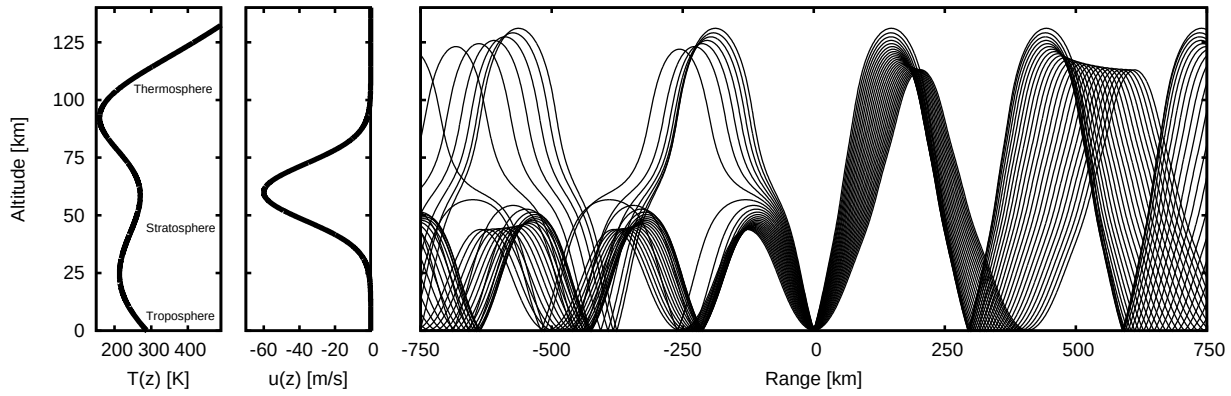

Fig. 12: Temperature, wind, and propagation paths in a model atmosphere used as a background for the storm winds in three dimensions.

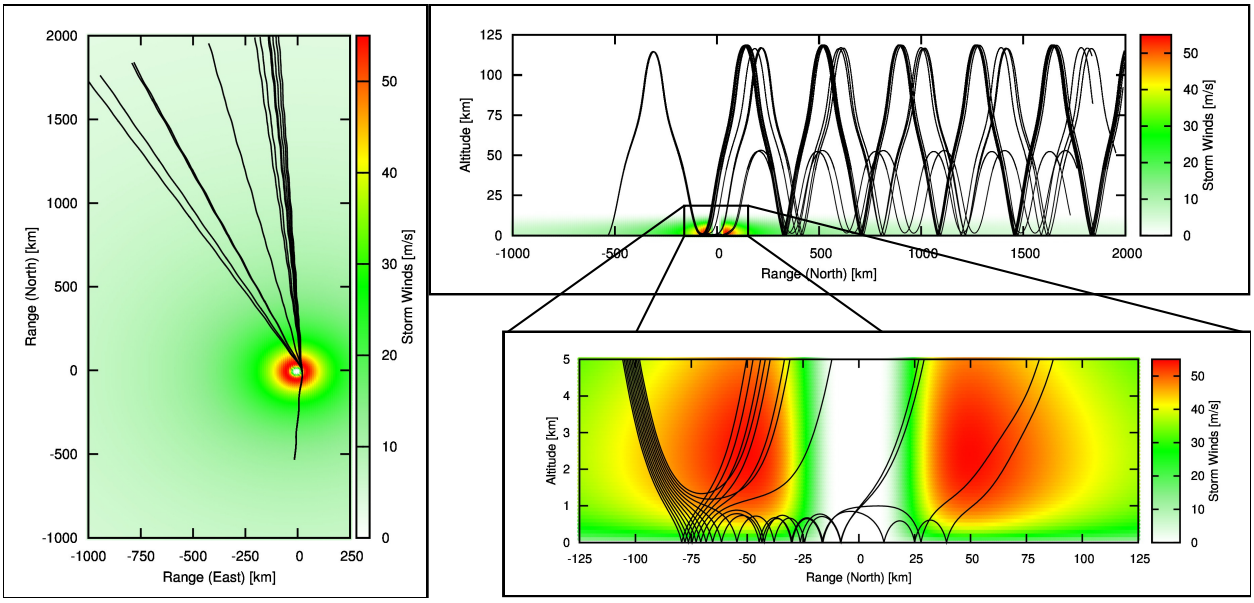

Fig. 13: Multiple views of the ray bundle with fixed azimuth, $\phi = 84^o$, and varying inclination angle $\theta = 12.5^o$ to 13.5^o.

extend $\sim 30^o$ counter-clockwise around the storm at a range of 2,000 kilometers. This is less than the $\sim 40^o$ predicted for a Category 3 storm using the two dimensional model. The decrease in refraction is due to the decreased interaction with the horizontal gradients.

Ray are ducted in the boundary layer under the condition that they are propagating parallel to the winds. Therefore, only the rays aligned with the cyclonic wind component will be refracted by the radial gradient. In the case that the ray paths are only weakly refracted, the cyclonic winds turn westward on the north side of the storm while the ray paths continue to propagate towards the north. This results in the ray paths escaping from the duct and weaker overall refraction compared to the two dimensional model. In the case that the horiztonal refraction is stronger, the rays continue propagating parallel to the winds and the horizontal refraction is close to that of the two dimensional model. Thus, a stronger storm is likely to produce refraction nearer to that predicted by the 2D model in which the ray interacts with the boundary layer winds along their entire propagation paths. Similarly, for storm winds weaker than some threshold, the winds in the boundary layer may not be able to duct the microbaroms at all.

In addition to the overhead view of the propagation paths shown in the left side of Fig. 13, it is useful to examine the vertical refraction producing ducting in the boundary layer. The right panels in the figure show the same bundle of ray paths as viewed from the west. The color scaling

in these panels is the wind along the $y = 0$ plane. The lower panel of the figure is a magnified view of the region around the storm eye column near the ocean surface. Within this region, the rays returning to the ocean surface with steeper angles pass through the boundary layer and are reflected off the ocean surface, passing through the boundary layer a second time and escaping from the storm winds. The rays which return towards the ocean surface with shallower angles are refracted back upward before reaching the ocean surface due to the wind gradient above the boundary layer.

For a small number of ray paths, the horizontal changes in the winds are such that the rays penetrate through the boundary layer and are reflected off the ocean surface. The rays are then unable to escape back through the downward refracting wind gradient. These ray paths are ducted through the boundary layer and refracted by the horizontal wind gradients in the eye wall of the storm. Analyzing other initial azimuth angles, one finds that the results from the analysis of the two dimensional propagation are still valid for propagation in three dimensions. The rays which are ducted through the radially increasing winds in the eye wall are horizontally refracted as in the two dimensional model.

The leading order amplitude can be computed by solving the transport equation as discussed in Appendix A. One can then determine the amplitude of the anomalous arrivals relative to those which are not ducted in the boundary layer of the storm. The intercepts and amplitudes for rays strongly refracted by the cyclonic storm winds are shown in the left panel of Fig. 14. The cluster of points near the origin show the reflection points in the duct under the eyewall. After being ducted and horizontally refracted by the storm winds, the rays propagate either through the stratospheric or thermospheric duct shown in Fig. 12. In the case shown in Fig. 13, some of the rays are refracted sufficiently strongly around the storm that they are ducted by the stratospheric jet.

The anomalous arrivals produced by the horizontal refraction in the boundary layer arrive some distance form the storm forming ensonified bands which overlap with the ensonified regions produced by the microbaroms which are not ducted by the storm. The right panel of Fig. 14 shows this multiple propagation path geometry. The resulting signal at the receiver contains two coherent signals with slightly different back azimuths. From the analysis here, the separation of these azimuths can be determined to range from 10^o to over 25^o depending on the relative locations of the storm, source, and receiver.

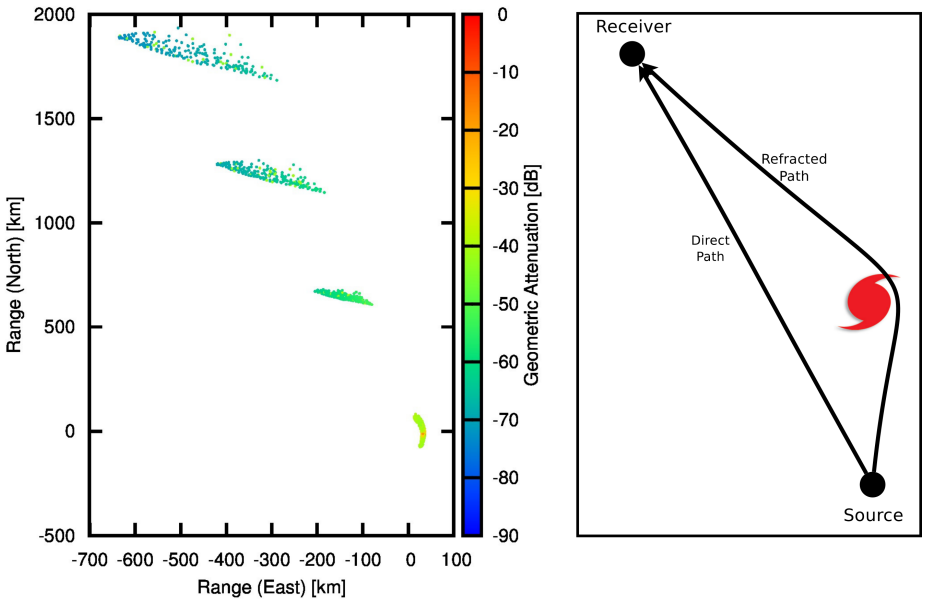

Fig. 14: (Left) Geometric attenuation for the contribution to the signal of the refracted arrival. (Right) The geometry of the multi-pathing due to the horizontal refraction.

The direct contribution to the signal will be ducted either by the winds in the stratosphere or the increasing temperature in the thermosphere. The attenuation of the arrivals due to the storm, stratospheric ducting, and thermospheric ducting are shown in Fig. 15. In the figure, the horizontally refracted arrivals due to the storm are shown in black. The stratospheric and thermospheric arrivals are shown in red and blue respectively. Additionally, the solid and dashed lines in the figure correspond to the attenuation expected for spherical and cylindrical spreading respectively. In each of the arrival clusters from the storm, the amplitude of the refracted arrivals is ~ 10 dB stronger than those of the stratospheric or thermospheric paths.

There is an important caveat to note regarding this result. The attenuation shown here is purely geometric, it does not include the effects of atmospheric absorption which can produce significant additional energy loss, particularly for propagation in the thermosphere. The additional attenuation due to atmospheric absorption could apply to only the horizontally refracted arrivals, only the direct arrivals, or both. In the case that the refracted energy is ducted in the stratosphere after it escapes the storm and the direct propagation is not, the amplitude difference could increase considerably. It is unlikely that the direct contribution would be ducted in the stratosphere and the horizontally refracted contribution would not due to the dominantly east-west orientation of the stratospheric jet. However, in such a case the two arrivals would likely be nearer to equal in

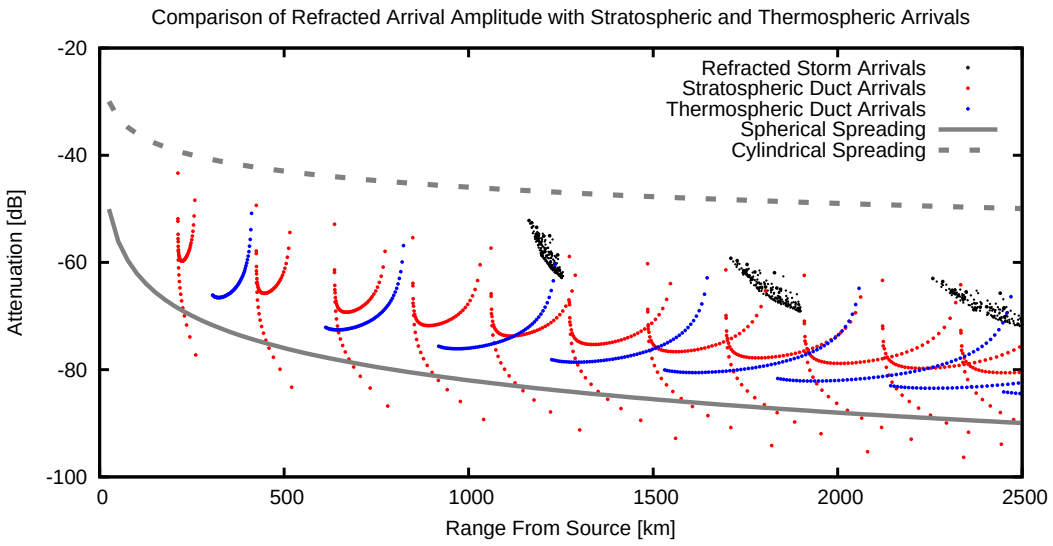

Fig. 15: The amplitude of the arrivals which have been strongly refracted (black points) are found to have undergone transmission loss due to geometric spreading approximately 10 dB less severe than that propagating directly to the far side of the storm via a stratospheric duct (red points) or thermospheric duct (blue points). Additional attenuation due to atmospheric absorption would likely increase this difference due to the refracted energy propagating less in the thermosphere.

amplitude. Finally, if neither or both of the propagation modes are ducted in the stratosphere, the similar additional attenuation will produce a pair of arrivals which are approximately 10 dB different in strength but have overall larger or smaller amplitude relative to the ambient noise levels at the receiver.

To summarize, it has been shown that the large positive gradient in the cyclonic component of the winds of a large maritime storm produces a strong refraction in the $-\hat{r}$ direction for infrasonic energy propagating through the boundary layer of the storm in the direction of the cyclonic winds. This refraction is present in both two and three dimensional propagation models, however, the directionality of the duct is only accounted for using the vertically varying storm. The refracted signal produces ensonified regions away from the storm which containing an anomalous contribution with back azimuth directed towards the storm center. In both two and three dimensional propagation models, the storm intensity affects the extent to which this anomalous signal is present around the storm.

It is expected that observations of the microbarom signal far from the storm center could contain multiple contributions: one corresponding to the energy which interacted weakly with the

storm and propagated directly to the receiver and a second corresponding to a strongly refracted ray path which has been ducted through the storm boundary layer near the eye column. Geometric propagation modeling predicts a difference in back azimuth between the two signals of 10^o - 25^o and a difference in amplitude of $\sim$ 10 dB. In Chapter 5, these values will be used to evaluate the performance of an idealized array design for continued study of microbaroms generated by large maritime storms.

CHAPTER 4

MONITORING THE 2010 AND 2011 ATLANTIC HURRICANE SEASONS

Microbaroms generated by maritime storms in the Atlantic can be detected in North America, Europe, and Africa depending on the atmospheric winds. In order to test the results obtained in Chapter 3, a number of infrasound arrays were deployed along the southern Atlantic coast of the United States during the 2010 and 2011 Atlantic hurricane seasons. Each array consisted of four infrasound recording elements. The elements each contained an infrasonic microphone with flat response from 0.02 Hz to 200 Hz, a data acquisition system sampling data at 33 samples-per-second, a GPS antenna, a 12 V battery, and a solar panel to maintain power. The sensor and data storage system is a single unit designed by the infrasound group at the NCPA specifically for rapid, temporary deployments.

The 2010 Atlantic Hurricane Season Deployment

During the 2010 Atlantic hurricane season, arrays were deployed in Florida and the Carolinas. The geometry of each array was an equilateral triangle of three elements with a fourth element at the center of the triangle. Each array of was deployed to obtain an aperture of approximately 1 to 1.5 kilometers. Detailed descriptions of the arrays is given in Appendix C along with expected array response functions. The array in Croatan National Forest near the Atlantic coast of North Carolina is shown in the left panel of Fig 16. The aperture of each triangular array was approximately one kilometer. The locations used for the deployments are shown in Fig. 17 and included the Ocala National Forest in central Florida, Francis Marion National Forest in South Carolina, Croatan National Forest in North Carolina, and private land owned by the McCoy family near

Fig. 16: The geometry of the Croatan array (left) and Brookhaven National Lab array (right)

Maxton, North Carolina.

During the 2010 Atlantic hurricane season, 12 storms reached at least Category 1 intensity. A full list of these storms and their trajectories are shown in Fig. 18. The arrays were not fully deployed and active until early September, and so storms early in the season (Danielle and Earl) were not recorded. Hurricanes Karl, Paula, and Richard formed in the Gulf of Mexico and didn't travel into the Atlantic. Hurricane Igor formed off the coast of Africa and moved eastward before turning north and strengthened to a Category 4 storm. Igor weakened to a Category 1 storm before striking Bermuda and continuing through the open Atlantic. The strong microbarom signals from hurricane Igor were chosen to use as sample data during development of array processing methods for detecting and monitoring microbaroms generated by large maritime storms. The remaining storms which formed late in the season either did not move through the open Atlantic or were not measured due to decreased solar exposure and loss of power on the equipment. Hurricane Otto formed north of the Dominican Republic and moved north west from there during early October of 2010. Hurricane Tomas formed north of Venezuela, moved into the Caribbean Sea, and turned north passing between Cuba and the Dominican Republic before weakening to a tropical storm.

The 2011 Atlantic Hurricane Season Deployment

The array locations from the 2010 experiment were re-populated for the 2011 Atlantic Hurricane seasons and three additional sites were added along the northern Atlantic coast. The additional sites included Bass River State Forest on the coast of New Jersey, Pachaug State Forest near the Rhode Island-Connecticut state line, and Brookhaven National Laboratory in New York.

Fig. 17: Locations of arrays deployed during the 2010 Atlantic Hurricane season (red markers) and sites added during the 2011 season (yellow markers).

These new sites are denoted with red markers in Fig. 17. The arrays in Bass River and Pachaug forests each contained 4 elements in a centered triangular array identical to those in Florida and the Carolinas. The Brookhaven National Laboratory array is semi-permanent and contains 6 elements in an approximately 3×2 grid.

The arrays were populated and began recording data in mid-July of 2011, allowing all the major storms of the 2011 season to be recorded. Five major storms were recorded during the 2011 Atlantic Season. Hurricane Irene produced usable data before making land fall in North Carolina near the Croatan Array. Hurricane Katia reached a maximum intensity of Category 4 and passed to the west of Bermuda. This maximum intensity and storm path are similar to those of Hurricane Igor in 2010 and provide a useful measure of whether such storms produce similar microbarom signals. Hurricane Maria was a very weak storm which produced some signal, Hurricanes Ophelia and Philippe passed through the open Atlantic during early October of 2011 and produced measurable microbarom signal. Detailed analysis and discussion of these storms along with results for Hurricane Igor will be presented in Chapter 6.

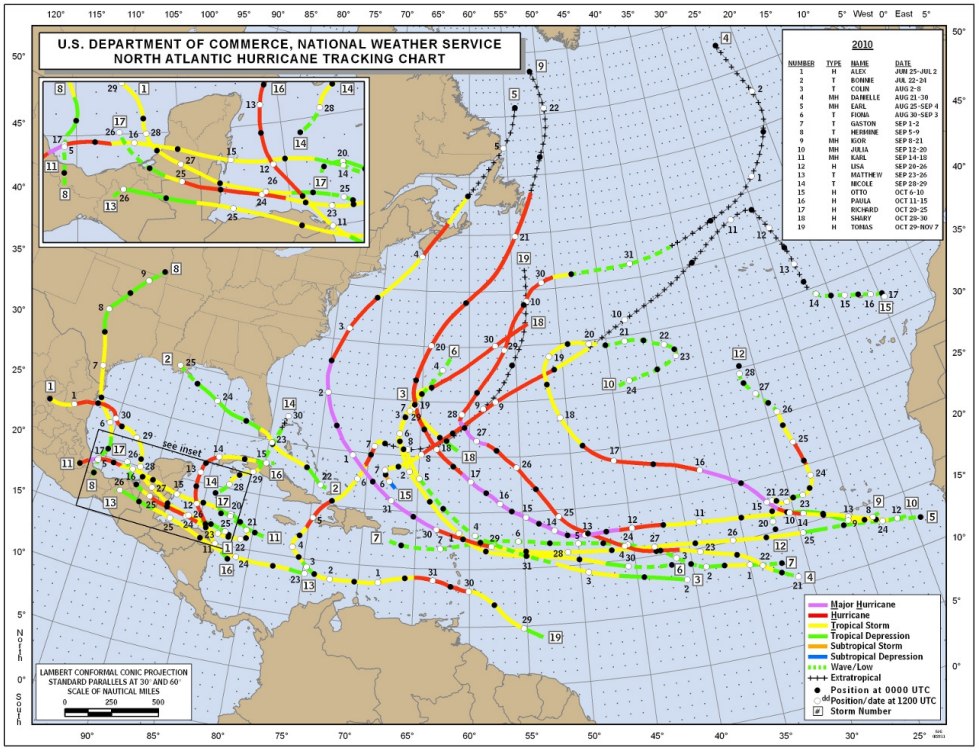

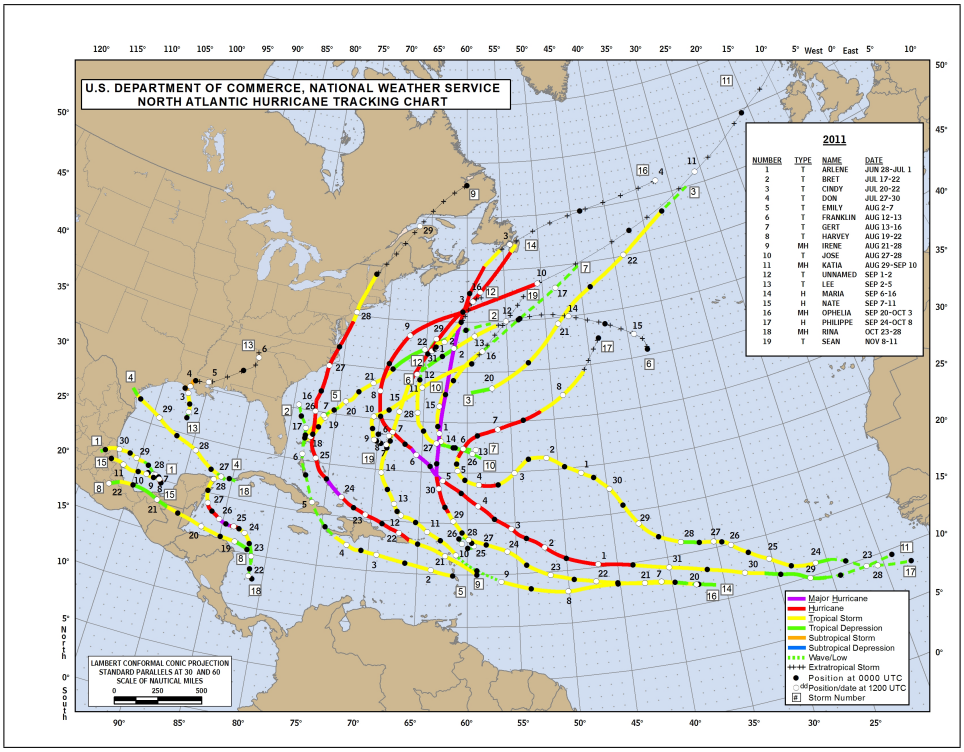

Fig. 18: Summaries of all storms during the 2010 (top) and 2011 (bottom) Atlantic Hurricane Seasons. From the 2010 season, data was recorded and analyzed from Hurricane Igor. The majority of other storms which remained in the open Atlantic occurred before the equipment was deployed. From the 2011 season, Irene, Katia, Maria, and Ophelia produced microbaroms which has been analyzed.

CHAPTER 5

ARRAY PROCESSING METHODS

In this section, mathematical methods for analyzing data recorded on an array of sensors are developed and discussed. Statistical properties of the data can be used to characterize the data and estimate the coherence, signal power, and back azimuth of the acoustic disturbance recorded on the array of sensors. The methods developed here are applicable to all types of data analysis involving periodic signals.

In the following analysis, the array geometry is contained in a composite location matrix $\boldsymbol{Z}$ whose rows are given by $\vec{z}_j = (x_j, y_j)$ which is the location of the j^{th} sensor, p denotes the number of sensors in the array, and q denotes the number of coherent signals present in the data record. A time record of data across an array is denoted by a vector $\vec{x}\,(t)$ and the Fourier transform of these time series form the vector $\vec{X}\,(f)$. Measured quantities are denoted by tildes, $\tilde{\vec{X}}\,(f)$, estimated quantities are denoted with hats, $\hat{\vec{X}}\,(f)$, and averaged quantities are denoted with brackets, $\left\langle \vec{X}\,(f) \right\rangle$. If multiple frequencies are being used in a calculation, the band is bounded by f_1 and f_K, and we assume K discrete frequency bins in the band. Additionally, a weighting function $\varrho\,(f)$ can be used to weight quantities calculated at various frequencies (in practice this function produces a K length vector of weights at the bins in the frequency band).

Background: Statistical and Fourier Methods

Consider an ensemble of recordings from an array of microphones. Each element $x_i\,(t)$ corresponds to the data recorded on a single sensor. From this vector of records, several statistical

properties can be calculated immediately [57].

$$\mu_i = \lim_{T\to\infty} \frac{1}{T} \int_0^T x_i\,(t)dt \quad \text{Mean Value,} \tag{99a}$$

$$\psi_i = \lim_{T\to\infty} \frac{1}{T} \int_0^T {x_i}^2\,(t)dt \quad \text{Mean Square Value,} \tag{99b}$$

$$R_{i,i}\,(\tau) = \lim_{T\to\infty} \frac{1}{T} \int_0^T x_i\,(t)\,x_i\,(t+\tau)dt \quad \text{Autocorrelation Functions,} \tag{99c}$$

$$R_{i,j}\,(\tau) = \lim_{T\to\infty} \frac{1}{T} \int_0^T x_i\,(t)\,x_j\,(t+\tau)dt \quad \text{Cross-correlation Functions,} \tag{99d}$$

where T is the time length of each recording. Note that μ_i and ψ_i form vectors of length p while the auto and cross correlation functions form a $p\times p$ matrix $\boldsymbol{R}\,(\tau)$ which is simply termed the correlation matrix [57, 58]. In practice one will never obtain an infinitely long time sample and instead one assumes $T \gg \tau_{\text{phen.}}$ where $\tau_{\text{phen}} = \frac{1}{f_{\text{phen.}}}$ is the period associated with the lowest frequency present in the phenomenon.

Consider if instead of the above definitions, one used averages across an infinite number of elements in an array to determine mean values at specific times,

$$\mu_i\,(t_n) = \lim_{p\to\infty} \frac{1}{p} \sum_{i=1}^{p} x_i\,(t_n) \quad \text{Mean Value,} \tag{100a}$$

$$\psi_i\,(t_n) = \lim_{p\to\infty} \frac{1}{p} \sum_{i=1}^{p} {x_i}^2\,(t_n) \quad \text{Mean Square Value,} \tag{100b}$$

$$R_{i,i}\,(t_n,\tau) = \lim_{p\to\infty} \frac{1}{p} \sum_{i=1}^{p} x_i\,(t_n)\,x_i\,(t_n+\tau) \quad \text{Autocorrelation Functions,} \tag{100c}$$

$$R_{i,j}\,(t_n,\tau) = \lim_{p\to\infty} \frac{1}{p} \sum_{i=1}^{p} x_i\,(t_n)\,x_j\,(t_n+\tau) \quad \text{Cross-correlation Functions.} \tag{100d}$$

If the properties computed from the time averages over individual records of the ensemble are the same from one record to the next and equal the corresponding properties from an ensemble average over the records at any time t_n, then

$$\lim_{T\to\infty} \frac{1}{T} \int_0^T \left| R_{i,i}\,(\tau) - {\mu_i}^2 \right| d\tau = 0, \tag{101}$$

and the data is termed "stationary". This condition is termed the ergodic theorem [57]. In the

case of acoustic data, these statistical quantities have physical meaning which is important to note. The elements of $\vec{\mu}$ give the ambient pressure about which the acoustic perturbations occur. For analysis, the mean value is subtracted off the records. The elements in $\vec{\psi}$ are proportional to the acoustic energy of the disturbance per unit time. The elements in $\boldsymbol{R}(\tau)$ exhibit peaks at specific times. The diagonal elements should exhibit peaks at $\tau = 0$ while the off-diagonal elements exhibit peaks at the travel times from one sensor to another in the case that coherent energy is present across the array.

The microbarom signal of interest to this investigation is a continuous signal which is detected on the array for long periods of time. In such a case, it is more beneficial to analyze the data in the frequency domain because statistical quantities can be estimated by averaging over multiple concurrent snapshots. The frequency content of each record can be computed via a Fourier transform [35],

$$X_i(f) = \frac{1}{\sqrt{2\pi}} \int_{-\infty}^{\infty} x_i(t)\, e^{2\pi i f t} dt \quad \Longleftrightarrow \quad x_i(t) = \frac{1}{\sqrt{2\pi}} \int_{-\infty}^{\infty} X_i(f)\, e^{-2\pi i f t} df. \tag{102}$$

The function $X_i(f)$ is a complex function, however, because $x(t)$ is pure-real, a number of useful properties are immediately found. Consider writing $X_i(f) = A_i(f) e^{i\varphi_i(f)}$, then one finds

$$A_i(-f) = A_i(f), \quad \varphi_i(-f) = -\varphi_i(f) \quad \Rightarrow \quad X_i(-f) = X_i^*(f).$$

Thus only the positive frequencies need be considered for analysis. Additionally, the results of time scaling and shifting can be inferred.

$$x(at) \Leftrightarrow \frac{1}{|a|} X\left(\frac{f}{a}\right) \quad \text{time scaling,} \tag{103a}$$

$$\frac{1}{|b|} x\left(\frac{t}{b}\right)) \Leftrightarrow X(bf) \quad \text{frequency scaling,} \tag{103b}$$

$$x(t - t_0) \Leftrightarrow X(f)\, e^{2\pi i f t_0} \quad \text{time shifting,} \tag{103c}$$

$$x(t) e^{-2\pi i f_0 t} \Leftrightarrow X(f - f_0) \quad \text{frequency shifting.} \tag{103d}$$

Using the time shifting result, one can derive an important result for the correlation functions above. Consider expressing the cross-correlation function in terms of the Fourier transforms

of the functions,

$$\begin{aligned}
R_{i,j}(\tau) &= \lim_{T\to\infty}\frac{1}{T}\int_0^T x_i(t)\,x_j(t+\tau)dt \\
&= \lim_{T\to\infty}\frac{1}{T}\int_0^T\left[\frac{1}{\sqrt{2\pi}}\int_{-\infty}^{\infty}X_i(f_1)\,e^{2\pi i f_1 t}df_1\right]\left[\frac{1}{\sqrt{2\pi}}\int_{-\infty}^{\infty}X_j(f_2)\,e^{2\pi i f_2(t+\tau)}df_2\right]dt \\
&= \lim_{T\to\infty}\frac{1}{T}\int_{-\infty}^{\infty}\int_{-\infty}^{\infty}X_i(f_1)\,X_j(f_2)\,e^{2\pi i f_2\tau}\frac{1}{2\pi}\int_0^T e^{2\pi i(f_1+f_2)t}df_1df_2dt \\
&= \int_{-\infty}^{\infty}\int_{-\infty}^{\infty}X_i(f_1)\,X_j(f_2)\,e^{2\pi i f_2\tau}\delta(f_1+f_2)df_1df_2 \\
&= \int_{-\infty}^{\infty}X_i(f_1)\,X_j(-f_1)\,e^{-2\pi i f_1\tau}df_1 = \int_{-\infty}^{\infty}S_{i,j}(f_1)\,e^{-2\pi i f_1\tau}df_1. \qquad (104)
\end{aligned}$$

In this result we've defined the cross-spectral density function, $S_{i,j}(f)$, which can be derived from the Fourier transform of the cross correlation function, $R_{i,j}(\tau)$. This relation is termed the Weiner-Khinchin theorem [57]. From this result, one can calculate the cross-spectral density function from the Fourier transformed data and use its Fourier transform to compute the cross correlation function. Introducing the finite Fourier transform, $X_k(f,T)$, the cross spectral density matrix is then defined by

$$S_{i,j}(f) = \lim_{T\to\infty}X_i(f,T)\,X_j^*(f,T), \qquad X_k(f,T) = \int_0^T x_k(t)e^{2\pi i f t}dt. \qquad (105)$$

The cross spectral density matrix, $\boldsymbol{S}(f)$, contains information about the relative phase of the signal across the entire array of sensors and is therefore very useful in approximating the direction of arrival.

In addition to direction of arrival estimates, the cross spectral density matrix elements can be used to construct the coherence matrix, $\boldsymbol{\gamma}^2(f)$,with elements given by [57],

$$\gamma_{i,j}^2(f) = \frac{|S_{i,j}(f)|^2}{S_{i,i}(f)\,S_{j,j}(f)}. \qquad (106)$$

It is straightforward to see that the diagonal elements of $\boldsymbol{\gamma}^2(f)$ are each unity. However, the off-diagonal elements contain information about the relative phasing of the signals between sensors i and j. When there exists some relative phasing between two data records, the cross spectral density function $S_{ij}(f)$ will be some non-zero value dependent on the strength of the signal. Alternately,

when there is no such relationship present, the random phase difference averaged over time results in $S_{ij}(f)$. Thus, the coherence function in Eq. (106) measures the relative phase between data recorded on sensors i and j, scaled to eliminate any bias due to the gain or background level of the sensors.

The multivariate coherence contained in an array's data record can be measured measure by the pure state filter developed by Samson and further studied by Olson [59, 60],

$$\gamma^2_{(\text{filter})}\left[\boldsymbol{S}(f)\right] = \frac{p\text{Tr}\left[\boldsymbol{S}^\dagger(f)\boldsymbol{S}(f)\right] - \text{Tr}\left[\boldsymbol{S}(f)\right]^2}{(p-1)\left(\text{Tr}\left[\boldsymbol{S}(f)\right]\right)^2}. \tag{107}$$

The benefit of this coherence measure is that it can be used as a data-adaptive band-pass filter. For broadband analysis, $\gamma^2_{(\text{filter})}(f)$ provides a measure of how coherent the data is across the array at one frequency versus another. This allows a heavier weight to be associated with frequencies which contain more coherent signal.

Some analysis of this filter should be performed before any applications can be considered. The form with which data is input to the filter function is critical for understanding the output. Consider the simple case of 2 elements. For the spectral density matrix, one has,

$$\boldsymbol{S}(f) = \begin{pmatrix} S_{11}(f) & S_{12}(f) \\ S_{21}(f) & S_{22}(f) \end{pmatrix},$$

where, by definition, $S^*_{12}(f) = S_{21}(f)$. The traces involved in the pure state filter are given by,

$$\text{Tr}\left[\boldsymbol{S}(f)\right] = S_{11}(f) + S_{22}(f),$$

$$\text{Tr}\left[\boldsymbol{S}^\dagger(f)\,\boldsymbol{S}(f)\right] = S^2_{11}(f) + S^2_{22}(f) + 2\left|S_{12}(f)\right|^2,$$

and the pure state filter returns,

$$\begin{aligned}\gamma^2_{(\text{filter})}\left[\boldsymbol{S}\left(f\right)\right] &= \frac{2\left(S^2_{11}\left(f\right)+S^2_{22}\left(f\right)+2\left|S_{12}\left(f\right)\right|^2\right)-\left(S_{11}\left(f\right)+S_{22}\left(f\right)\right)^2}{\left(S_{11}\left(f\right)+S_{22}\left(f\right)\right)^2}\\ &= \frac{S^2_{11}\left(f\right)+S^2_{22}\left(f\right)-2S_{11}S_{22}+4\left|S_{12}\left(f\right)\right|^2}{S^2_{11}\left(f\right)+S^2_{22}\left(f\right)+2S_{11}S_{22}}\\ &= \frac{\left(S_{11}\left(f\right)-S_{22}\left(f\right)\right)^2+4\left|S_{12}\left(f\right)\right|^2}{\left(S_{11}\left(f\right)+S_{22}\left(f\right)\right)^2},\end{aligned}$$

which doesn't provide much information directly. Consider alternately, if one divides the i,j element of the matrix by the combined diagonal magnitudes, $\sqrt{S_{ii}S_{jj}}$. The resulting matrix is the coherence matrix,

$$\boldsymbol{\gamma}\left(f\right)=\begin{pmatrix}1 & \frac{S_{12}}{\sqrt{S_{11}S_{22}}}\\ \frac{S_{21}}{\sqrt{S_{11}S_{22}}} & 1\end{pmatrix}=\begin{pmatrix}1 & \gamma_{12}(f)\\ \gamma_{21}(f) & 1\end{pmatrix}.$$

Immediately one can see that,

$$\text{Tr}\left[\boldsymbol{\gamma}\left(f\right)\right]=2,\qquad \text{Tr}\left[\boldsymbol{\gamma}^\dagger\left(f\right)\boldsymbol{\gamma}\left(f\right)\right]=2+2\left|\gamma_{12}\left(f\right)\right|^2,$$

which leads to,

$$\gamma^2_{(\text{filter})}\left[\boldsymbol{\gamma}\left(f\right)\right]=\frac{2\left(2+2\left|\gamma_{12}\left(f\right)\right|^2\right)-2^2}{2^2}=\left|\gamma_{12}(f)\right|^2.$$

Thus, once a matrix is modified by $A_{ij}\rightarrow\frac{A_{ij}}{\sqrt{A_{ii}A_{jj}}}$, non-zero off-diagonal elements increase the value of the pure state filter applied to the matrix towards unity and provide a measure of coherence across sensors in the case of the power spectral density matrix. It can be seen that in the case that $\boldsymbol{S}\left(f\right)$ is diagonal,$\gamma^2_{(\text{filter})}\left[\boldsymbol{S}_{\text{diag}}\right]=0$.

In practice, one is limited to a finite sample length as well as discrete sampling of the actual process. This requires the use of a discrete Fourier transform, or DFT,

$$X_k=dt\sum_{n=1}^{N}x_n e^{2\pi i\frac{kn}{N}}\quad\Leftrightarrow\quad x_n=df\sum_{K=1}^{N}X_k e^{-2\pi i\frac{kn}{N}},\tag{108}$$

where $Ndt=T$ and $df=\frac{1}{Ndt}=\frac{1}{T}$. The value of x_n corresponds to $x(n\,dt)$ while X_k corresponds

to $X\left(\frac{n}{Ndt}\right)$. From these definitions for the discrete Fourier transform and because x_n is pure-real, several characteristics of X_k are immediately known,

$$X_{-k} = X_k^* \text{ for all } k, \tag{109a}$$

$$X_{N-k} = X_k^* \text{ for } k = 1, 2, 3, \ldots, \frac{N}{2}, \tag{109b}$$

$$X_{k+N} = X_k \text{ for all } k, \tag{109c}$$

$$x_{n+N} = x_n \text{ for all } n. \tag{109d}$$

The operation of taking the DFT of a vector of values $\vec{x}$ can be written more compactly by

$$\vec{X} = \boldsymbol{W}\vec{x}, \qquad W_{ij} = e^{-2\pi i \frac{ij}{N}}, \tag{110}$$

and requires N^2 operations. However, an algorithm termed the fast Fourier transform, or FFT, can compute the transform of $\vec{x}$ in $N \ln_2 N$ operations [61]. The mathematical formulation of the FFT has been known since Gauss derived its basic algorithm in 1805. However, it was not until the 1960's that Cooley and Tukey published the algorithm [62]. Prior to this, Danielson and Lanczos demonstrated that a discrete transformation of length N can be rewritten as a sum of two discrete transformations of length $\frac{N}{2}$ [63]. The proof is straight forward,

$$\begin{aligned} X_k = \sum_n W_{k,n} x_n &= \sum_{n=0}^{N-1} e^{2\pi i \frac{nk}{N}} x_n \\ &= \sum_{n=0}^{\frac{N}{2}-1} e^{2\pi i \frac{2nk}{N}} x_{2n} + \sum_{n=0}^{\frac{N}{2}-1} e^{2\pi i \frac{(2n+1)k}{N}} x_{2n+1} \\ &= \sum_{n=0}^{\frac{N}{2}-1} e^{2\pi i \frac{nk}{\frac{N}{2}}} x_{2n} + e^{-2\pi i \frac{k}{N}} \sum_{n=0}^{\frac{N}{2}-1} e^{2\pi i \frac{nk}{\frac{N}{2}}} x_{2n+1} \\ &= X_k^{(\text{even})} + e^{-2\pi i \frac{k}{N}} X_k^{(\text{odd})}. \end{aligned} \tag{111}$$

In this result $X_k^{(\text{even})}$ is the k^{th} component of the Fourier transformation of length $\frac{N}{2}$ from the even components of the original $\vec{x}$ while $X_k^{(\text{odd})}$ are the odd components. These subdivisions can be written more compactly as X_k^e and X_k^o and additional subdivisions can be denoted by sequences of e's and o's in the superscript. The algorithm functions by zero padding the input to obtain a

vector of length 2^n for any integer n and recursively dividing each new vector until all segments are of length 1. The transform of such an array is the identity operator that copies its one input number into the output slot. That is, for every pattern of $\ln_2 N$ even and odd subdivisions, there is a one-point transformation that is just a transform of input numbers x_n,

$$x_n = X_k^{eoeooeoeoeeeeoeoe...eoeooe}, \qquad \text{for some } n.$$

The remaining step is to determine which value of n corresponds to which pattern of e's and o's in the definition above. The relation can be found by reversing the order in the superscript and changing $e \to 0$, $o \to 1$. This gives the value of n in binary. The combination of the Danielson-Lanczos subdivision method with this bit reversal makes the FFT useful [63, 62, 61]. Although an FFT routine is straightforward to write, more robust routines are available for use. In this project, all Fourier analysis has been done using the FFTW package of routines [64].

Beamforming Methods

In this section we set up the general problem of determining the direction of arrival, or DOA, for a signal incident on an array of sensors. The direction of arrival can be calculated using the time delay between when a signal is recorded on one microphone relative to another. Far from the source, acoustic energy propagates as a planar wave. A plane wave's velocity can be written in terms of the angles it makes with the horizontal, θ, and x-axis, ϕ,

$$\vec{v} = \begin{pmatrix} v\cos\theta\cos\phi \\ v\cos\theta\sin\phi \\ v\sin\theta \end{pmatrix}.$$

From this parameterization, the horizontal velocity at which the plane wave travels across the array can be denoted by $\vec{v}_{\text{tr}} = \frac{v}{\cos\theta}\begin{pmatrix}\cos\phi \\ \sin\phi\end{pmatrix}$ and is termed the "trace velocity" of the plane wave. For an acoustic plane wave with trace velocity $\vec{v}_{\text{tr}}$ incident on an array of microphones, the time delay

between when the signal reaches microphones i and j can be written

$$\frac{x_{i,j}}{v_{\mathrm{tr},x}} + \frac{y_{i,j}}{v_{\mathrm{tr},y}} = \tau_{i,j} \quad \rightarrow \quad \begin{pmatrix} x_{1,2} & y_{1,2} \\ x_{1,3} & y_{1,3} \\ \vdots & \vdots \\ x_{p-1,p} & y_{p-1,p} \end{pmatrix} \begin{pmatrix} \frac{1}{v_{\mathrm{tr},x}} \\ \frac{1}{v_{\mathrm{tr},y}} \end{pmatrix} = \begin{pmatrix} \tau_{1,2} \\ \tau_{1,3} \\ \vdots \\ \tau_{p-1,p} \end{pmatrix}. \tag{112}$$

This equation can be written more compactly in the form $\boldsymbol{D}\vec{w} = \vec{\tau}$ where $\vec{w} = \begin{pmatrix} v_{\mathrm{tr},x}^{-1} \\ v_{\mathrm{tr},y}^{-1} \end{pmatrix}$ is termed the slowness vector [58, 65].

A DOA approximation can be made by finding a least squares error solution of Eq. (112) using the pseudo inverse of the matrix of sensor separations and a measured vector of time delays,

$$\hat{\vec{w}} = \left(\boldsymbol{D}^{\dagger}\boldsymbol{D}\right)^{-1}\boldsymbol{D}^{\dagger}\tilde{\vec{\tau}}. \tag{113}$$

The time delays can be found by determining the maximum cross correlation $\tilde{\tau}_{i,j} = \max\left[\tilde{R}_{i,j}(\tau)\right]$. Because of wind and other noise sources, the above relation will not be exact. A measure of the accuracy of this solution can be calculated from the residual,

$$\vec{\varepsilon} = \vec{\tau} - \boldsymbol{D}\vec{w} \quad \rightarrow \quad \hat{\vec{\varepsilon}} = \left[\boldsymbol{I} - \boldsymbol{D}\left(\boldsymbol{D}^{\dagger}\boldsymbol{D}\right)^{-1}\boldsymbol{D}^{\dagger}\right]\tilde{\vec{\tau}}. \tag{114}$$

The ratio $\frac{||\hat{\vec{\varepsilon}}||^2}{||\tilde{\vec{\tau}}||^2}$ measures how much of the signal is not accounted for by the plane wave defined by $\hat{\vec{w}}$. This DOA approximation has several limitations, most notably that there is no control of look direction. The pseudo inverse simply determines the plane wave direction which minimizes the difference between $\boldsymbol{D}\hat{\vec{w}}$ and $\tilde{\vec{\tau}}$. Additionally, if multiple plane waves are incident on the array of microphones, this algorithm has no way of resolving them.

In order to obtain a more sophisticated DOA approximation method, one can construct a model for the signal recorded on each element of the array. For q plane waves incident on an array of microphones, the signal detected on the i^{th} microphone can be modeled by

$$x_i(t) = \sum_{j=1}^{q} F_j\left(t - \tau_i^{(j)}\right) + n_i(t), \quad \tau_i^{(j)} = \vec{w}_j \cdot \vec{z}_i, \tag{115}$$

where $F_j(t)$ is the waveform of the j^{th} plane wave, $\vec{z}_i$ is the two dimensional location of the i^{th} sensor, and $n_i(t)$ describes all other contributions to the data record on the i^{th} sensor. It is useful to assume a single signal and perform some analysis of this result.

Time Domain Analysis. Due to the continuous nature of the microbarom signal, only frequency domain analysis is used in this project. However, the time domain result for this analysis is straightforward. Using the above definition,

$$\begin{aligned}
R_{i,j}(\tau) &= \lim_{T\to\infty}\frac{1}{T}\int_0^T x_i(t)\,x_j(t+\tau)dt \\
&= \lim_{T\to\infty}\frac{1}{T}\int_0^T \left[F(t-\tau_i)+n_i(t)\right]\left[F(t-\tau_j+\tau)+n_j(t+\tau)\right]dt \\
&= \lim_{T\to\infty}\frac{1}{T}\int_0^T F(t-\tau_i)\,F(t-\tau_j+\tau)dt \\
&\qquad + \lim_{T\to\infty}\frac{1}{T}\int_0^T F(t-\tau_i)\,n_j(t+\tau)dt \\
&\qquad\qquad + \lim_{T\to\infty}\frac{1}{T}\int_0^T n_i(t)\,F(t-\tau_j+\tau)dt \\
&\qquad\qquad\qquad + \lim_{T\to\infty}\frac{1}{T}\int_0^T n_i(t)\,n_j(t+\tau)dt \\
&= \lim_{T\to\infty}\frac{1}{T}\int_0^T F(t-\tau_i)\,F(t-\tau_j+\tau)dt + \lim_{T\to\infty}\frac{1}{T}\int_0^T n_i(t)\,n_j(t+\tau)dt,
\end{aligned}$$

where we've set the cross terms to zero because the signal and noise are assumed to be incoherent. The correlation matrices of the signal and noise then have the forms,

$$R^{(F)}_{i,j}(\tau) = \lim_{T\to\infty}\frac{1}{T}\int_0^T F(t-\tau_i)\,F(t-\tau_j+\tau)dt, \tag{116a}$$

$$R^{(n)}_{i,j}(\tau) = \lim_{T\to\infty}\frac{1}{T}\int_0^T n_i(t)\,n_j(t+\tau)dt \approx \sigma_n^2\delta_{ij}, \tag{116b}$$

where the simplification of the noise correlation coefficients is the result of assuming constant incoherent white noise. Note that the diagonal elements of $\boldsymbol{R}^{(F)}(\tau)$ are proportional to the signal strength while those of $\boldsymbol{R}^{(n)}(\tau)$ are equal to the noise power. Because of this, one expects $R^{(F)}_{i,i}(0) > \sigma_n^2(0)$ when a strong coherent signal is present.

Frequency Domain Analysis. The modeled signal can be Fourier transformed and written in the frequency domain as

$$X_i(f) = \sum_{j=1}^{q} \mathcal{F}_j(f)\, e^{2\pi i f \tau_i^{(j)}} + \eta_i(f). \tag{117}$$

which simplifies to $X_i(f) = \mathcal{F}(f)\, e^{2\pi i f \tau_i} + \eta_i(f)$ in the case of a single plane wave. From this result, the cross spectral density matrix can easily be derived,

$$\begin{aligned}
S_{i,j}(f) &= \lim_{T\to\infty} \frac{1}{T} X_i(f)\, X_j^*(f) \\
&= \lim_{T\to\infty} \left[\mathcal{F}(f)\, e^{2\pi i f \tau_i} + \eta_i(f)\right] \left[\mathcal{F}^*(f)\, e^{-2\pi i f \tau_j} + \eta_j^*(f)\right] \\
&= \lim_{T\to\infty} |\mathcal{F}(f)|^2\, e^{2\pi i f(\tau_i - \tau_j)} \\
&\qquad + \lim_{T\to\infty} \mathcal{F}(f)\, e^{2\pi i f \tau_i} \eta_j^*(f) + \lim_{T\to\infty} \eta_i(f)\, \mathcal{F}^*(f)\, e^{2\pi i f \tau_j} \\
&\qquad\qquad + \lim_{T\to\infty} \eta_i(f)\, \eta_j^*(f) \\
&= \lim_{T\to\infty} |\mathcal{F}(f)|^2\, e^{2\pi i f(\tau_i - \tau_j)} + \lim_{T\to\infty} \eta_i(f)\, \eta_j^*(f).
\end{aligned}$$

Again we've separated the signal and noise cross spectral densities,

$$S_{i,j}^{(\mathcal{F})}(f) = \lim_{T\to\infty} |\mathcal{F}(f)|^2\, e^{2\pi i f(\tau_i - \tau_j)}, \tag{118a}$$

$$S_{i,j}^{(\eta)}(f) = \lim_{T\to\infty} \eta_i(f)\, \eta_j^*(f) \approx \sigma_\eta^2(f)\, \delta_{i,j}. \tag{118b}$$

Note again that the diagonal elements of $\boldsymbol{S}^{(\mathcal{F})}$ are proportional to the signal strength while those of $\boldsymbol{S}^{(\eta)}$ are proportional to the noise power. At frequencies which contain coherent energy, $S_{i,i}^{(\mathcal{F})}(f) \gg \sigma_\eta^2(f)$.

Given these alternate representations of the correlation and spectral density matrices, the formulation of beam methods is straightforward. The central idea of beamforming is to define a "beam" by a slowness vector $\vec{w}$ and determine some measure of the field in that direction, termed the spatial spectrum. In the frequency domain, one can define a steering vector $\vec{\Phi}(\vec{w}, f)$ which produces the phase shifts expected in Eq. (117). For a single plane wave incident on an array of

sensors, the steering vector is a vector of length p with elements defined by

$$\Phi_j\left(\vec{w}, f\right) = e^{2\pi i f(\vec{w}\cdot\vec{z}_j)}. \tag{119}$$

The steering vector(s) which produce local maxima in the spatial spectrum correspond to the DOA estimate(s). From a linear algebra point of view, all beamforming reduces to expressing $\vec{\Phi}$ in terms of the eigenvectors of $\boldsymbol{S}\left(f\right)$ and performing some analysis of the projection on the different eigenvectors. The matrix $\boldsymbol{S}$ is positive definite and therefore its eigenvectors, $\vec{v}_j^{(\boldsymbol{S})}$, and eigenvalues, $\lambda_j^{(\boldsymbol{S})}$, define a p dimensional vector space [35]. At each frequency,

$$\boldsymbol{S} = \boldsymbol{U}\boldsymbol{\Lambda}\boldsymbol{U}^{\dagger}, \quad \boldsymbol{U} = \begin{pmatrix} \vec{v}_1^{(\boldsymbol{S})} & \vec{v}_2^{(\boldsymbol{S})} & \dots & \vec{v}_p^{(\boldsymbol{S})} \end{pmatrix}, \quad \boldsymbol{\Lambda} = \begin{pmatrix} \lambda_1^{(\boldsymbol{S})} & 0 & 0 \\ 0 & \ddots & 0 \\ 0 & 0 & \lambda_p^{(\boldsymbol{S})} \end{pmatrix}, \tag{120a}$$

$$\boldsymbol{S}\vec{v}_j^{(\boldsymbol{S})} = \lambda_j^{(\boldsymbol{S})}\vec{v}_j^{(\boldsymbol{S})} \quad \text{for } j = 1, 2, \dots p. \tag{120b}$$

Further, the steering vector, $\vec{\Phi}$, can be expanded in terms of the eigenvectors of $\boldsymbol{S}$ at each frequency,

$$\vec{\Phi} = \sum_{j=1}^{p} \left(\vec{\Phi}\cdot\vec{v}_j^{(\boldsymbol{S})}\right)\vec{v}_j^{(\boldsymbol{S})} = \sum_{j=1}^{p} c_j^{(\vec{\Phi})}\,\vec{v}_j^{(\boldsymbol{S})}. \tag{120c}$$

where $c_j^{(\vec{\Phi})}$ is the projection of the steering vector on the j^{th} eigenvector of $\boldsymbol{S}$. Once each beamforming method is derived, it is useful to return to this notation and analyze the resulting spatial spectrum in terms of $c_j^{(\vec{\Phi})}$.

In order to derive the spatial spectra in each method, the power in the signal is calculated using a weighted version of the actual data, $\tilde{\vec{X}}\left(f\right)$. One writes the estimate of the signal as a linear function,

$$\hat{\mathcal{F}}\left(\vec{w}, f\right) = \vec{\nu}^{\dagger}\left(\vec{\Phi}, \boldsymbol{S}\right)\tilde{\vec{X}}\left(f\right), \tag{121}$$

where the weighting vector $\vec{\nu}$ is defined to satisfy some criterion proposed by the beamforming method. Several formulations are presented in the literature, however, the most commonly used beamforming methods are the Bartlett and Capon beams [66, 67, 68, 69]. In the following discussion these two methods will be derived along with two methods which extend the results to account

for multiple signals. Once a form for $\vec{\nu}$ is determined, the corresponding spatial spectrum can be calculated using a statistical average of $\left|\hat{\mathcal{F}}\left(\vec{\Phi}, f\right)\right|^2$ [58],

$$\begin{aligned} P\left(\vec{\nu}\right) &= \left\langle \left|\vec{\nu}^{\dagger}\tilde{\vec{X}}\right|^2 \right\rangle = \vec{\nu}^{\dagger}\left\langle \tilde{\vec{X}} \otimes \tilde{\vec{X}}^{\dagger} \right\rangle \vec{\nu} \\ &= \vec{\nu}^{\dagger}(\vec{\Phi})\hat{\boldsymbol{S}}(f)\vec{\nu}(\vec{\Phi}). \end{aligned} \tag{122}$$

In order to define the weighting function, we combine Eq. (119) with the model in Eq. (117) for a single plane wave,

$$\vec{X}\left(f\right) = \mathcal{F}\left(f\right)\vec{\Phi}\left(\vec{w}, f\right) + \vec{\eta}\left(f\right). \tag{123}$$

The spatial spectrum in Eq. (122) can be used to write the expected spatial spectrum by replacing $\tilde{\vec{X}}$ with $\vec{X}$,

$$\begin{aligned} \left\langle \left|\vec{\nu}^{\dagger}\vec{X}\right|^2 \right\rangle &= \vec{\nu}^{\dagger}\left\langle \vec{X} \otimes \vec{X}^{\dagger} \right\rangle \vec{\nu} \\ &= \vec{\nu}^{\dagger}\left\langle \left[\mathcal{F}\vec{\Phi} + \vec{\eta}\right] \otimes \left[\mathcal{F}^{*}\vec{\Phi}^{\dagger} + \vec{\eta}^{\dagger}\right] \right\rangle \vec{\nu} \\ &= \left\langle \left|\mathcal{F}\right|^2 \right\rangle \left|\vec{\nu}^{\dagger}\vec{\Phi}\right|^2 + \sigma_{\eta}^2 \left|\vec{\nu}\right|^2, \end{aligned} \tag{124}$$

where we've used the assumptions $\left\langle \mathcal{F}\vec{\Phi} \otimes \vec{\eta}^{\dagger} \right\rangle = 0$, $\left\langle \vec{\eta} \otimes \mathcal{F}^{*}\vec{\Phi}^{\dagger} \right\rangle = 0$, and $\left\langle \vec{\eta} \otimes \vec{\eta}^{\dagger} \right\rangle = \sigma_{\eta}^2 \boldsymbol{I}$. This result can be used to determine $\vec{\nu}\left(\vec{\Phi}, \boldsymbol{S}\right)$ for a given criterion.

The Bartlett Beam

The conventional, or Bartlett, beamforming algorithm seeks a normalized weighting function $\left|\vec{\nu}\left(\vec{\Phi}, \boldsymbol{S}\right)\right| = 1$ which maximizes the spatial spectrum [66]. Normalizing $\vec{\nu}\left(\vec{\Phi}, \boldsymbol{S}\right)$ fixes the noise term in Eq. (124). The first term in Eq. (124) is maximized when $\vec{\nu}$ is parallel to $\vec{\Phi}$ which leads to the normalized weighting,

$$\vec{\nu}^{(B)}\left(\vec{\Phi}, \boldsymbol{S}\right) = \frac{\vec{\Phi}\left(\vec{w}, f\right)}{\sqrt{\vec{\Phi}^{\dagger}\left(\vec{w}, f\right)\vec{\Phi}\left(\vec{w}, f\right)}}. \tag{125}$$

Inserting this result into Eq. (122), one finds [66],

$$\begin{aligned} P^{(B)}(\vec{w}, f) &= \vec{\nu}^{\dagger}(\vec{\Phi}, \boldsymbol{S})\hat{\boldsymbol{S}}(f)\vec{\nu}(\vec{\Phi}, \boldsymbol{S}) \\ &= \frac{\vec{\Phi}^{\dagger}(\vec{w}, f)}{\sqrt{\vec{\Phi}^{\dagger}(\vec{w}, f)\vec{\Phi}(\vec{w}, f)}^{*}}\hat{\boldsymbol{S}}(f)\frac{\vec{\Phi}(\vec{w}, f)}{\sqrt{\vec{\Phi}^{\dagger}(\vec{w}, f)\vec{\Phi}(\vec{w}, f)}} \\ &= \frac{\vec{\Phi}^{\dagger}(\vec{w}, f)\hat{\boldsymbol{S}}(f)\vec{\Phi}(\vec{w}, f)}{|\vec{\Phi}(\vec{w}, f)|^2}. \end{aligned} \tag{126}$$

Referring back to Eq. (120), this spatial spectra can be written in the form,

$$\begin{aligned} P^{(B)}(\vec{w}, f) &= \frac{1}{p}\sum_{j=1}^{p}\lambda_j^{(\boldsymbol{S})}(f)\left|\vec{\Phi}(\vec{w}, f)\cdot\vec{v}_j^{(\boldsymbol{S})}(f)\right|^2 \\ &= \frac{1}{p}\sum_{j=1}^{p}\lambda_j^{(\boldsymbol{S})}(f)\left|c_j^{(\vec{\Phi})}(\vec{w}, f)\right|^2. \end{aligned} \tag{127}$$

The coefficients $c_j^{(\vec{\Phi})}(\vec{w}, f)$ measure how much of $\vec{\Phi}(\vec{w}, f)$ is projected onto $\vec{v}_j^{(\boldsymbol{S})}(f)$, and therefore the Bartlett beamformer searches for a solution which is dominated by projections on the eigenvectors associated with the largest eigenvalues. The Bartlett beamformer has some limitations in resolving multiple incident signals when their back azimuths are separated by small angles because it uses every degree of freedom in the model to concentrate the signal along the beam into the spatial spectrum.

The Capon Beam

In order to alleviate the resolution limitations of the Bartlett beamformer, the Capon method (also termed the Minimum Variance Distortionless Response filter) was developed [67, 68]. The spatial spectrum for the Capon beamformer is defined by

$$\min\left[\left\langle|\mathcal{F}(f)|^2\right\rangle\left|\vec{\nu}^{\dagger}\vec{\Phi}\right|^2 + \sigma^2|\vec{\nu}|^2\right],$$
$$\text{subject to } \left|\vec{\nu}^{\dagger}\vec{\Phi}\right| = 1.$$

The physical meaning of this weighting is that the gain in the look direction is held fixed by the second condition. Then, the contribution to the spatial spectrum from noise and signals off-beam

is minimized. The optimizing weighting function can be found by Lagrange multipliers [67],

$$\vec{\nu}^{(C)}\left(\vec{\Phi}, \boldsymbol{S}\right) = \frac{\hat{\boldsymbol{S}}^{-1}(f)\vec{\Phi}\left(\vec{w}, f\right)}{\vec{\Phi}^{\dagger}\left(\vec{w}, f\right)\hat{\boldsymbol{S}}^{-1}(f)\vec{\Phi}\left(\vec{w}, f\right)}. \tag{128}$$

Again, inserting the weighting into Eq. (122) gives the Capon beamformer spatial spectrum [67, 68],

$$\begin{aligned} P^{(C)}\left(\vec{w}, f\right) &= \vec{\nu}^{\dagger}(\vec{\Phi}, \boldsymbol{S})\hat{\boldsymbol{S}}(f)\vec{\nu}(\vec{\Phi}, \boldsymbol{S}) \\ &= \frac{\vec{\Phi}^{\dagger}(\vec{w}, f)\hat{\boldsymbol{S}}^{-1}(f)}{\left(\vec{\Phi}^{\dagger}(\vec{w}, f)\hat{\boldsymbol{S}}^{-1}(f)\vec{\Phi}\right)^{*}(\vec{w}, f)}\hat{\boldsymbol{S}}(f)\frac{\hat{\boldsymbol{S}}^{-1}(f)\vec{\Phi}(\vec{w}, f)}{\vec{\Phi}^{\dagger}(\vec{w}, f)\hat{\boldsymbol{S}}^{-1}(f)\vec{\Phi}(\vec{w}, f)} \\ &= \frac{\vec{\Phi}^{\dagger}(\vec{w}, f)\left(\hat{\boldsymbol{S}}^{-1}(f)\hat{\boldsymbol{S}}(f)\right)\hat{\boldsymbol{S}}^{-1}(f)\vec{\Phi}(\vec{w}, f)}{\left|\vec{\Phi}^{\dagger}(\vec{w}, f)\hat{\boldsymbol{S}}^{-1}(f)\vec{\Phi}(\vec{w}, f)\right|^{2}} \\ &= \frac{1}{\vec{\Phi}^{\dagger}(\vec{w}, f)\hat{\boldsymbol{S}}^{-1}(f)\vec{\Phi}(\vec{w}, f)}. \end{aligned} \tag{129}$$

The inverse spatial spectrum matrix, $\hat{\boldsymbol{S}}^{-1}(f)$, contains the inverse of the matrix $\boldsymbol{\Lambda}$ in Eq. (120). $\boldsymbol{\Lambda}^{-1}$ in a diagonal matrix with λ_j^{-1} along the diagonal. From Eq.(118) and the discussion following it, we can infer that in such a case, the previously small noise eigenvalues become dominant and the previously larger signal eigenvectors become relatively small. Therefore the vector space associated with $\hat{\boldsymbol{S}}^{-1}(f)$ is dominated by the noise eigenvectors. Again referring back to Eq. (120), the Capon spatial spectra can be written in the alternate form,

$$\begin{aligned} P^{(C)}\left(\vec{w}, f\right) &= \frac{1}{\sum_{j=1}^{p}\frac{1}{\lambda_j^{(\boldsymbol{S})}(f)}\left|\vec{\Phi}(\vec{w}, f)\cdot\vec{v}_j^{(\boldsymbol{S})}(f)\right|^{2}} \\ &= \left[\sum_{j=1}^{p}\frac{1}{\lambda_j^{(\boldsymbol{S})}(f)}\left|c_j^{(\vec{\Phi})}(\vec{w}, f)\right|^{2}\right]^{-1}. \end{aligned} \tag{130}$$

Thus, the spatial spectrum searches for solutions which have the smallest projections on the eigenvectors associated with the smallest eigenvalues. This provides the basis for the description of this spatial spectrum as a minimum variance distortionless response filter [35, 67, 68]. Unlike the Bartlett method, some noise suppression capability is sacrificed in order to reduce both coherent and incoherent energy away from the beam direction. This results in a spatial spectrum which reduces spectral leakage from closely spaced sources and has superior spatial resolution compared

to the Bartlett method [67, 68].

The MUSIC Beam

An additional method was developed by Schmidt which is similar in function to the Bartlett and Capon beamforming methods, though its aim is to identify multiple coherent signals and therefore its derivation is slightly different [70]. In the Capon beamformer, the inverse of $\hat{\boldsymbol{S}}$ was used to spatially filter for steering vectors near the null space of the inverse matrix, which is dominated by the noise eigenvectors. Consider if, instead, one simply extracts the noise eigenvectors from $\hat{\boldsymbol{S}}$ and finds steering vectors which are near the null space of the noise. Combining the results of Eq. (118) with (120), we expect to be able to write the decomposition of $\hat{\boldsymbol{S}}$ in the form,

$$\begin{aligned}\hat{\boldsymbol{S}}(f) &= \boldsymbol{U}_{\text{sig}}(f)\boldsymbol{\Lambda}_{\text{sig}}(f)\boldsymbol{U}_{\text{sig}}^{\dagger}(f) + \boldsymbol{U}_{\eta}(f)\boldsymbol{\Lambda}_{\eta}(f)\boldsymbol{U}_{\eta}^{\dagger}(f) \\ &\approx \boldsymbol{U}_{\text{sig}}(f)\boldsymbol{\Lambda}_{\text{sig}}(f)\boldsymbol{U}_{\text{sig}}^{\dagger}(f) + \sigma_{\eta}^{2}(f)\boldsymbol{I},\end{aligned} \tag{131}$$

where we've separated the eigenvalues and eigenvectors associated with the coherent signal from those associated with incoherent noise. In realistic data, the distinction between signal and noise eigenvalues is more complicated. In the high SNR case, this separation is possible because $\lambda_j(f) \sim \sigma_{\eta}^2(f)$ for all noise eigenvectors where $\sigma_{\eta}^2(f)$ is the noise power, and $\lambda_k(f) \gg \sigma_{\eta}^2(f)$ for k denoting a signal eigenvector. In the lower SNR case, this separation is difficult and more robust methods must be used. Such methods will be developed later in this chapter. For now, let's assume for now that we've determined there to be q coherent signals incident on the array ($q < p$).

$$\boldsymbol{\Lambda}_{\text{sig}}(f) = \begin{pmatrix} \lambda_1(f) & & \mathbf{0} \\ & \ddots & \\ \mathbf{0} & & \lambda_q(f) \end{pmatrix}, \qquad \boldsymbol{U}_{\text{sig}}(f) = \begin{pmatrix} \vec{v}_1(f) & \cdots & \vec{v}_q(f) \end{pmatrix},$$

$$\boldsymbol{\Lambda}_{\eta}(f) = \begin{pmatrix} \lambda_{q+1}(f) & & \mathbf{0} \\ & \ddots & \\ \mathbf{0} & & \lambda_p(f) \end{pmatrix}, \qquad \boldsymbol{U}_{\eta}(f) = \begin{pmatrix} \vec{v}_{q+1}(f) & \cdots & \vec{v}_p(f) \end{pmatrix}.$$

Any vector orthogonal to $\boldsymbol{U}_{\text{sig}}(f)$ can be expressed as a linear combination of the eigenvectors in $\boldsymbol{U}_{\eta}(f)$ and vice versa [35]. Because the eigenvectors in $\boldsymbol{U}_{\eta}(f)$ are orthogonal to the signal

vector space, we seek steering vectors which are as orthogonal as possible to the vector space of the noise. That is,

$$\boldsymbol{U}_\eta^\dagger(f)\vec{\Phi}\,(\boldsymbol{w},f)\sim 0 \qquad \text{for the true DOAs.}$$

A projection operator, $\boldsymbol{\Pi}_\eta^{(q)}(f)=\boldsymbol{U}_\eta(f)\boldsymbol{U}_\eta^\dagger(f)$, can be constructed and the multiple signal classification or MUSIC spatial spectrum is then defined by [70, 58]

$$P_q^{(M)}\,(\vec{w},f)=\frac{\vec{\Phi}^\dagger(f)\vec{\Phi}(f)}{\vec{\Phi}^\dagger(f)\boldsymbol{\Pi}_\eta^{(q)}(f)\vec{\Phi}(f)}. \tag{132}$$

Using the representations in Eq. (120) and (131), we can alternately write this spatial spectrum as

$$P_q^{(M)}\,(\vec{w},f)=\left[\frac{1}{p}\sum_{j=q+1}^{p}\left|\vec{\Phi}\,(\vec{w},f)\cdot\vec{v}_j^{(\boldsymbol{S})}(f)\right|^2\right]^{-1}=\left[\frac{1}{p}\sum_{j=q+1}^{p}\left|c_j^{(\vec{\Phi})}\,(\vec{w},f)\right|^2\right]^{-1}. \tag{133}$$

That is, if one expands $\vec{\Phi}$ in terms of the eigenvectors of $\boldsymbol{S}$ and separates the summation as

$$\begin{aligned}\vec{\Phi}(\vec{w},f)&=\sum_{j=1}^{q}c_j^{(\vec{\Phi})}(\vec{w},f)\vec{v}_j^{(\boldsymbol{S})}(f)+\sum_{j=q+1}^{p}c_j^{(\vec{\Phi})}(\vec{w},f)\vec{v}_j^{(\boldsymbol{S})}(f)\\&=\vec{\Phi}_{\text{sig}}(\vec{w},f)+\vec{\Phi}_\eta(\vec{w},f),\end{aligned} \tag{134}$$

one seeks a solution which minimizes $|\vec{\Phi}_\eta(\vec{w},f)|^2$. It should be noted that $P_q^{(M)}\,(\vec{w},f)$ is not a true spectrum in any sense, but instead is a measure of the distance between a given steering vector and the vector subspace associated with the noise. However, it does exhibit peaks for $\vec{\Phi}$ in the vicinity of the true DOAs.

The Dominant Mode Rejection Beam

In addition to the MUSIC spatial spectrum discussed in the previous section, other beamforming methods using the eigenvalue structure of the spectral density matrix have been developed. One such method is the Dominant Mode Rejection, or DMR, beamformer. The DMR beamformer uses an eigenvalue decomposition and separates the eigenvalues and eigenvectors of the spectral density matrix into those associated with signal and noise as the MUSIC spatial spectra does, however it includes all eigenvectors in the calculating, with the average of the eigenvalues for the noise eigenvectors, $\bar{\lambda}^{(\boldsymbol{S})}$, replacing the exact values [71]. The DMR spectrum is calculated similarly

to the Capon beamformer in Eq. (130),

$$P^{(DMR)}\left(\vec{w},f\right) = \left[\sum_{j=1}^{q}\frac{1}{\lambda_j^{(\boldsymbol{S})}(f)}\left|c_j^{(\vec{\Phi})}(\vec{w},f)\right|^2 + \frac{1}{\bar{\lambda}_\eta^{(\boldsymbol{S})}\left(f\right)}\sum_{j=q+1}^{p}\left|c_j^{(\vec{\Phi})}(\vec{w},f)\right|^2\right]^{-1} \tag{135a}$$

$$= \bar{\lambda}_\eta^{(\boldsymbol{S})}\left(f\right)\left[\sum_{j=1}^{q}\frac{\bar{\lambda}_\eta^{(\boldsymbol{S})}\left(f\right)}{\lambda_j^{(\boldsymbol{S})}(f)}\left|c_j^{(\vec{\Phi})}(\vec{w},f)\right|^2 + \sum_{j=q+1}^{p}\left|c_j^{(\vec{\Phi})}(\vec{w},f)\right|^2\right]^{-1}. \tag{135b}$$

Typically, the form of the beamformer in Eq. (135a) is used to compute the beam. However, it is useful to analyze the behavior of the beamformer using the second form in Eq. (135b). It is expected that $\lambda_j^{(\boldsymbol{S})}(f) \gg \bar{\lambda}_\eta^{(\boldsymbol{S})}(f)$ when a signal is present and the correct number of signals is assumed. Therefore, in such a case, the DMR spatial spectrum exhibits peaks in the regions where the sum in the second term is nearly zero.

The averaging used in defining $\bar{\lambda}_\eta^{(\boldsymbol{S})}$ allows one to use the beamformer without requiring that the sensor to snapshot ratio be less than unity. Recall that the spatial spectrum matrix, $\boldsymbol{S}$, has been estimated by averaging $\vec{X}\left(f\right) \otimes \vec{X}^\dagger\left(f\right)$ over multiple snapshots. Therefore, if fewer than p snapshots were used in this estimation, the matrix cannot be full rank. In such a case, the lowest eigenvalues are zero and the inversion required to use the Capon beamformer cannot be calculated. Thus, the dominant mode rejection can be used as an estimate of the Capon spatial spectrum in the case that $\boldsymbol{S}$ is rank deficient.

Comparing Eq. (135b) with the definition of the MUSIC spatial spectra in Eq. (133), we find that in this case the DMR and MUSIC spatial spectra are simply scaled versions of one another. Consider the different case in which one of the noise eigenvalues has been assumed to be signal and is left out of the averaging to find $\bar{\lambda}_\eta^{(\boldsymbol{S})}$. In such a case the ratio of $\lambda_j^{(\boldsymbol{S})}$ to $\bar{\lambda}_\eta^{(\boldsymbol{S})}$ will be nearly unity (not the very small value it would be if $\lambda_j^{(\boldsymbol{S})}$ were actually a signal eigenvalue) and the corresponding coefficient $|c_j|^2$ is kept in the summation. Thus, the DMR functions reproduces a scaled version of the MUSIC spatial spectrum in the case that the signal power is very high and the correct number of signals is input, however, it is less likely to fail when the number of signals is not correct.

Developing a Processing Routine for Microbaroms

In this section, we present a rigorous development of a data processing routine to be used to extract the microbarom signal from the data record of an array of microphones. The development of this routine has focused on determining the most effective method to achieve the following,

- Approximate the true spectral density matrix $\boldsymbol{S}(f)$ by some $\hat{\boldsymbol{S}}(f)$.
- Determine which of the beamforming methods most efficiently identifies microbaroms in the data. Specific attention is being paid to develop a method to detect multiple microbaroms in noisy data.
- Use the model in Eq. (117) to separate the signal and noise and, if possible, determine the signal count which best explains the data.

Approximating the Spectral Density Matrix and Applying a Data Adaptive Filter

Unlike analysis of transient signals, the signal to noise ratio of a continuous signal can be enhanced by taking a long recording and averaging over sub-windows to reduce the incoherent noise in the data record. During a large window of time, several snapshots of data within the larger window can be used to obtain a statistical average of the spectral density matrix. That is,

$$\hat{\boldsymbol{S}}\left(f\right) = \left\langle \tilde{\vec{X}}\left(f\right) \otimes \tilde{\vec{X}}^{\dagger}\left(f\right) \right\rangle_{\text{snap shots}}. \tag{136}$$

The limitations on the size of the window and snapshots is determined by the physical system of interest. The large window must be sufficiently small to guarantee that the source satisfies the assumption of stationarity but large enough to provide at least p independent snap shots so that $\hat{\boldsymbol{S}}\left(f\right)$ is full rank. The sub-window snapshots must be sufficiently large to record several cycles of the phenomenon of interest, and should be large enough to provide adequate frequency resolution. Recall that the frequency resolution from the DFT is $df = \frac{1}{T_{\text{snap shot}}}$.

For microbaroms, the band of frequencies which are dominant ranges from 0.15 to 0.3 Hz which corresponds to a maximum possible period of ~ 6 seconds. Fig. 19 shows how the snapshots overlap across the larger window. In order to maintain the assumption of stationarity and include

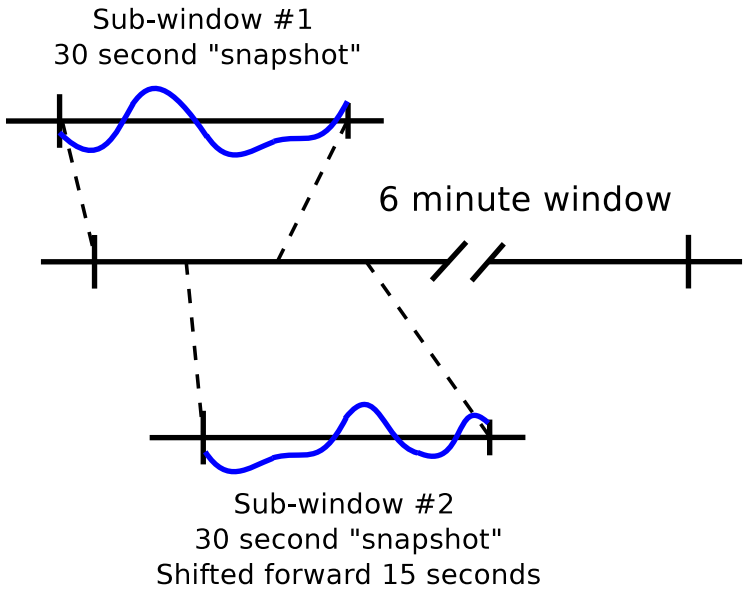

Fig. 19: A large window of data is broken into overlapping snapshots of data and the spectral density matrix is estimated by $\hat{\boldsymbol{S}}(f) = \left\langle \vec{X}(f) \otimes \vec{X}^{\dagger}(f) \right\rangle_{\text{snap shots}}$.

sufficient microbarom cycles, we have elected to use a larger window of 6 minutes with 30 second snapshots. Within each snap shot, the 30 seconds of data is scaled using a Hann window,

$$\mathcal{W}(n) = \frac{1}{2}\left(1 - \cos\left(\frac{2\pi n}{N-1}\right)\right), \tag{137}$$

which reduces spectral leakage [61]. Additionally, 15 seconds of zero padding are added before and after the actual data, resulting in a one minute time sample with 30 seconds of windowed data at its center. The resulting time data for a sample snapshot is shown in Fig. 20. Snapshots are overlapped to compensate for the windowing and allow all data to contribute to the averaged spectral density matrix.

Once a statistically determined spectral density matrix has been calculated, the pure state filter in Eq. (107) can be used to calculate the strength of the coherence at each frequency on interest. These values can then be used to determine the weighting function $\vec{\varrho}(f)$, at discrete frequency bins f_k,

$$\varrho_k = \frac{\gamma_{(\text{filter})}\left[\hat{\boldsymbol{S}}(f_k)\right]}{\sum_{j=1}^{K} \gamma_{(\text{filter})}\left[\hat{\boldsymbol{S}}(f_j)\right]}. \tag{138}$$

Note that the γ filter is not squared in this relation, so one must take the square root of the result from Eq. (107). Any quantity $A = \sum \mathcal{A}_k \varrho_k$ is simply the weighted average of $\mathcal{A}_k$ where frequencies with strongly coherence frequencies weighted more heavily than those with weaker coherence. It is

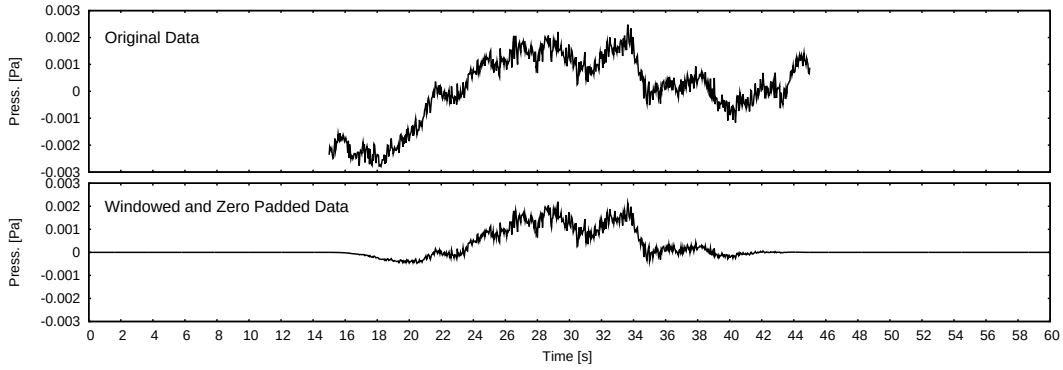

Fig. 20: The original data is scaled using a Hann window to eliminate edge effects and zero padded to double the snapshot length and reduce spectral leakage.

easily seen that if all frequencies are uniformly coherent, one finds $\varrho_k = \frac{1}{K}$ for all bins and a simple average is calculated $A = \frac{1}{K}\sum \mathcal{A}_k$.

Evaluation of Beamformer Performance

In order to compare the performance of the beamforming methods discussed previously, we have elected to use a combination of synthesized data using Eq. (117) as a model and actual microbarom data detected during Hurricane Igor in September of 2010. The synthesized data is generated by,

$$X_j\left(\vec{w},f\right) = \sum_{n=1}^{q} \mathcal{R}_{\mu_{\mathcal{F}},\sigma_{\mathcal{F}}}\left(n,f\right)\vec{\Phi}\left(\vec{w}_n,f\right) + \mathcal{R}_{\mu_\eta,\sigma_\eta}\left(f\right) \tag{139}$$

where $\mathcal{R}_{\mu,\sigma}$ is a random number generator with mean amplitude μ and variance σ. For our analysis, we've used mean amplitudes $\mu_{\mathcal{F}} = \sqrt{\text{SNR}}$ and $\mu_\eta = 1$. The variances used were $\sigma_{\mathcal{F}} = 0.1\sqrt{\text{SNR}}$, $\sigma_\eta = 0.1$. The random numbers associated with the signal are generated once for each n value while those associated with the noise are generated at each frequency. Both generators also produced a random phase. Thus we can generate n coherent plane waves of chosen amplitudes incident on a model array of microphones with fixed amplitude incoherent noise. Additional plane waves can be synthesized and included to model multiple coherent signals incident on an array of microphones. The array design used in generating the synthetic data is a 6 element array with geometry identical to that of the Brookhaven National Laboratory deployment.

The data from Hurricane Igor was chosen because it contains a strong microbarom signal and provides a real world example of the signal measured when a strong maritime storm is present in the open ocean. Hurricane Igor was the most intense storm of the 2010 Atlantic hurricane season.

Igor reached a maximum intensity of Category 4 with sustained winds of just under 70 $\frac{\mathrm{m}}{\mathrm{s}}$. The storm weakened to a Category 1 storm as it traveled eastward across the Atlantic but did not make landfall on the continental United States. Igor did strike the island of Bermuda as a Category 1 and continued to move northward through the Atlantic, maintaining its intensity. During the time that Igor was active, the Croatan and McCoy sites were recording with all four elements. One element in the Ocala array was not functioning and two sensors in the Francis Marion array were not functioning. All non-functioning elements were due to loss of power from insufficient solar exposure.

In this comparison of the beamforming methods discussed previously, we will consider how well each method's spatial spectra identifies the presence of one signal and a pair of signals incident on an array of microphones at various SNR values using the synthetic data. The data from Hurricane Igor will then be used to compare how the methods perform with actual data and compare the stability of solutions over large time samples associated with the prolonged microbarom energy produced by a large maritime storm.

Here we consider azimuth directions $-180^o \leq \phi \leq 180^o$ with increment 1^o, and acoustic trace velocities, v_{tr}, between 330 and 400 $\frac{\mathrm{m}}{\mathrm{s}}$. For the various beamforming methods, the spatial spectrum, $P(\phi, v_{\mathrm{tr}}, f)$, is calculated for all considered values and reduced to a function only of ϕ by taking the maximum value at constant azimuth, ϕ, and using the weighting vector,

$$P(\phi) = \sum_{k=1}^{K} \max_{v_{\mathrm{tr}}} \left[P(\phi, v_{\mathrm{tr}}, f_k)\, \varrho_k \right]. \tag{140}$$

The performance of the various spatial spectra can be analyzed using synthetic data incident on a model array. In this case, an array of eight elements in a five kilometer aperture are used to test synthesized continuous signal in the microbarom band, 0.15 - 0.3 Hz. The spatial spectra resulting from a single signal incident with SNR = 1, 2, and 4 are shown in the left column of Fig. 21. These panels show the response from each beamforming method for a single plane wave incident from 0 degrees. The Bartlett spatial spectrum varies very little with variations in noise level due to the side lobes present off the main beam. In the case of a single plane wave incident on the array, the Capon and MUSIC spatial spectra are equally efficient in identifying the peak. Even in the low SNR case, the DOA of a single signal is easily identified by all of the spatial spectra.

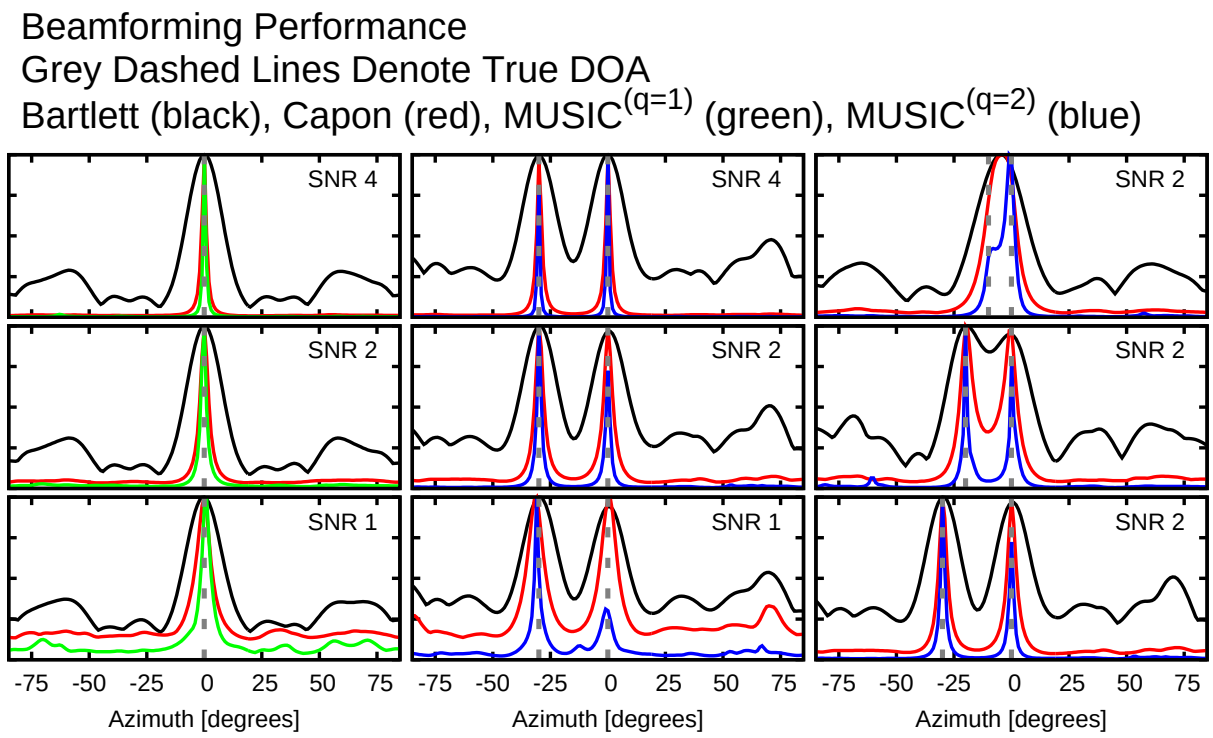

Fig. 21: The spatial spectrum response for one signal (left) and two signals (center, right) incident on an array of eight microphones in a five kilometer aperture array. In the left and center columns, the SNR decreases in the lower panels. In the right column, the sources source separation decreases with constant SNR.

In the case of two signals incident on an array, both the SNR and relative DOAs are factors in detection. The center column of Fig. 21 shows the results for two signals separated by 30 degrees at variable SNR. The Bartlett beam is able to resolve the two separate peaks in all cases, however again the side lobes complicate the spatial spectrum. The Capon spectrum reduces the side lobes, allowing the peaks to be easily identified in all cases, however the MUSIC spectra assuming $q = 2$ is able to better minimize the spatial spectra away from the true DOAs.

The spatial spectra response for two signals separated by 30^o, 20^o, and 10^o with constant SNR is shown in the right column of Fig. 21. All spatial spectra exhibit local maxima at the true DOAs when separated by 30^o (top), however, the Bartlett beam begins to have difficulty once the pair of arrivals are within 20^o of one another and cannot resolve the separate signals for small separations. The Capon spatial spectrum is able to reduce the side lobes, and more easily identify the signals when separated by 20^o, however it also fails to separate the signals at 10^o. Only the MUSIC ($q = 2$) is able to resolve the separate maxima for a separation of 10^o. Array geometry

contributes to the limiting resolution, however, in this case the relative performance of the different methods is of interest. It is evident from these results that the MUSIC algorithm out performs the Bartlett and Capon spatial spectra assuming that the correct value of q is known. A method to determine the number of signals present in a data record will be presented later in this chapter.

The data recorded on the Croatan and McCoy arrays during Hurricane Igor can be used to further compare the performance of the various beamforming methods. Once a window of data has been analyzed, it is straightforward to determine the largest local maximum. The large window can then be moved forward in the data record (possibly overlapping) resulting in a time series record of the azimuth of a continuous acoustic signal incident on an array. In the case of Hurricane Igor, microbaroms were present in the data from September 17 to September 22 of 2010. These five days of data have been processed using each type of spatial spectra and plotted using the difference between the azimuth of the microbarom signal and the azimuth from the array to the storm eye. The results of this processing are shown in Fig. 22 and 23. The horizontal axis denotes the time as the storm moved through the Atlantic and the vertical shows the relative azimuth of the signals detected relative to the azimuth to the eye. Positive azimuths indicate signal emanating from north of the storm while negative azimuths indicate signal emanating from south of the storm. The large dot on the horizontal axis denotes the time at which the hurricane passed the latitude of the array. Before that time, the storm was south of the array and the microbarom signal propagated through the storm wind field, while after that time the storm was north of the array and the microbarom signal was relatively unaffected by the storm winds.

In each case, the microbarom signal is overwhelmed by noise in the daytime hours due to increased wind and atmospheric turbulence. During the overnight hours, the signal is easily detected and analyzed. In the nighttime hours between 00:00 and 12:00 GMT on September 19th, both the Croatan and McCoy arrays detected microbaroms with azimuths north of the storm. As the storm passed each array latitude, the spread of the azimuths decreased and a low variance azimuth shifted to a location south of the storm and stabilized there. This stabilized azimuth is easily seen the results for the Bartlett, Capon, and $q = 1$ MUSIC spatial spectra. For the data recorded before the storm passed the array latitude, the microbarom propagated through the storm winds and the $q = 2$ MUSIC spatial spectra was able to locate multiple signals frequently.

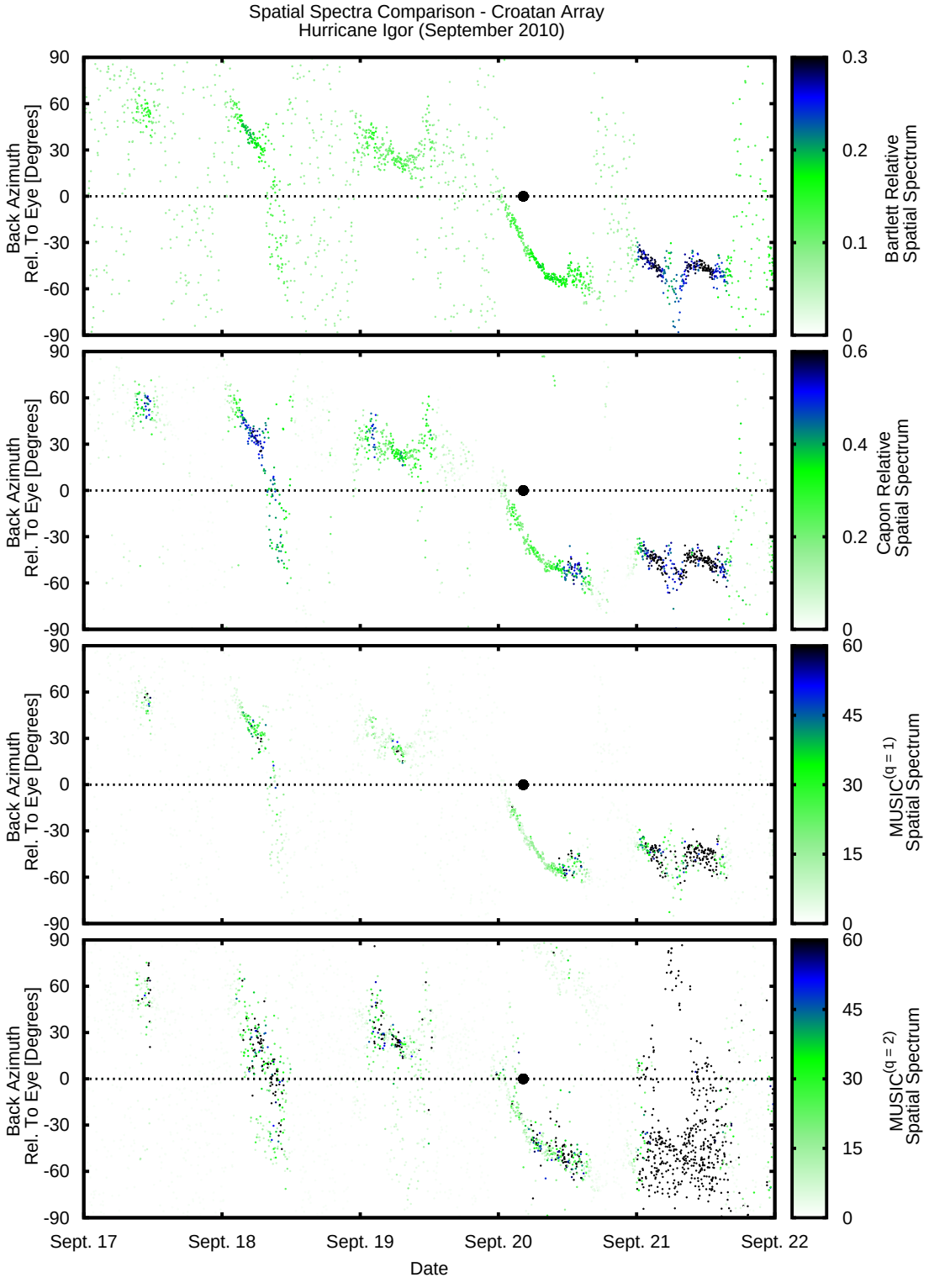

Fig. 22: The maximum of the spatial spectral function applied to data from the Croatan array during Hurricane Igor (September 2010).

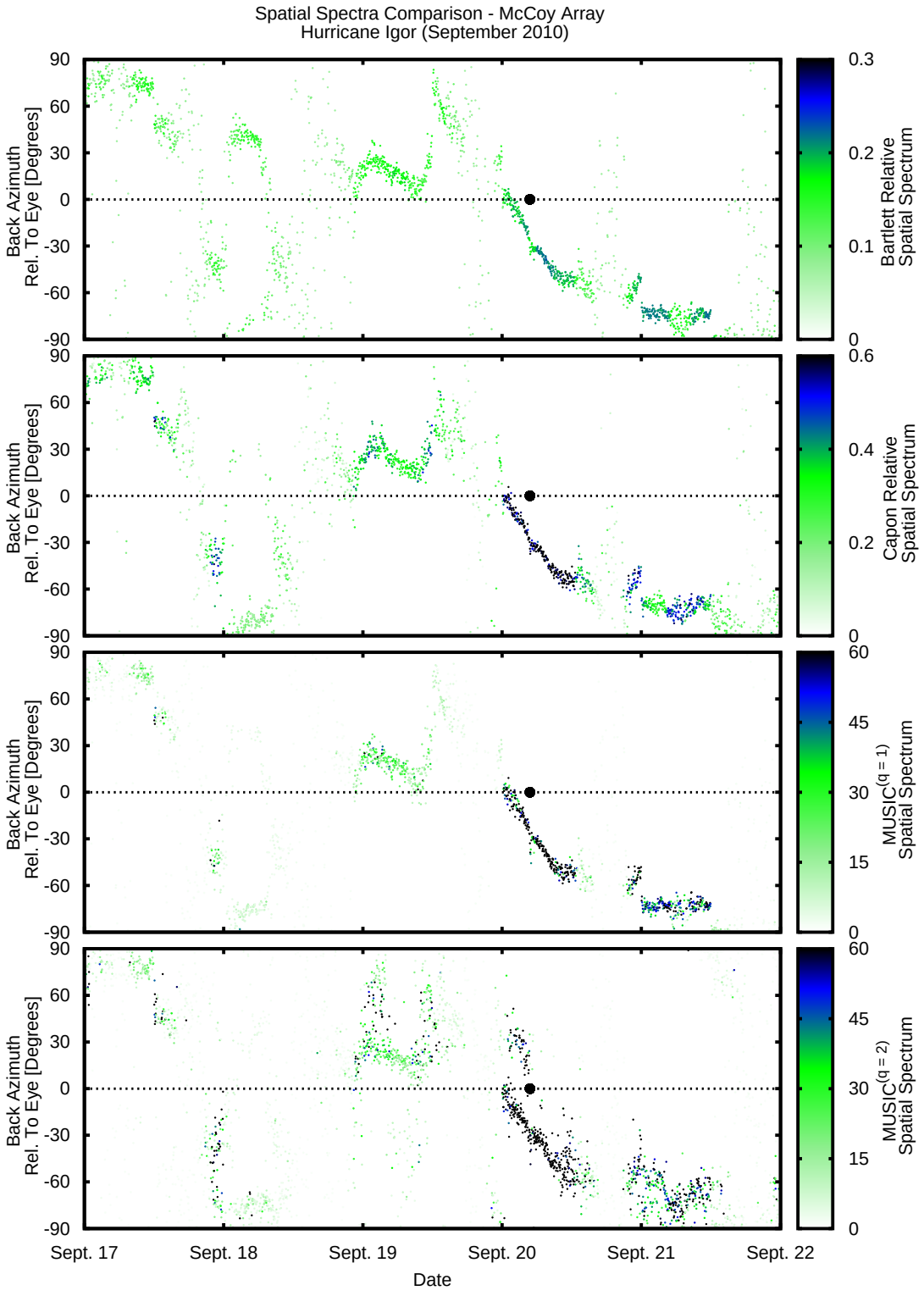

Fig. 23: The maximum of the spatial spectral function applied to data from the McCoy array during Hurricane Igor (September 2010).

Residual and Model Selection

From the analysis the beamforming performance, it is clear that the MUSIC spatial spectrum (or alternately the DMR beamformer) is more efficient than the Bartlett or Capon methods for extracting one or possibly several microbarom signals from a noisy data record. However, both MUSIC and DMR beamforming require a decision be made regarding the number of signals present. In this section we finalize the data processing routine to be used by developing and implementing a model selection criterion. In a general sense, the problem we approach can be summarized as follows: a data record is being analyzed which can be explained by a number of possible models. A null hypothesis exists which asserts that no coherent energy is present (q = 0). Alternately, one or more coherent plane waves could be present in the data, to a maximum of $p-1$. Thus, for an array of p microphones, there exist p possible models to explain the data, $q = 0, 1, \ldots p-1$.

Model selection is a statistical process which is based on a well-justified criteria of choosing the "best" model to explain a finite amount of noisy data. Model selection criterion should be a quantity calculable from the result of each model applied to the data and fit into a general statistical framework of a likelihood or Bayesian framework of statistics [72]. Such a criterion first relies on a quantification of information such as that developed by Kullback and Leibler in a 1951 publication. Let $\mathcal{T}(\mathcal{X})$ denote full reality or truth from a given state, $\mathcal{X}$, and $\mathcal{M}(\mathcal{X}, \mathcal{Q})$ denote an approximating model with parameters $\mathcal{Q}$. The truth varies only over the variable $\mathcal{X}$ while the model varies over $\mathcal{X}$ and a space of different models defined by $\mathcal{Q}$. The Kullback-Leibler information, $I(\mathcal{T}, \mathcal{M})$, is the information lost when the model $\mathcal{M}$ is used to approximate $\mathcal{T}$ [73],

$$I(\mathcal{T}, \mathcal{M}) = \int \mathcal{T}(\mathcal{X}) \ln\left(\frac{\mathcal{T}(\mathcal{X})}{\mathcal{M}(\mathcal{X}, \mathcal{Q})}\right) d\mathcal{X}. \tag{141}$$

The best model is then defined by that which minimizes the information lost relative to all possible models.

This information criterion cannot be used directly because it requires knowledge of the true

system, $\mathcal{T}(\mathcal{X})$. However, note that K-L information can be expressed in the alternate form,

$$\begin{aligned} I(\mathcal{T},\mathcal{M}) &= \int \mathcal{T}(\mathcal{X}) \ln\left(\frac{\mathcal{T}(\mathcal{X})}{\mathcal{M}(\mathcal{X},\mathcal{Q})}\right) d\mathcal{X} \\ &= \int \mathcal{T}(\mathcal{X}) \ln \mathcal{T}(\mathcal{X})\, d\mathcal{X} - \int \mathcal{T}(\mathcal{X}) \ln \mathcal{M}(\mathcal{X},\mathcal{Q})\, d\mathcal{X} \\ &= E_{\mathcal{T}}\left[\ln \mathcal{T}(\mathcal{X})\right] - E_{\mathcal{T}}\left[\ln \mathcal{M}(\mathcal{X},\mathcal{Q})\right]. \end{aligned}$$

where we've denoted the expectation of a quantity $\int \mathcal{T}(\mathcal{X})\, A\, d\mathcal{X} = E_{\mathcal{T}}[A]$. The first term in this new form is a constant, we'll denote it by $C_{\mathcal{T}}$, and so finally,

$$I(\mathcal{T},\mathcal{M}) = C_{\mathcal{T}} - E_{\mathcal{T}}\left[\ln \mathcal{M}(\mathcal{X},\mathcal{Q})\right]. \tag{142}$$

This produces an information criterion measure which can be compared for different values of $\mathcal{Q}$ without requiring knowledge of the truth.

A rigorous model selection criterion based on K-L information was introduced by Akaike [74]. The basis of the problem reduced to estimating

$$E_{\tilde{\mathcal{X}}} E_{\mathcal{X}}\left[\ln \mathcal{M}\left(\mathcal{X}|\hat{\mathcal{Q}}\left(\tilde{\mathcal{X}}\right)\right)\right],$$

where $E_{\mathcal{X}}\left[\ln \mathcal{M}\left(\mathcal{X}|\hat{\mathcal{Q}}\left(\tilde{\mathcal{X}}\right)\right)\right] = E_{\mathcal{T}}\left[\ln \mathcal{M}\left(\mathcal{X}|\hat{\mathcal{Q}}\right)\right]$ with $\hat{\mathcal{Q}}$ being the maximum likelihood estimator of $\mathcal{Q}$ based on the model $\mathcal{M}$ and data $\tilde{\mathcal{X}}$. Akaike demonstrated that the maximized log-likelihood value was a biased estimate of $E_{\tilde{\mathcal{X}}} E_{\mathcal{X}}\left[\ln \mathcal{M}\left(\mathcal{X}|\hat{\mathcal{Q}}\left(\tilde{\mathcal{X}}\right)\right)\right]$, but the bias was proportional to $\mathcal{K}$, the number of estimable parameters in the model [74]. Therefore, an approximately unbiased estimator in the case of large sample sizes and "good" models is

$$\ln\left(\mathcal{L}\left(\hat{\mathcal{Q}}|\tilde{\mathcal{X}}\right)\right) - \mathcal{K} = C_{\mathcal{T}} - \hat{E}_{\hat{\mathcal{Q}}}\left[I\left(\mathcal{T},\hat{\mathcal{M}}\right)\right],$$

where $\hat{\mathcal{M}} = \mathcal{M}\left(\cdot|\hat{\mathcal{Q}}\right)$. Akaike took this result and scaled it by -2, producing the Akaike Information Criterion [74],

$$\mathrm{AIC} = -2\ln\left(\mathcal{L}\left(\hat{\mathcal{Q}}|\tilde{\mathcal{X}}\right)\right) + 2\mathcal{K}. \tag{143}$$

In the case of a least squares estimation, the AIC can be expressed alternately as

$$\mathrm{AIC} = \mathcal{N} \ln\left(\frac{\mathrm{RSS}}{\mathcal{N}}\right) + 2\mathcal{K}, \tag{144}$$

where $\mathcal{N}$ is the number of independent measurements used in the model selection process. In the case that $\mathcal{K}$ is large relative to $\mathcal{N}$ (or $\mathcal{N}$ is small for any $\mathcal{K}$), there is a second order bias correction which must be used to correct for a finite sample size. The corrected AIC was derived by Sugiura, Hurvich, and Tsai [75, 76],

$$\begin{aligned} \mathrm{AICc} &= \mathcal{N} \ln\left(\frac{\mathrm{RSS}}{\mathcal{N}}\right) + 2\mathcal{K} + \frac{2\mathcal{K}\left(\mathcal{K}+1\right)}{\mathcal{N}-\left(\mathcal{K}+1\right)} \\ &= \mathcal{N} \ln\left(\frac{\mathrm{RSS}}{\mathcal{N}}\right) + \frac{2\mathcal{K}\mathcal{N}}{\mathcal{N}-\left(\mathcal{K}+1\right)}. \end{aligned} \tag{145}$$

Thus, in order to select the model which best explains the data, we require the number of independent measurements, $\mathcal{N}$, the number of parameters in each model, $\mathcal{K}$, and the residual sum of squares, RSS, for each possible model. The model which minimizes the AICc is then the one which best explains the information contained in the data.

The application of the AICc can be separated into a number of steps. Initially, the null hypothesis produces an AICc value,

$$\mathrm{AICc}\left(0\right) = \mathcal{N} \ln\left(\frac{1}{\mathcal{N}}\right). \tag{146}$$

Then, taking the peak of the MUSIC or DMR spatial spectrum for $q = 1$, the residual for 1 plane wave is found, $0 \leq \mathrm{RSS}_1 < 1$, which provides some decrease in the logarithmic term. However, a penalty is produced by $\mathcal{K}_1$. Thus, a single plane wave is a "better" model for the data if,

$$\begin{aligned} \mathrm{AICc}(1) &< \mathrm{AICc}(0) \\ \mathcal{N} \ln\left(\frac{\mathrm{RSS}_1}{\mathcal{N}}\right) + \frac{2\mathcal{K}_1\mathcal{N}}{\mathcal{N}-\left(\mathcal{K}_1+1\right)} &< \mathcal{N} \ln\left(\frac{1}{\mathcal{N}}\right) \\ \frac{2\mathcal{K}_1}{\mathcal{N}-\left(\mathcal{K}_1+1\right)} &< \ln\left(\frac{1}{\mathrm{RSS}_1}\right). \end{aligned} \tag{147}$$

A similar expression can be derived to relate the AICc values for q and $q+1$. The resulting condition

states that the penalty for additional parameters required in a more complicated model must provide a sufficiently large decrease in the residual sum of squares to be accepted as a "better" model. In general, the more measurements used in the analysis, the easier it is to satisfy this condition, while a large number of parameters requires a larger reduction in the residual to allow the more complicated model.

The number of parameters associated with each model can be determined by referencing the set up of our problem in Eq. (124). For each plane wave incident on the array, only its overall amplitude $|\mathcal{F}(f)|^2$ was free in the beamforming derivation. This provides K free parameters for each plane wave in the model. Additionally, each plane wave was defined by a two component slowness vector $\vec{w}$. However, in each beamforming development, the length of $\vec{\Phi}$ was fixed by some condition. This constraint eliminates one free parameter. Therefore, a model with q plane waves contains $\mathcal{K} = (K + 2 - 1)\, q = (K + 1)\, q$ free parameters.

The residual sum of squares for a given number of signals can be found by using Eq. (117) with (119) with the slowness vector(s) defined by the q largest peaks in the spatial spectrum. Assuming that $\vec{\eta}(f) \ll \mathcal{F}(f)\, \Phi(\vec{w}, f)$, the spectral content of the coherent signal(s) incident on the array can be calculated with the pseudo-inverse of $\vec{\Phi}$,

$$\hat{\vec{\mathcal{F}}}(f) = \left(\boldsymbol{\Phi}^{\dagger}(\boldsymbol{w}, f)\boldsymbol{\Phi}(\boldsymbol{w}, f)\right)^{-1} \boldsymbol{\Phi}(\boldsymbol{w}, f)\tilde{\vec{X}}(f), \tag{148}$$

$$\boldsymbol{\Phi}(\boldsymbol{w}, f) = \left(\vec{\Phi}_1(\vec{w}_1, f) \quad \vec{\Phi}_2(\vec{w}_2, f) \quad \cdots \quad \vec{\Phi}_q(\vec{w}_q, f)\right).$$

This can be combined with the modeled signal to define a projection operator for the residual,

$$\begin{aligned}
\hat{\vec{\eta}}(\boldsymbol{w}, f) &= \tilde{\vec{X}}(f) - \boldsymbol{\Phi}(\boldsymbol{w}, f)\left(\boldsymbol{\Phi}^{\dagger}(\boldsymbol{w}, f)\boldsymbol{\Phi}(\boldsymbol{w}, f)\right)^{-1} \boldsymbol{\Phi}(\boldsymbol{w}, f)\tilde{\vec{X}}(f) \\
&= \left[\boldsymbol{I} - \boldsymbol{\Phi}(\boldsymbol{w}, f)\left(\boldsymbol{\Phi}^{\dagger}(\boldsymbol{w}, f)\boldsymbol{\Phi}(\boldsymbol{w}, f)\right)^{-1} \boldsymbol{\Phi}(\boldsymbol{w}, f)\right] \tilde{\vec{X}}(f) \\
&= \left[\boldsymbol{I} - \hat{\boldsymbol{\Pi}}_{\text{sig}}(\boldsymbol{w}, f)\right] \tilde{\vec{X}}(f) = \hat{\boldsymbol{\Pi}}_{\eta}(\boldsymbol{w}, f)\, \tilde{\vec{X}}(f).
\end{aligned} \tag{149}$$

The residual spectral density can then be written,

$$\begin{aligned}
\boldsymbol{S}_{\eta}(f) &= \left\langle \hat{\vec{\eta}}(\boldsymbol{w}, f) \otimes \hat{\vec{\eta}}^{\dagger}(\boldsymbol{w}, f) \right\rangle \\
&= \left\langle \hat{\boldsymbol{\Pi}}_{\eta}(\boldsymbol{w}, f) \tilde{\vec{X}}(f) \otimes \left[\hat{\boldsymbol{\Pi}}_{\eta}(\boldsymbol{w}, f) \tilde{\vec{X}}(f) \right]^{\dagger} \right\rangle \\
&= \hat{\boldsymbol{\Pi}}_{\eta}(\boldsymbol{w}, f) \left\langle \tilde{\vec{X}}(f) \otimes \tilde{\vec{X}}^{\dagger}(f) \right\rangle \hat{\boldsymbol{\Pi}}_{\eta}^{\dagger}(\boldsymbol{w}, f) \\
&= \hat{\boldsymbol{\Pi}}_{\eta}(\boldsymbol{w}, f) \hat{\boldsymbol{S}}(f) \hat{\boldsymbol{\Pi}}_{\eta}^{\dagger}(\boldsymbol{w}, f).
\end{aligned} \tag{150}$$

And so finally, the residual can be calculated by comparing the trace of the original spectral density matrix to the trace of the residual,

$$\mathrm{RSS} = \sum_{j=1}^{K} \frac{\mathrm{Tr}\left[\hat{\boldsymbol{S}}_{\eta}(f_j) \right]}{\mathrm{Tr}\left[\hat{\boldsymbol{S}}(f_j) \right]} \varrho_k. \tag{151}$$

It should be noted that this normalizes the RSS values so that in the case of $q = 0$, one has RSS $= 1$.

In our application, the number of measurements used to select a model is $2pK$ since there is a real and imaginary component of $X_j(f)$ at each sensor and at each frequency used in broadband analysis. A problem arises at this point because not all of the measurements are independent. Spectral leakage and time correlations in the noise reduce the independence of the measurements. In order to demonstrate this problem, consider the 12 hours of data displayed in Fig 24. In the left side of the figure are the largest maxima of the MUSIC spatial spectra assuming $q = 1$ and $q = 2$. Over the course of the data record, a consistent coherent signal is present at around 0^o. There are occasional times during which a weak second signal is present from around 100^o and a short period between hours three and four where a second signal is present between -60^o and -90^o.

On the right are the full spatial spectra for a few specific times within the overall record. Early in the data record, at 00:27, there is evidently only a single signal since the $q = 2$ spectra doesn't contain a second peak which can be distinguished from the incoherent noise. Later, at 03:50, the $q = 1$ spatial spectra actually pick up several instances of strong coherent energy from around -75^o which is consistent with the $q = 2$ spectra and therefore during these times it is reasonable to assume a strong second coherent signal is present. Later still in the record, at 07:47, the signal

incident around 0^o is seen to split into a pair of coincident signals separated by approximately 20 degrees.

In the upper panel of Fig. 25 is the residual calculated using the projection result in Eq. (151) for $q = 0$, $q = 1$, and $q = 2$. In the lower panels of the figure is the AICc values assuming all of the measurements are independent, 90% are independent, and 80% are independent. In the case that all measurements are assumed completely independent, the AICc selects the $q = 2$ result for nearly the entire data record, which the results in Fig. 24 clearly indicate to be an incorrect model selection for much of the data record. By assuming some of the measurements are dependent on one another, we can scale the value of $N = 2pK$ and by doing so produce the modified AICc results in the lower panels of the figure in which the model selection is more applicable to the data record.

In order to account for these losses, we have introduced a multi-frequency spectral density matrix, which we elect to term the "super spectral density matrix". Within each snapshot of data, we stack the vectors of data from f_1 to f_K and then average over multiple snapshots to produce a matrix of the form,

$$\tilde{\vec{X}}_{\boldsymbol{\mathcal{S}}} = \begin{pmatrix} \tilde{\vec{X}}\left(f_1\right) \\ \tilde{\vec{X}}\left(f_2\right) \\ \cdots \\ \tilde{\vec{X}}\left(f_K\right) \end{pmatrix} \quad \longrightarrow \quad \hat{\boldsymbol{\mathcal{S}}} = \left\langle \tilde{\vec{X}}_{\boldsymbol{\mathcal{S}}} \otimes \tilde{\vec{X}}^{\dagger}_{\boldsymbol{\mathcal{S}}} \right\rangle . \tag{152}$$

As an alternate visualization of this matrix, consider defining the spectral density matrix for mul-

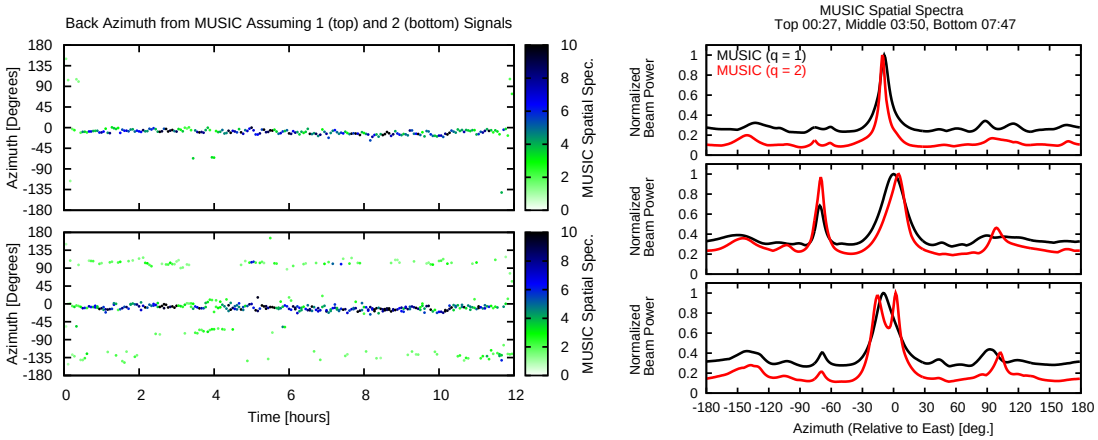

Fig. 24: Data from Brookhaven National Laboratory during Hurricane Ophelia likely contains multiple coherent signals at certain time intervals and can be used to demonstrate the overestimate of the number of independent measurements used in the AICc calculation.

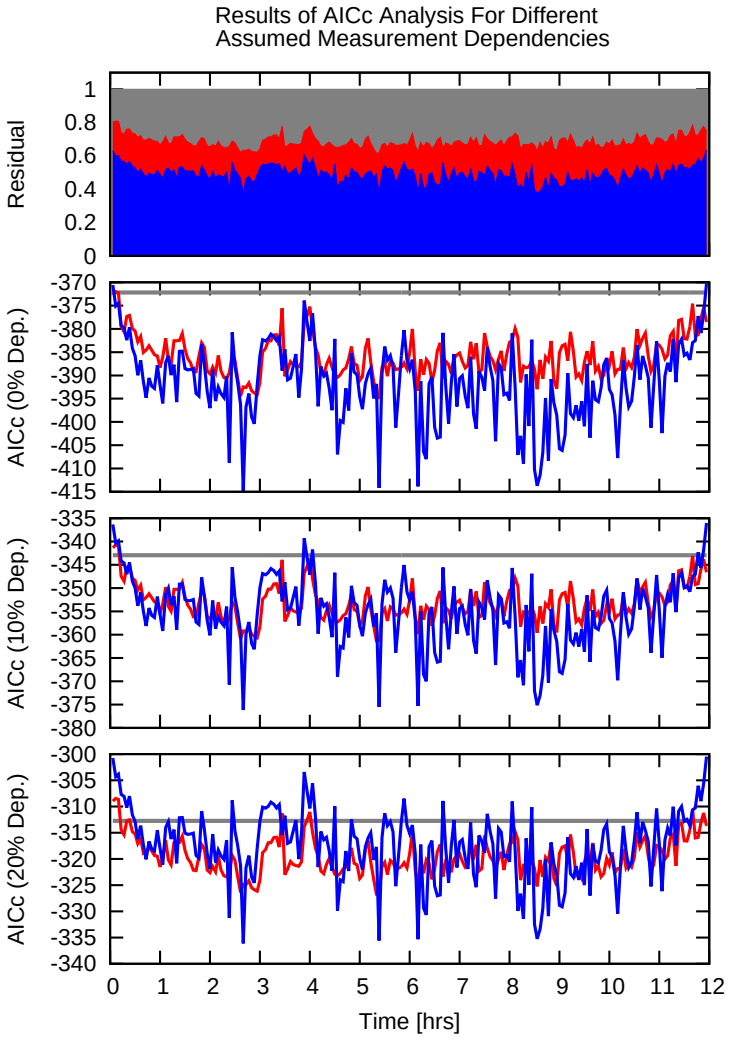

Fig. 25: The residual calculated using the larges peak and largest 2 peaks in the $q = 1$ and $q = 2$ MUSIC spatial spectra respectively are shown in the upper panel of the figure with the blue area being the residual for $q = 2$, the red area above that being the additional residual for $q = 1$. In the lower panels, the AICc result for $q = 0$ (gray), $q = 1$ (red), and $q = 2$ (blue) are shown for various assumptions of what fraction of the measurements are dependent.

tiple frequencies,

$$\hat{\boldsymbol{S}}\left(f_n, f_m\right) = \left\langle \tilde{\vec{X}}\left(f_n\right) \otimes \tilde{\vec{X}}^{\dagger}\left(f_m\right) \right\rangle,$$

then the super spectral density matrix is defined by sub-matrices,

$$\boldsymbol{\mathcal{S}} = \begin{pmatrix} \hat{\boldsymbol{S}}\left(f_1, f_1\right) & \hat{\boldsymbol{S}}\left(f_1, f_2\right) & \dots & \hat{\boldsymbol{S}}\left(f_1, f_K\right) \\ \hat{\boldsymbol{S}}\left(f_2, f_1\right) & \hat{\boldsymbol{S}}\left(f_2, f_2\right) & & \vdots \\ \vdots & & \ddots & \\ \hat{\boldsymbol{S}}\left(f_K, f_1\right) & \dots & & \hat{\boldsymbol{S}}\left(f_K, f_K\right) \end{pmatrix}.$$

A number of characteristics of the data can be obtained from the super spectral density matrix. If one sets all off-diagonal blocks to zero, and substitutes the resulting matrix into the pure state filter in Eq. (107), one finds a measure of only the spatial coherence at all frequencies being used in the calculation. Such spatial coherence is assumed to be the result of a coherent acoustic signal propagating across the array. In order to obtain a measure of the spectral leakage, one sets the off-diagonals within each sub-matrix to zero resulting in a matrix of the form,

$$\boldsymbol{\mathcal{S}}_{\text{spec}} = \begin{pmatrix} S_{11}\left(f_1, f_1\right) & 0 & \dots & S_{11}\left(f_1, f_2\right) & 0 & \dots \\ 0 & S_{22}\left(f_1, f_1\right) & \dots & 0 & S_{22}\left(f_1, f_2\right) & \\ \vdots & \vdots & \ddots & & & \ddots \\ S_{11}\left(f_2, f_1\right) & 0 & & & & \\ 0 & S_{22}\left(f_2, f_1\right) & & & & \\ \vdots & & \ddots & & & \end{pmatrix}. \tag{153}$$

Substituting this matrix into the pure state filter in Eq. (107) results in a measure of how much independence is lost due to spectral leakage. One can therefore approximate the number of independent measurements by $\mathcal{N}' = 2pK\left(1 - \gamma_{(\text{filter})}\left[\boldsymbol{\mathcal{S}}_{\text{spec}}\right]\right)$.

Preliminary work using the data recorded at BNL has produced value of $\gamma_{(\text{filter})}\left[\boldsymbol{\mathcal{S}}_{\text{spec}}\right]$ which greatly improve the accuracy of the AICc model selection method. However, additional complications arise due to the need for this large matrix to be full rank which requires a large number of snapshots to provide sufficient statistics of the dependence of the data. Additional work is necessary to further investigate the information contained in the super spectral density matrix and determine if it is a useful quantity to use in the statistics of array processing. Regrettably, the

additional data collection and time necessary to perform such an investigation is beyond the scope of this project and will need to be done at a later time.

The introduction of the super spectral density matrix, Eq. (152), leads to a new concern in our scheme of arranging snapshots within a larger time window. The super spectral density matrix is $pK \times pK$ and therefore we have increased the number of independent snapshots necessary to construct a statistically accurate matrix by a factor of K. In order to assure ourselves that the super spectral density matrix computed by snap shot averaging is full rank, we require at least $(p+1)K$ independent windows be included in our calculation. For a frequency band Δf and data sampled with time steps dt, $K = \Delta f \times N dt$. Accounting for the zero-padding of data, the snapshot window is of length $T_{\text{snap}} = \frac{N}{2} dt$. Combining this,

$$\begin{aligned} \frac{T_{\text{window}}}{T_{\text{snap}}} &\geq (p+1)\, \Delta f\, N dt \\ &\geq (p+1)\, \Delta f\, 2 T_{\text{snap}}. \end{aligned} \tag{154}$$

Thus we require,

$$T_{\text{window}} \geq 2\,(p+1)\, \Delta f\, T_{\text{snap}}^2, \tag{155}$$

which can produce feasibility issues when p or Δf are large.

Summary and Evaluation of An Optimized Routine

All aspects of the proposed data processing routine have been discussed and here we provide a summary of the method. Following the description of the routine is a short explanation of post processing methods which are useful for characterizing the detection.

1. A large window of data is selected for analysis. The length of this window is determined by Eq. (155). Within this window, overlapping snapshots of data are Fourier transformed to produce an averaged power spectral density matrix, $\hat{\boldsymbol{S}}(f)$, by Eq. (136) and an averaged super spectral density matrix $\boldsymbol{\mathcal{S}}$ by Eq. (152).

2. Various operators are performed using the power spectral density matrix and super spectral density matrix.

    - The power spectral density matrix at each frequency to be included in analysis is used

in the pure state filter, Eq. (107), to weight each frequency by the coherence of the data in that bin.

- The power spectral density matrix at each frequency to be used is expanded into an eigenvector decomposition as in Eq. (120).
- The super spectral density matrix is modified to include only spectral coherence as in Eq. (153) and plugged into the pure state filter to determine the fraction of the measured data which is independent. From this result the AICc (0) is computed using Eq. (146).

3. The MUSIC or DMR spatial spectrum is calculated for $q = 1$ using the eigenvalues and eigenvectors of $\hat{\boldsymbol{S}}(f)$.

   - The peak of the spatial spectrum is found and used to construct the projection operator in Eq. (149).
   - The residual RSS_1 is calculated and used to calculate AICc(1).

4. If AICc(0) $<$ AICc(1), the routine exits and reports that there is no signal present. Otherwise it calculates the MUSIC or DMR spatial spectrum for the subsequent value of q.

   - The largest q peaks of the spatial spectrum are determined, the projection operator in Eq. (149) is calculated, and RSS_q is determined.
   - AICc(q) is checked against AICc($q-1$) to determine if a minimum value of AICc has been found.
   - These steps are looped over until a minimum AICc value is found or the limiting number of signals is reached.

5. The large window is moved forward by some fraction of its duration and the subsequent data is analyzed. This is repeated until the end of the data file is reached.

Once a model is chosen by the AICc criterion, several characteristics of the result can be calculated and used to characterize the detection. The discrete second derivative at the local maximum associated with a signal can be used to fit a quadratic and window the peak in the spatial spectrum. Once this is completed, the mean, μ_P, and standard deviation, σ_P, of the off-beam data can be computed. An example of this analysis is shown in Fig. 26. From the form of the expression

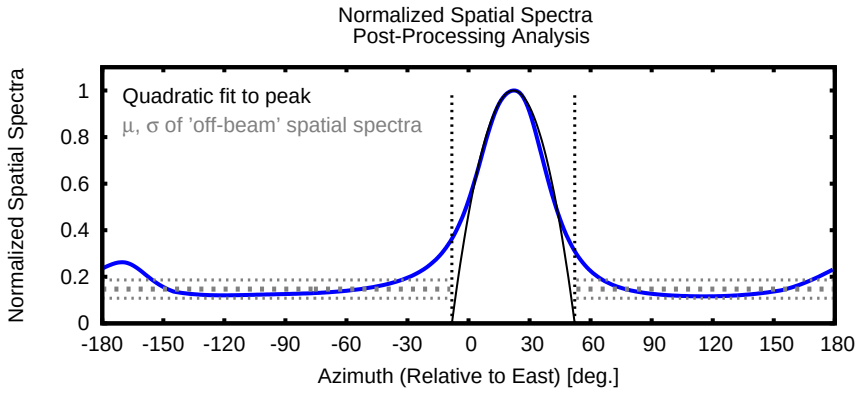

Fig. 26: The zeros of a quadratic fit (black solid line) can be used to identify the portions of the spectrum which are "off-beam". In this region, the mean, μ, and standard deviation, σ are calculated in order to characterize the result.

in Eq. (134), it is evident that the spatial spectrum in the vicinity of a maximum associated with a signal can be expressed as a scaled Cauchy-Lorenz distribution,

$$P(\phi)\Big|_{\phi_0} \sim \mu_P + \frac{P(\phi_0) - \mu_P}{1 + \frac{(\phi-\phi_0)^2}{\delta\phi^2}}. \tag{156}$$

Using μ_P, σ_P, and this fit, the confidence and width of each spatial spectral maximum can be calculated by,

$$\text{Confidence} = \frac{P(\phi_{\max}) - \mu_P}{\sigma_P}, \tag{157a}$$

$$\text{Beam Half-Width} = \phi_{\frac{1}{2}} = 2\sqrt{-2\frac{P(\phi_0)}{P''(\phi_0)}}. \tag{157b}$$

The first of these quantities measures the maximum in terms of standard deviations above the off-beam mean. The second measures the half-width of the maximum relative to the off-beam mean and is derived by the condition

$$\mu_P + \frac{P(\phi_0) - \mu_P}{1 + \frac{\left(\phi_{\frac{1}{2}} - \phi_0\right)^2}{\Delta\phi^2}} = \mu_P + \frac{P(\phi_0) - \mu_P}{2}, \tag{158}$$

where it can be shown from the fit that $\Delta\phi = \sqrt{-2\frac{P(\phi_0)-\mu_P}{P''(\phi_0)}}$.

It should also be noted that the processing routine discussed here can be implemented as

part of a broader method. Consider the case that a low SNR transient is present in data with a moderately strong microbarom signal (or other continuous coherent background). The routine here can be used to construct the projection operator in Eq. (149), which can then be used to remove the continuous background signal from the data. The projection operator, $\mathbf{\Pi}_{\eta}(\boldsymbol{w}, f)$, acting on a snapshot of data $\tilde{\vec{X}}(f)$, removes all coherent information along the beam(s) defined by $\boldsymbol{w}$; in effect spatially filtering the data to remove coherent signals only along the beam(s). The resulting snap shot of data can then be analyzed using any other method to identify remaining transients.

Limited Data Sources - A Processing Method for Sparse Arrays

From the results of the analysis of the previous section, it is evident that in the case of the small arrays used in the experiment by the NCPA infrasound group, the data is insufficient to use the MUSIC/AICc algorithm. As an alternate to the method proposed above, it has been chosen here to use steps 1 and 2 from the previous section's method to extract the approximate spectral density matrix $\hat{\boldsymbol{\mathcal{S}}}(f)$ and use it to determine weighting of frequency bins as in the first part of step 2 from the method summary. Instead of using the MUSIC spatial spectrum, the inverse $\hat{\boldsymbol{\mathcal{S}}}^{-1}(f)$ at each frequency of interest is computed and the frequency weighted Capon beamformer is used to produce a spatial spectrum for the data. From this result, the largest local maximum indicating signal incident from east of the array (that is, from the Atlantic) is chosen and the beamwidth is calculated as in Eq. (157b) using the second derivative and local maximum from the Capon beam. This extracts only the largest local maximum in the direction of interest and neglects any secondary sources which might contribute to the sound field at the array.

Optimizing Array Design

The arrays deployed during the 2010 and 2011 Atlantic hurricane seasons have been found to be incapable of resolving the nearly coincident arrivals predicted by the propagation models in Chapter 3. From the separation of arrival geometry in Fig. 9 and 14, we can infer that future deployments should be designed such that the arrays are capable of resolving incident signals separated by as little as 10 degrees and with differences in intensity of over 10 dB. In this section, we use the Capon beamforming methods to test the response of various array geometries including those used in the current analysis and several denser array layouts to determine the sensor count

and array footprint necessary to resolve the arrivals predicted by the propagation models.

In all the examples here, 15 60-second synthetic data records are generated to produce the equivalent of sampling a 15 minute data file using 15 subwindows. Using 15 snapshots to create the spectral density matrix guarantees that the sensor to snapshot ratio is always less than unity. While some processing methods allow a sensor to snapshot ratio of greater than unity, here we have required that the sensor to snapshot ratio be less than that value. In the event that the sensor to snapshort ratio is greater than unity, the spectral density matrix becomes rank deficient and the inversion in the Capon beamforming calculation fails.

Centered Triangular Array

The 4 element centered triangular arrays used for the majority of deployments in this project have provided useful data for identifying the microbarom source region once the signal is no longer interacting with the storm winds. However, the limited resolution of such a sparse array prevents one from being able to identify multiple signals in a data record without exceptionally large differences in incident angle. Shown in Fig. 27 is the spatial spectrum response for a pair of signals differing by 10 dB and incident from 0^o and -25^o relative to east. The signal to noise ratio (SNR) between the stronger signal and the background noise in this example is 4. It is immediately evident from this result the reason that our current data set has been unable to resolve the multi-pathing predicted by the model. Even in this high signal to noise ratio case, the only indication of the second signal is the asymmetry in the peak due to the stronger signal.

The Brookhaven National Laboratory Array

The 6 element array deployed at Brookhaven National Laboratory has performed markedly better than the four element centered triangular arrays deployed elsewhere during this project.

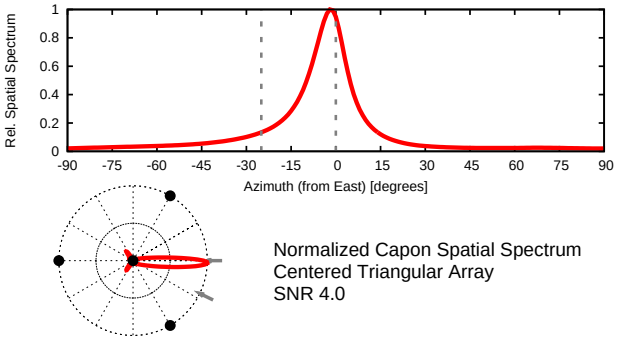

Fig. 27: The spectral response of a four element centered triangular array to a pair of infrasonic signals with 10 dB difference incident from 0^o and -25^o degrees.

The Brookhaven array has a longitudinal aperture of 4 km and latitudinal aperture of 1.8 km. The array is arranged such that it can be used as a pair of three element sub-arrays on the east and west side of the laboratory property, however, as mentioned in the analysis of the 4 element arrays, the resolving power of such sparse arrays is lower than that of the total array. Fig. 28 shows the resolving power of the existing 6 element array and a modified array of 8 elements in which a new central element and south-eastern element have been added.

Compared with the results in Fig. 27, it is clear that the increase in resolving power from a 4 element design to a 6 element design is significant. At a signal to noise ratio of 2, the expanded array is able to identify the weaker signal if it is separated by 15^o. The existing array is able to identify the second signal if the SNR increases to 4. If the separation decreases to 10^o, the expanded array is nearly able to resolve the two signals at an SNR of 8 while the existing array is unable to identify the second peak since there is no clear local maximum. The two additional sensors included in this analysis are shown in Fig. 29. In addition to the overall noise reducing that the added element provide, by decreasing the average inter-element spacing, the resolving power of the array is increased.

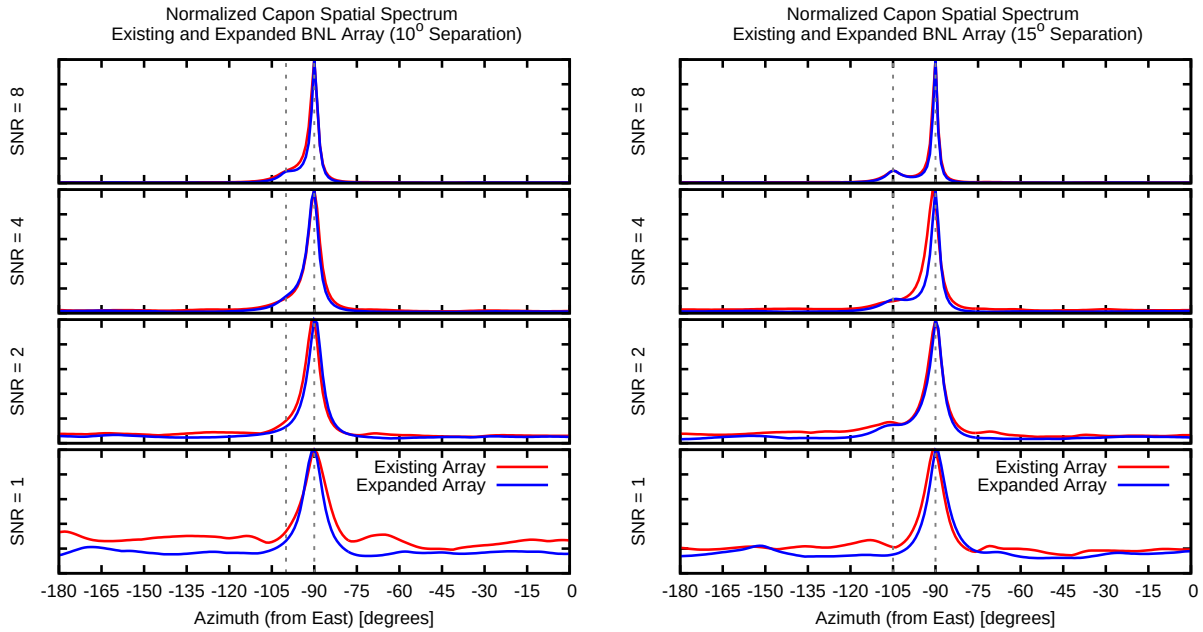

Fig. 28: The spectral response of the existing array at Brookhaven National Laboratory as well as the response of the array if two additional sensors are installed.

Fig. 29: The existing array at Brookhaven National Lab (yellow markers) and the proposed additional elements to improve performance (red markers).

Omni-Directional Array

In order to determine the limiting array characteristics for microbarom monitoring, one must ensure that the array has appropriate aperture and inter-element spacing to resolve signals from any azimuth. While it might be useful to design an array such that the sensitivity is non-uniform, it is more beneficial to be able to detect infrasonic energy incident from any azimuth in order to possibly track multiple targets accurately. Thus, we seek to produce an array design which has uniform resolving power in all directions and is capable of resolving multiple continuous signals in the microbarom band with the differences in azimuth and amplitude mentions previously. The microbarom band is assumed to be from 0.15 to 0.3 Hz. The wavelength of such signals at the ground (assuming a propagation speed of 350 $\frac{\text{m}}{\text{s}}$), range from 1.17 to 2.3 km. The nearest-neighbor inter-element spacing in the array should be approximately a half wavelength, which is 0.59 to 1.15 kilometers. Thus, as the number of elements increases in the array design, the overall aperture should increase as well. It should also be noted that exact replication of any specific array geometry is not required. It has been shown in previous studies that multiple solutions can be found for the "optimal" geometry and that it is efficient to pseudo-randomly distribute elements within a given aperture so long as the nearest neighbor spacing is approximately half wavelength [77].

The difference in array resolving power when one increases from 4 to 6 element is substantial, however the performance gained by further increasing the array density is less substantial (as seen in the change of 6 to 8 sensors in the BNL array). It is expected that as more sensors are added to an array, the increase in performance becomes less significant, therefore we seek to determine how

much additional resolving power is gained by increasing beyond this 8 element limit. For feasibility of installation and maintenance, an upper limit of $10 - 12$ elements has been chosen. Considered here are a symmetric 8 element array arranged in a pair of centered squares with a 4 kilometer aperture and a 12 element array arranged along the line,

$$r(\theta) = 3.325 \ln\left(1 + \frac{\theta}{\pi}\right), \qquad \theta = 0 \ldots \frac{7\pi}{2}. \tag{159}$$

This results in a 5 kilometer aperture array in which the inter-element spacing varies slightly but remains approximately $\frac{\lambda}{2}$. Both array geometries are shown in Fig. 30.

The response of these two array designs to signals separated by 15^o and 10^o at various signal strengths is shown in the left and right sides of Fig. 31 respectively. The improvements in resolving power by increasing the element count from 8 to 12 is still significant. For a pair of signals separated by 15^o, the 12 element is able to resolve the local maxima of the separate signals for SNR of two or greater. The 8 element array is nearly able to resolve the two signals at an SNR of 4, and easily able to resolve the second signal once the SNR increases to 8. The 8 element array is never able to identify the second peak when the signals are separated by only 10^o, while the 12 element array can distinguish the separate peaks for sufficiently high SNR. For both arrays, the second signal is not visible below an SNR of 2, although there is some asymmetry in the beams

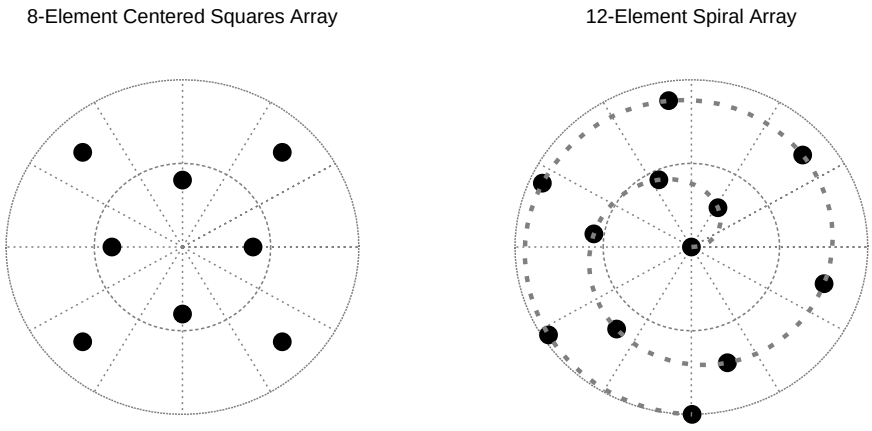

Fig. 30: The symmetric array geometries tested to determine optimal array design for microbarom monitoring. (Left) 8 elements in a pair of centered squares with aperture of 4 kilometers. (Right) 12 elements in a logarithmic spiral with aperture 5 km.

which could be used to infer the presence of a second signal.

Recommendations for Future Work

The limiting resolutions of the array geometries investigated here are presented in Table 2. These results have been obtained by maintaining the dominant signal at a fixed azimuth and continuously varying the azimuth of the weaker signal to determine the separation at which each array design is no longer able to resolve the separate signals at fixed SNR. From these results it is immediately clear that the 4- and 6-element arrays which were used in this project were not sufficient to resolve the nearly coincident microbaroms theorized to be generated by the storm. Additionally, the enhanced 8-element array at Brookhaven National Lab under performs a symmetric aperture array. This is due to the wider longitudinal aperture which enhances its resolving power for signals incident from the north and south, but weakens its resolving power for signals from the east and west. It is likely that if additional elements are to be added to the array, efforts should be made to extend the latitudinal aperture of the array.

From these results, it is clear that in order to consistently distinguish the nearly coincident signals predicted for microbaroms around a large maritime storm at low SNR, one requires an array with aperture of at least $4-5$ km and a minimum of $10-12$ elements. Because of the abundance of

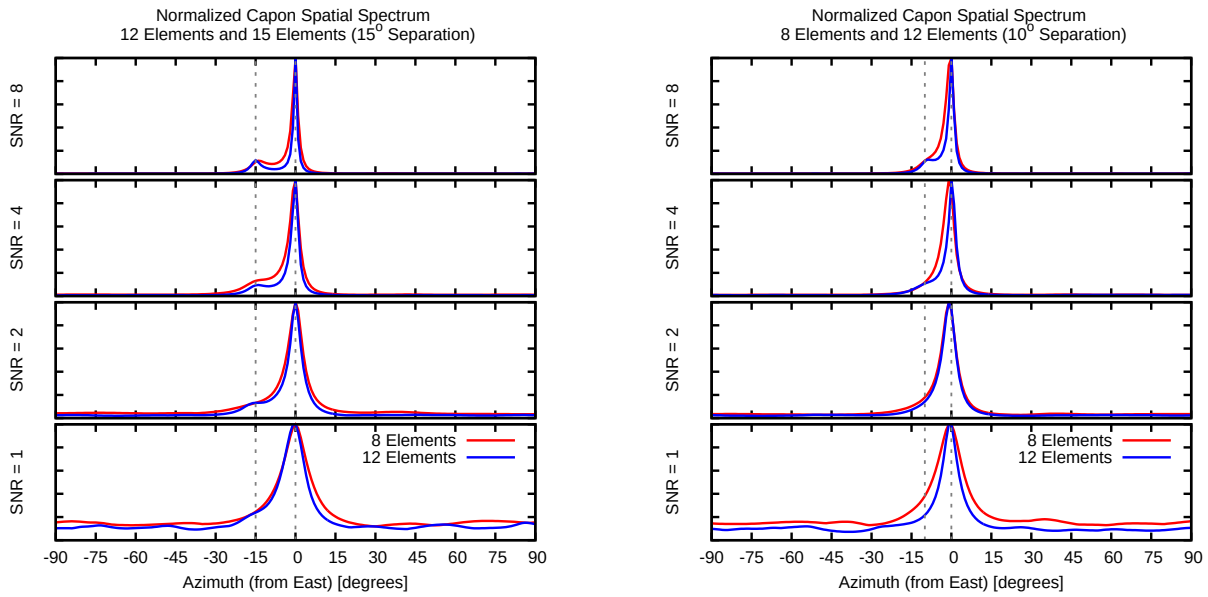

Fig. 31: Array response for a pair of signals separated by 10^o and 15^o incident on the arrays shown in Fig. 30.

Resolving power of array designs			
Array Design	Aperture	SNR 2	SNR 4
4 Element C-Triangle	1.4 km	58^o	53^o
6 Element BNL Array	3 km	33^o	26^o
8 Element BNL Array	3 km	30^o	24^o
8 Element C-Squares	4 km	22^o	19^o
12 Element Spiral	5 km	16^o	13^o

Table 2: The limiting signal separation at which each array geometry can distinguish a pair of incident signals with 10 dB amplitude difference. SNR is given relative to the stronger signal..

infrasonic energy and the inability to predict where other additional signals could be produced, it is best to design the array as symmetrically as possible in order to reduce biasing sensitivity in certain azimuths. Thus, the ideas from random array methods are useful in selecting an aperture size and pseudo-randomly distributing the elements such that the nearest neighbor spacing is $\sim \frac{\lambda}{2}$. It could be beneficial to increase the element count beyond 12, however such increases lead to additional analysis problems when the sensor to snapshot ratio is kept below unity. Increasing the number of snapshots extends the sample window to a limit in which the signal may no longer satisfy the ergodic condition and the azimuth may varying within a sample window.

CHAPTER 6

ANALYSIS OF THE STORMS

A total of five storms observed during the 2010 and 2011 Atlantic Hurricane seasons produced data applicable to this project. Hurricane Igor in September of 2010 provided a useful case to study data processing performance. During the 2011 Atlantic Hurricane season, hurricanes Irene, Katia, Maria, and Ophelia produced measurable microbaroms along the eastern coast of the United States. The data presented here has been processed using the methods discussed in Chapter 5 for arrays of limited size. For each storm, a time sequence of detection back azimuths and beam widths were calculated from measurements. These results were then smoothed using a Kalman statistical tracking filter and used to create tracking animations. The following discussion includes frames from these tracking results along with discussion of the implications of these measurements.

Statistical Tracking Using the Kalman Filter

The azimuths calculated using the recorded infrasonic data contain some uncertainty and noise due to additional coherent sources, incoherent energy, and a number of other noise sources. In order to smooth the time dependent results, we have processed the results of the beamforming through a Kalman filter, a statistical algorithm which uses a model of the observed system and iteratively incorporates new data into a filtered version of the input [78]. The Kalman filter functions by taking a physical model of the observable and some known current state to predict the state which would be measured some time later. Once the subsequent measurement is entered, the filter calculates a correction using its prediction and the new measurement. Finally, the current state is updated with the new information and a new prediction is made. This process is repeated each time a new measurement is made.

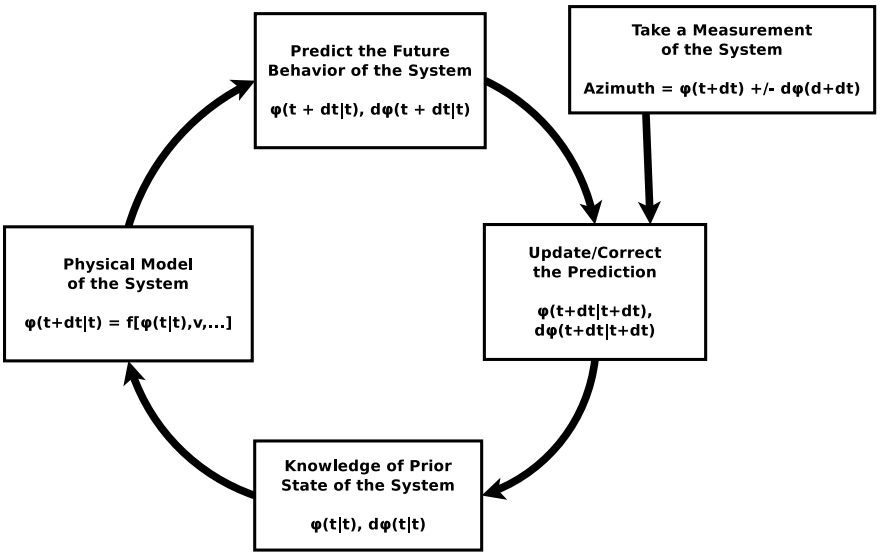

Fig. 32: Azimuth tracking using the Kalman statistical filter.

A graphical form of the Kalman filter as used for azimuth tracking is shown in Fig. 32. In the figure, one starts at the low point on the cycle where the state of the system is described by an observed azimuth, $\phi(t|t)$, and beam width, $d\phi(t|t)$, which are known at time t. Using the physical model, a prediction is made that at a later time $t + dt$, a measurement of the system will return an azimuth, $\phi\,(t + dt|t)$, with a beam width, $d\phi\,(t + dt|t)$. Once the new measurement, $\phi(t + dt)$ and $d\phi(t + dt)$, is given to the Kalman filter, it compares its prediction with the system and uses that to produce a new known state of the system. The process updates the expected observables as long as there are measurements being given to the filter. If no additional measurements are given, the the Kalman filter allows the uncertainty, $d\phi$, to increase at some rate with increased dt according to the model of the system.

Analysis of the Storms from the 2010 and 2011 Atlantic Hurricane Seasons

The Kalman filter discussed in the previous section has been used to produce time series of azimuths and beam widths for each array during the various storms recorded during 2010 and 2011. The results to be discussed have been organized as shown in Fig. 33. The upper right of the figure identifies the storm being analyzed as well as the date and time, in GMT, of the window of data being analyzed. The data has been analyzed using six minute windows, thus the example here shows the results for data recorded between 20:33 and 20:39 on September 18th, 2010. The left side of the figure shows the array geometry at each site with the radial scale for reference. The azimuth

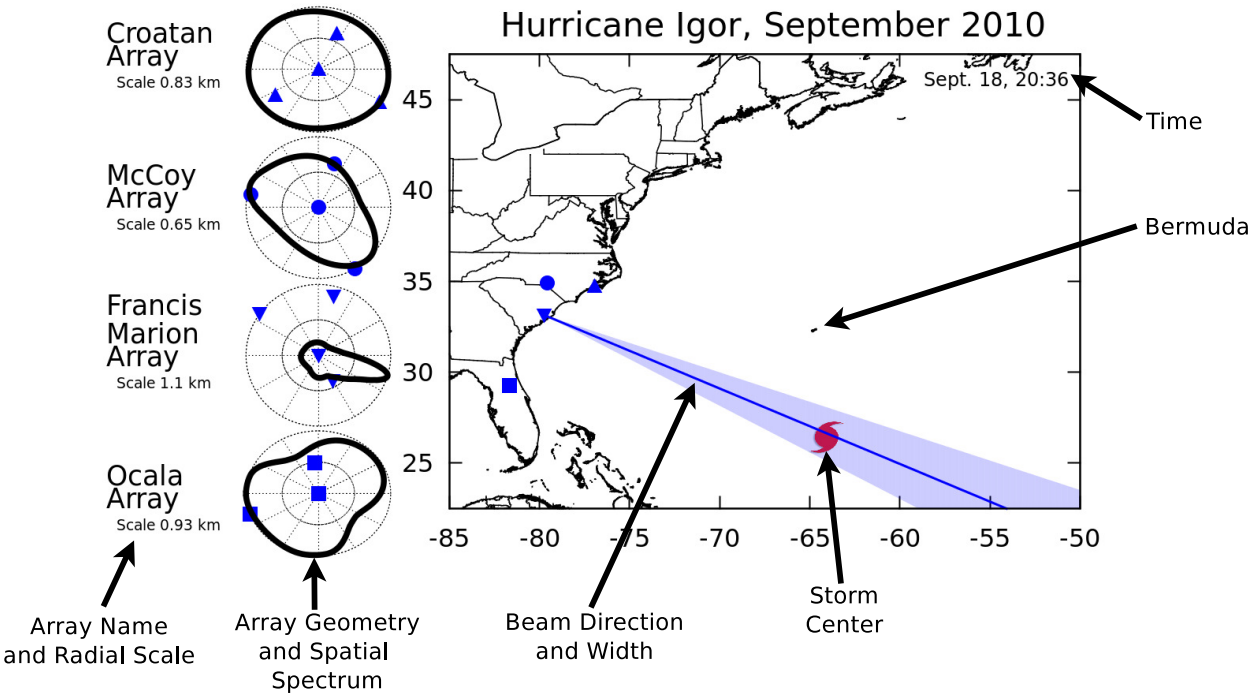

Fig. 33: Example of beamforming analysis results. The spatial spectra at various arrays are shown on the left. Time, beam directions, beam widths, and the location of the storm are shown on the right.

of the maximum and associated beam width have been calculated as discussed in Chapter 5. In the case that a clear signal is evident from the Atlantic, the resulting direction and width of the beam at each array are plotted in the right panel of the figure along with the storm location. In the example shown, only the array at Francis Marion is detecting coherent signal and therefore only that beam is plotted. The red spiral symbol in the right panel denotes the location of the storm at the time indicated in the figure. The location of Bermuda is noted here because the island's relative location to that of the storm is useful to describe the storm trajectory through the Atlantic.

Hurricane Igor Results

Hurricane Igor was one of the most intense storms of the 2010 Atlantic hurricane season and although it did not make landfall in the United States, it produced large storm swells and damaging winds in Bermuda and Newfoundland where it did made landfall. Igor formed in the equatorial Atlantic on September 8th, 2010 and remained at hurricane intensity until September 21st. The storm reached a maximum intensity of category 4 with maximum wind speeds of 70 $\frac{\text{m}}{\text{s}}$, though it weakened to a category 1 storm by the time it reached Bermuda and maintained that intensity until it made landfall in Newfoundland [79].

The storm track and results of microbaroms recorded during Hurricane Igor are shown in Fig. 34. In the upper panels of the figure, showing results at 03:06 and 05:15 on September 18, it is evident that as Hurricane Igor approached the south-east coast of the US, the arrays detected signal incident from around the storm. The beam widths at Croatan, McCoy, and Francis Marion are large possibly due to low signal to noise ratios or to multiple coherent signals from similar azimuths as predicted in Chapter 3. Comparing the spatial spectra at 03:06 and 05:15, the beam widths at the later time have decreased appreciably. This is likely due to decreased wind and anthropogenic noise at the array locations during the overnight hours. Additional analysis shows similar behavior in that data recorded during the day and night at all array locations. Thus, analysis here has

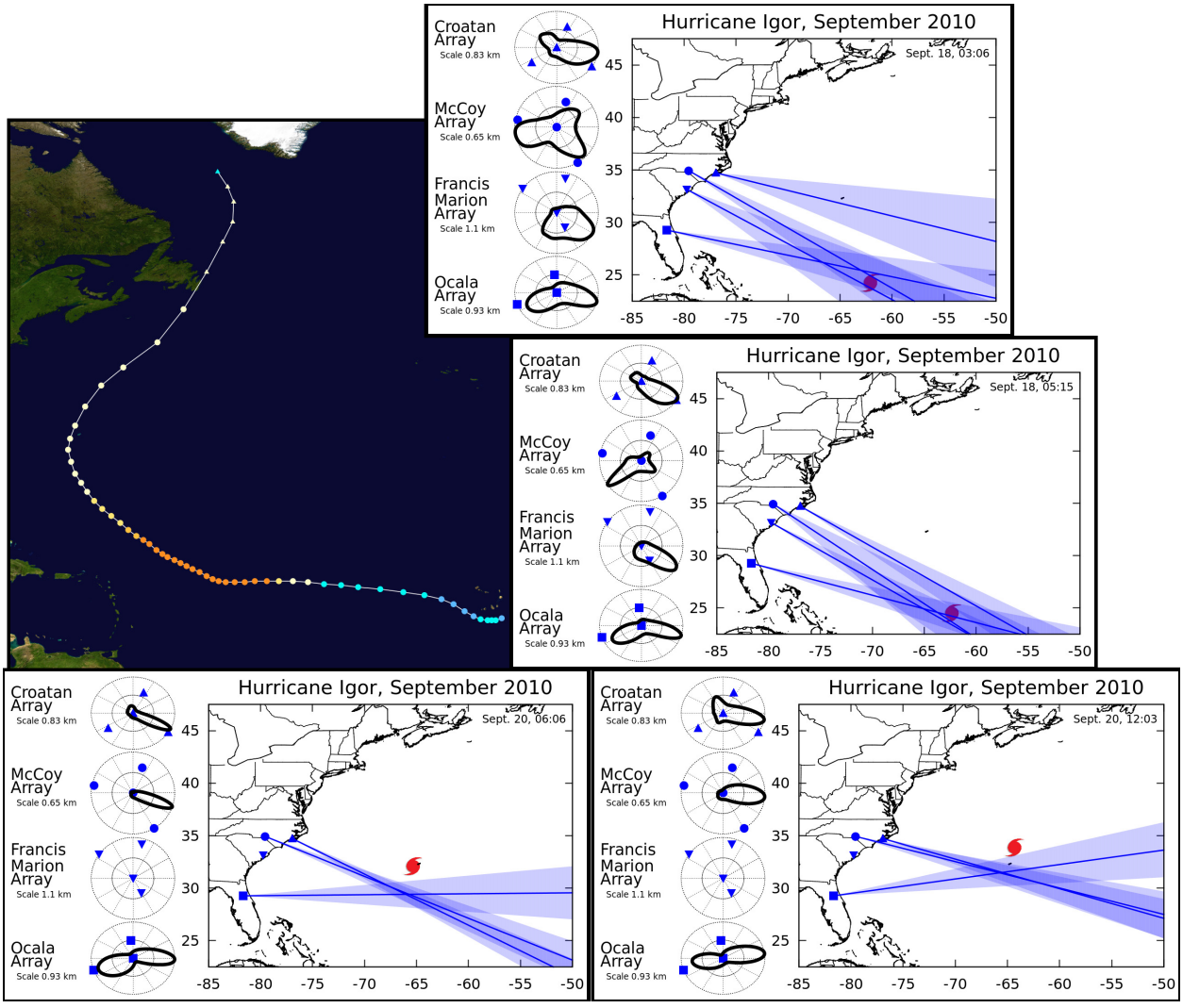

Fig. 34: The storm track, spatial spectra, and resulting beam directions for data recorded during Hurricane Igor during September of 2010..

focused on data obtained during the overnight hours when infrasonic noise levels are reduced.

In the lower panels of the figure, those at 06:06 and 12:03 GMT, the storm has moved nearer to the array latitudes. The beams widths continue to decrease significantly. The combined azimuths clearly identify a source of the microbaroms to the south of the storm at the location in which the beams converge. This observed source location is in agreement with the model presented in Chapter 2. The propagation distance from the indicated source region is over 1,000 kilometers, however there is sufficient microbarom energy to provide high signal to noise and produce the very narrow beam widths observed in the lower panels of Fig. 34.

Hurricane Irene Results

Hurricane Irene formed in the equatorial Atlantic on August 21, 2011 and reached a maximum intensity of Category 3 with wind speeds of 55 $\frac{\mathrm{m}}{\mathrm{s}}$. Irene has been ranked as one of the ten costliest storms to hit the United States in recorded history. The storm maintained hurricane intensity until August 28th and made land fall in North Carolina near Cape Lookout and the eye of the storm made landfall within a few kilometers of the Croatan array [80]. We have not included the interaction of the storm swell with a coast line, however, it is reasonable to expect that the reflected surface waves from the coast line could produce additional microbarom source regions. Despite this, data recorded by the Ocala and McCoy arrays in Florida and North Carolina respectively provide applicable data for analysis before the storm made landfall.

The storm track and spatial spectra analysis results for Hurricane Irene are shown in Fig. 35. In all the frames in the figure, the array in Ocala is able to identify microbaroms emanating from a region south of the storm center where the source is expected to be located. In the earliest time presented here, 14:39 on August 26th, the McCoy array detects coherent energy emanating from around the storm center, however, the asymmetry of the spatial spectrum at the array hints that there are likely multiple contributions which cannot be resolved separately. Several hours later, in the 21:15 frame, the signal at McCoy has becomes stronger and more symmetric, indicating a single signal which still appears to emanate from near the storm center.

In the lower left panel, at 07:42 on August 27, the array at Ocala is still able to identify the source region to the south of the storm as predicted in the model, however, the storm winds produce excessive wind noise on the arrays in the Carolinas and no coherent signal can be resolved.

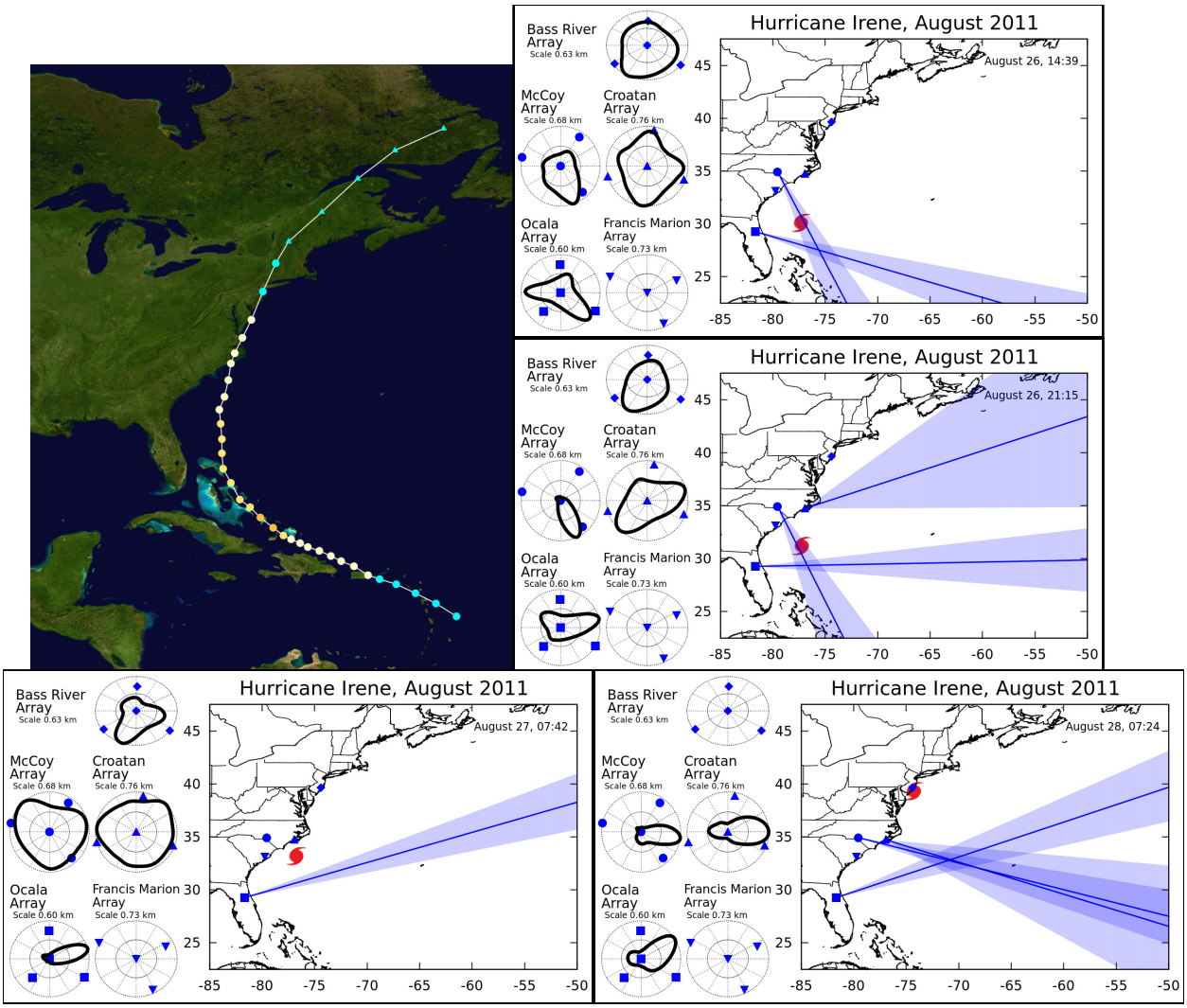

Fig. 35: The storm track, spatial spectra, and beam directions relative to the storm for data recorded during Hurricane Irene in August of 2011.

Note that the Bass River array shows a wide maximum in the spatial spectrum from the south-west, which coincides with the general direction to the storm. The following day, at 07:24 on August 28, the storm has moved further northward along the coast and the arrays in Florida and the Carolinas detect microbaroms emanating from the region in which the beams converge. In both of these later frames the storm induced waves interact with the continental coast line and the storm is no longer in the "open ocean". Because of this, the model discussed in Chapter 2 is no longer an accurate description of the storm system and other microbarom radiating regions are likely formed due to the reflection of waves from the coast.

Hurricane Katia Results

Hurricane Katia formed in the equatorial Atlantic south of Cape Verde on August 29, 2011, and strengthened to a Category 4 intensity storm by September 5 before weakening to Category 1 and moved east toward the North Sea where it merged with a second storm system and produced strong winds and waves across the United Kingdom during September 11-13 [81]. The storm did not make other landfalls during its time in the Atlantic, and therefore provides a useful example of a storm in open water producing microbaroms. Katia's path through the Atlantic was similar to Hurricane Igor's in 2010 and therefore it is useful to compare the characteristics of the microbaroms detected from the two storms.

The storm track and results for microbaroms analyzed during Hurricane Katia are shown in Fig. 36. In the upper panels, on September 5 and 6, the storm reaches its maximum intensity and microbaroms are detected at the Ocala and McCoy arrays with back azimuths indicating the signal is emanating from around the storm center. On September 6, the storm is nearer to the coast and the azimuths are markedly more well defined in the spatial spectra on the two arrays. Comparing these with the observations made during Hurricane Igor in 2010, it is found that the back azimuths are similar. In both cases the storm moves through the region at 60^o to 70^o W longitude and 25^o to 30^o N latitude with high storm intensity and produces microbaroms at the arrays in Florida and the Carolinas with back azimuths centered around the storm center.

On September 8, the storm moved nearer and past the latitude of Bermuda. Unlike Hurricane Igor in 2010, Hurricane Katia did not make landfall in Bermuda and progressed through the Atlantic several hundred kilometers to the west of the island. The microbaroms detected at 05:54 on the Ocala and Croatan arrays provide an estimate of the location of the microbarom source region to the south of the storm at the time. The spatial spectrum on the McCoy array shows a very wide, asymmetric maximum which implies multiple contributions which the array cannot separately resolve. One of these arrivals appears to emanate from directly east and the other from the south-east. In the results at 13:18, the behavior of the Croatan and McCoy spatial spectra swap. The beam at McCoy, and the beam at Ocala in fact, narrow significantly and indicate a clearly defined microbarom signal emanating from the expected source location. The Croatan spatial spectrum contains an asymmetric maximum with a contribution from the south-east and a second contribution from directly east.

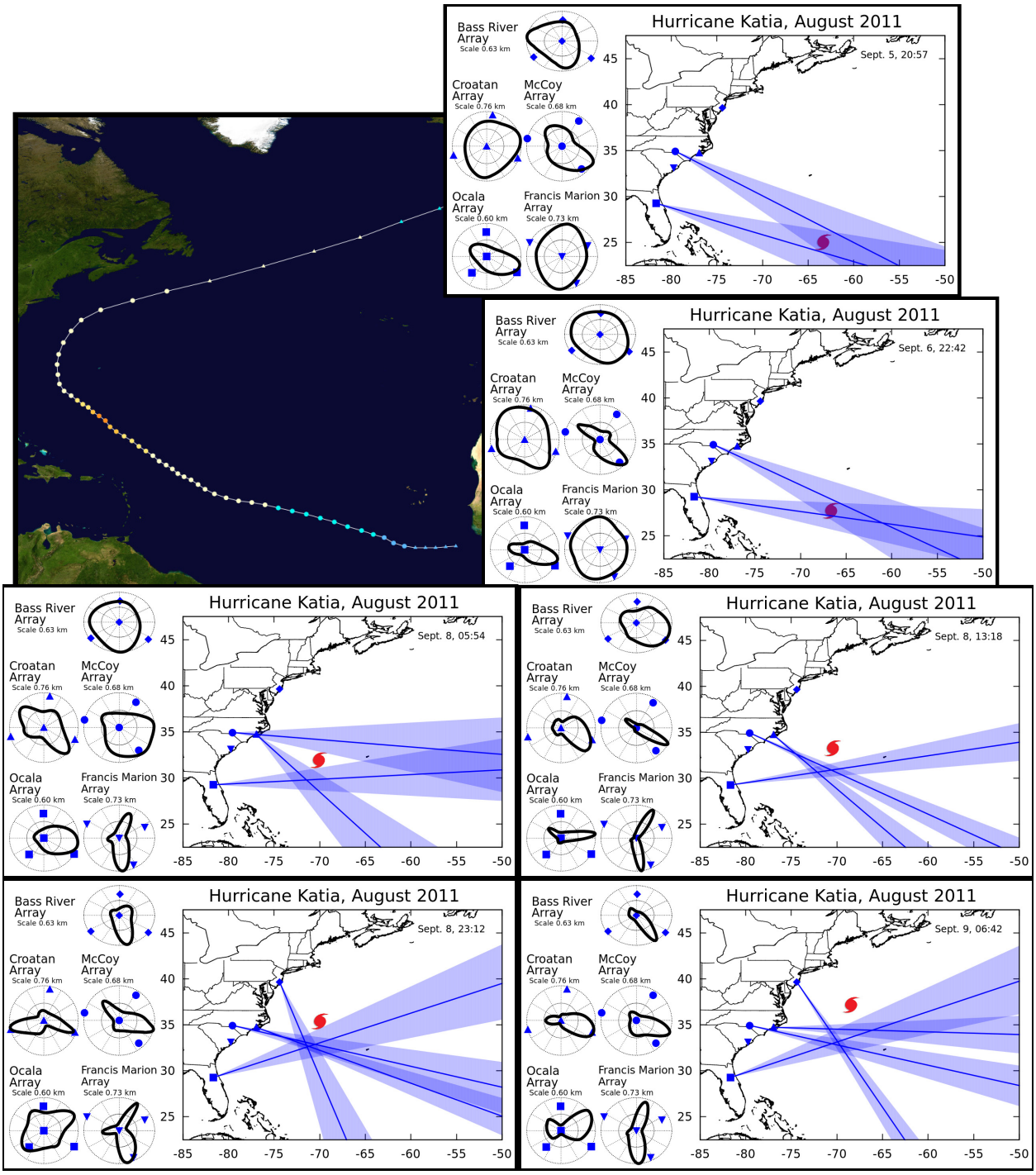

Fig. 36: The spatial spectra and beam directions relative to the storm position for data recorded during Hurricane Katia during September of 2011.

In both cases, the contribution from the south-east indicates a coherent signal from near the location at which the beam from Ocala converges with the other beam, which is in agreement with the expected microbaroms source location. The second contribution from the east would indicate signal from around the storm itself, consistent with the refraction effects predicted by the propagation model in Chapter 3, though the anomalous arrival is not expected to extend this far around the storm. It's possible that the gradient of winds in the eye columns is more severe than modeled by the Holland cyclonic wind model. The observation that this second arrival is present at the McCoy array and not Croatan at 05:54 and then present at Croatan and not McCoy for the later observation at 13:18 can be explained by the formation of bands of ensonified regions in the three dimensional propagation model. At the earlier time, McCoy was contained within the region in which the anomalous arrivals are present and Croatan was not, and in the later case, the ensonified region shifted such that Croatan was within the region and McCoy was not.

In all observations on September 8 and 9, a microbarom source region located to the south of the storm is implied by the converging beams in that region. The last panel, September 9 at 06:42, clearly identifies a source region for the microbaroms located south of the storm. These results along with those in the lower panels of Fig. 34 provide convincing evidence that the source region of microbaroms due to a large maritime storm in the Atlantic trails to the south of the storm in the open ocean as predicted by Hetzer et al. and as discussed in Chapter 2.

Hurricane Maria Results

Hurricane Maria was a weaker storm which formed in the central equatorial Atlantic on September 6, 2011. A combination of high vertical wind shear and cooler sea temperatures in that region weakened the storm into a low-pressure area soon after forming. The storm later moved north, passing to the west of Bermuda before strengthening to a Category 1 storm with wind speeds of 35 $\frac{\text{m}}{\text{s}}$ and passing near to Newfoundland [82]. The storm provided very weak microbarom signals, but is included in this discussion to demonstrate the necessity to use appropriate array designs and data processing in continued work regarding microbaroms due to large maritime storms.

The storm track and results from Hurricane Maria are shown in Fig. 37. In the upper most panel, September 14 at 03:36, all of the arrays indicate a strong coherent signal emanating from the northern Atlantic, likely due to the large microbarom source which forms to the south

of Greenland in this region. In this region, converging currents are known to microbaroms which, under the appropriate atmospheric conditions, can propagate toward Newfoundland and the eastern United States. This signal can often overwhelm any microbarom signal coming from the central and equatorial Atlantic. Examination of the spatial spectra on the arrays in Ocala, McCoy, and Croatan at this time, one notices that weaker local maxima are present which would indicate signal emanating from the south-east, which would be consistent with the observations of Hurricane Igor and Katia as they progressed through the similar region of the Atlantic (the September 18 frames in Fig. 34 and September 5 and 6 frames in Fig. 36).

In the lower right panel, September 15, Hurricane Maria has progressed northward in the Atlantic to the latitude of the Ocala array. At this time, microbaroms are detected emanating from around the storm on the McCoy and Croatan arrays, however, microbaroms produced in the Gulf

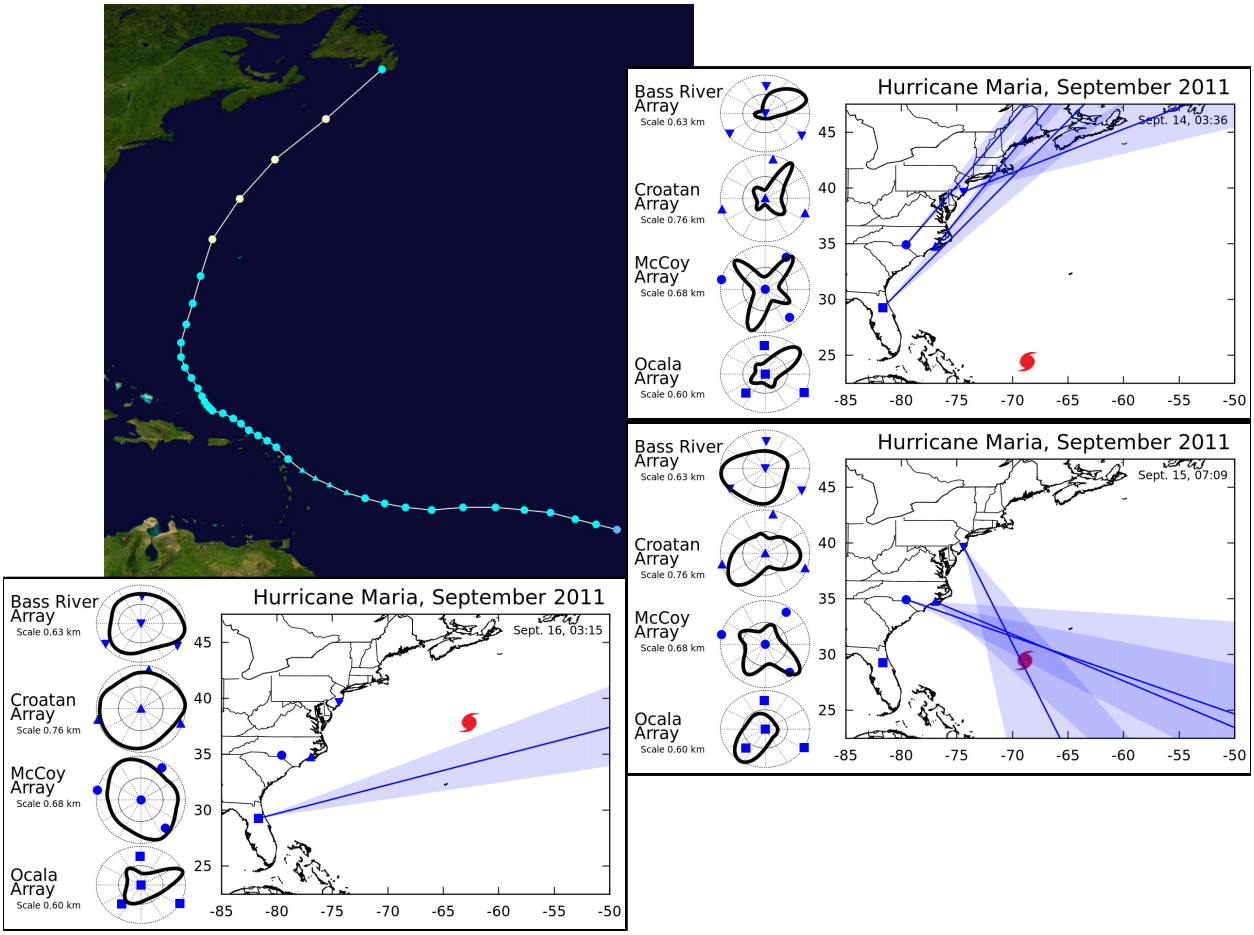

Fig. 37: The spatial spectra and beam directions relative to the storm position for data recorded during Hurricane Maria during September of 2011.

of Mexico produce additional coherent signals which complicate the spatial spectra of all arrays. In the final frame, September 16, the storm has moved north-east through the Atlantic. The array in Ocala is able to detect some coherent energy from the region south of the storm, however, the other arrays cannot detect any coherent signal and it is not possible determine if the signal detected at Ocala is due to a microbarom source region to the south of the storm or some other location along the beam.

In all of the results for Hurricane Maria, weak signal strength and the presence of multiple signals in the data record complicate the identification and analysis of microbaroms produced by the storm. As discussed in the array optimization section of Chapter 5, denser arrays can be used to increase the effective signal strength and by arranging the array to limit biasing of one azimuth to another, multiple contributions to the data record can be separated. Thus, it is critical to future research that arrays be designed so that any microbaroms generated by non-storm sources such as those in the northern Atlantic and Gulf of Mexico can be separated from the microbarom signals produced by large maritime storms even in the case of weak signal strength from the storm induced microbaroms.

Hurricane Ophelia Results

Hurricane Ophelia was the most intense storm of the 2011 Atlantic hurricane season, reaching a sustained wind speed of 63 $\frac{\mathrm{m}}{\mathrm{s}}$ corresponding to a Category 4 intensity. The storm formed in the central equatorial Atlantic on September 20 and strengthened as it moved north through the Atlantic, passing to the east of Bermuda and weakening to a Category 1 when its outer bands produced strong winds and heavy rain in Newfoundland [83]. Because Ophelia remained in the open Atlantic, it was expected to provide useful data similar to that of Hurricane Igor in 2010 and Katia earlier in 2011. However, the storm remained east of Bermuda and formed in late September, resulting in weaker signals than those produced by other storms. The reason for this is a combination of the increased propagation range from the storm to the arrays and a seasonal change in the winds in the stratosphere around the time of the autumnal equinox. The microbaroms produced by the storm propagated hundreds of additional kilometers compared with the other storms discussed here and underwent stronger attenuation due to propagation through the rarefied air in the thermosphere.

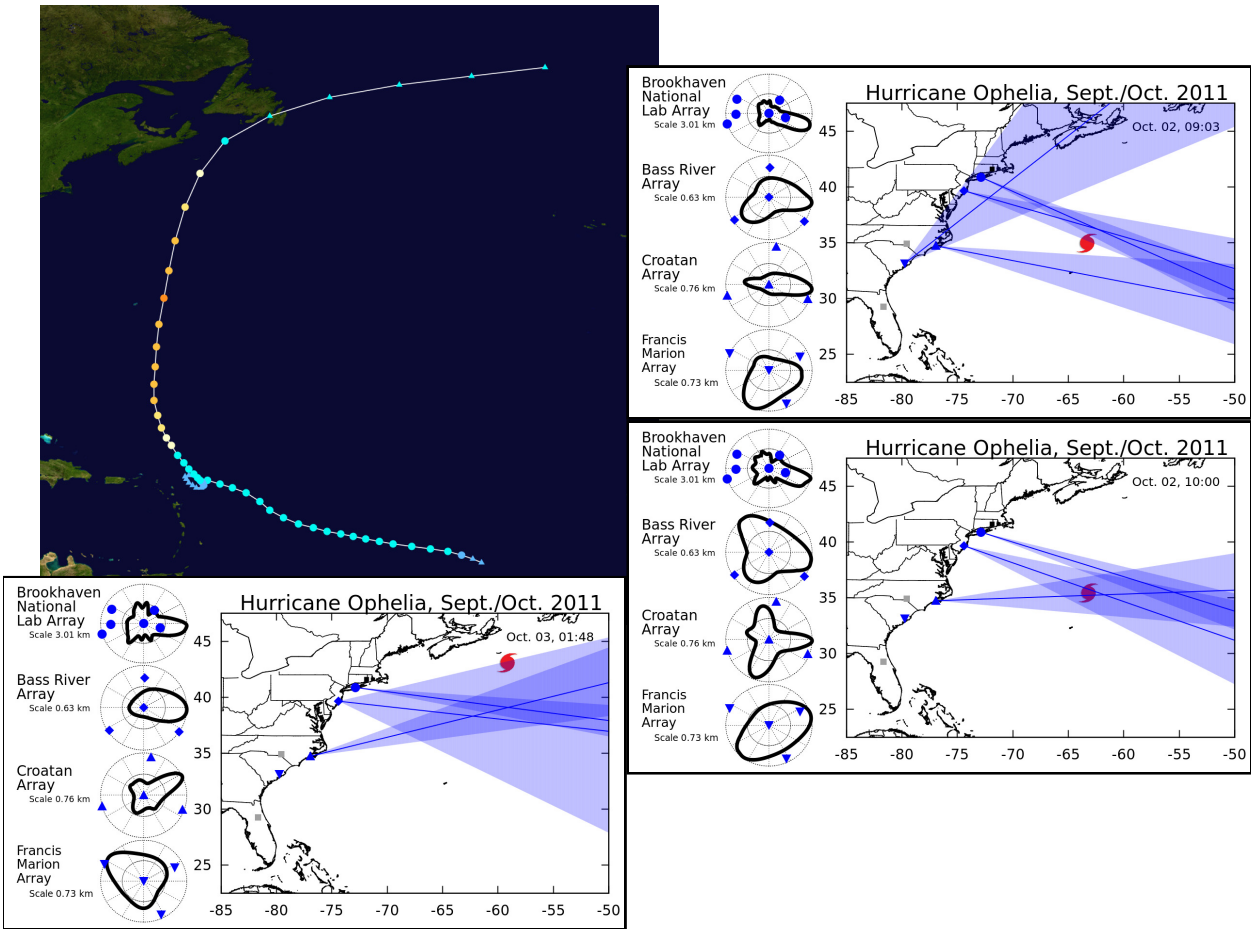

Fig. 38: The spatial spectra and beam directions relative to the storm position for data recorded during Hurricane Ophelia during October of 2011.

The storm track and results for data recorded during Hurricane Ophelia are shown in Fig. 38. In the uppermost panel, October 2 at 09:03, signal is detected on the Brookhaven and Bass River arrays from around the storm center and on the Croatan array from south of the storm. Roughly an hour later, at 10:00, the results are similar, but additional sources complicate the spatial spectra on the arrays at Bass River and Croatan. It should be noted that the additional elements at the Brookhaven array provide enhanced noise reduction and resolving power to separate multiple signals. In this result at 10:00, the beam at Brookhaven contains two contributions which are narrowly separated which both appear to emanate from the storm center. On the following day, October 3, the storm had moved north of all arrays and although signals are weak due to the increased propagation range and thermospheric attenuation, the beams at Brookhaven, Bass River, and Croatan converge at a location to the south of the storm.

Summary of Microbarom Observations During the 2010 and 2011 Hurricane Seasons

During the 2010 and 2011 Atlantic hurricane seasons, infrasonic measurements have been taken at locations in Florida, South Carolina, North Carolina, New Jersey, New York, and Connecticut. During these two years, infrasonic measurements have been analyzed during five storms of at least Category 1 intensity. In all of these cases, once the storm moved sufficiently far north into the open Atlantic, combined back azimuths of coherent signal detected from multiple the arrays indicated a source region south of the storm system from which the microbarom signal appears to emanate. In all cases except for Hurricane Maria, multiple arrays produced beams which converged in a location south of the storm system. These observations are in agreement with the model described in Chapter 2 which predicts microbaroms to be generated in a region away from the storm center where the interaction of the storm swell and the background Atlantic swell produce the counter propagating surface wave structure required for microbarom radiation. In one of these cases, Hurricane Irene in 2011, it must be noted that the observations were made while the storm made landfall along the Atlantic coast of the United States and interaction with the coast has not been included in our storm model. During the time that Hurricane Irene approached the coast, the array in Ocala was able to identify a microbarom source azimuth consistent with the other observations. However, without a second array to provide an intersection of multiple azimuths, an approximate location for the source cannot be found.

Analysis of the data from arrays north of the storm system provide consistent results that a microbarom signal appears to emanate from the general region around the storm center when observed from the north-west. In all of these cases, the beam width of the detection is much larger compared to the detections from south of the storm as one would expect for signal which has interacted with the storm in some manner. This observation has been made repeatedly during Hurricanes Igor, Katia, and Ophelia. In all three cases, as the storm approached arrays from the south, multiple arrays would indicate signal emanating from around the storm itself. Additional experiments using denser arrays and a more robust data processing method would provide clarification of whether the cause of the wide beams in these observations is low signal to noise levels or to multiple arrivals with similar azimuths as predicted by the propagation modeling in Chapter 3.

It should also be noted that the alternate microbarom generation mechanism proposed

by Stopa et.al. in Ref. [27] would produce microbaroms in the storm center which then radiate away symmetrically in all directions from the storm. Such a source could explain the presence of the observed anomalous microbarom signal. It would be possible to determine if the anomalous microbaroms observed here are the result of refraction or an additional source region by increasing the number of arrays deployed and monitoring multiple locations around a storm to determine if the anomalous arrivals are present at all locations around the storm. In the case that the anomalous arrivals are found to be present in all directions around the storm, it is likely that the microbaroms are being generated in the storm center as proposed by Stopa et al.. Alternately, if it were found that the anomalous arrivals are only present in the regions predicted by the refraction models, then it is likely that the source is due to the interaction discussed in Chapter 2 and the anomalous arrivals are produced by the propagation effects discussed in Chapter 3. The observations reported here show definite azimuth dependence on the anomalous arrivals since they are only observed from the north-west side of the storm, however additional observations are necessary to determine with certainty which model more accurately explains the anomalous signals from the storm center.

Lastly, in the case in which the storm made landfall near an array, some useful observations can be made. Referring back to the data taken on the Ocala and McCoy arrays during Hurricane Irene in Fig. 35, it is possible that some contribution of the signal arriving at the McCoy array has propagate through the storm. During this storm, the direction to the source is indicated by the array in Ocala, however without a second array it is not possible to identify where along that azimuth the source is located. As the storm approached the coast, the arrays at McCoy, Croatan, and Bass River detected coherent energy emanating from around the storm, though the back azimuth at McCoy was the most well defined. It is possible that the observations at McCoy are of signal which has propagated through the storm winds. It is also possible that the signal is the result of propagation over the storm or that the interaction with the coast north of the storm has produced additional microbarom source regions close to the array. Again, additional experiments using denser arrays and more robust data processing methods is required to elucidate where the microbarom signals are produced. Further, a model for the storm, swell, and coast line interaction would provide some predictions of whether or not additional sources would be expected in such a case.

CHAPTER 7

CONCLUSIONS

The physical model for generation of microbaroms and microseisms by active sea states has been incrementally extended over several decades. The most thorough treatment of microbarom generation is that published by Waxler and Gilbert in 2006. The manner in which a large maritime storm produces microbaroms is still a topic of some debate within the research community. It has been shown here that the simple interaction model proposed by Hetzer et al. accurately predicts the location of the microbarom source associated with a large maritime storm. Specifically, the surface waves induced by the strong cyclonic winds generate counter propagating waves relative to the open ocean swell along a line extending radially from the the storm center and perpendicular to the direction of the background swell. At some distance along this radial line, the wavelength of the induced surface waves is equal to that of the background swell. In such a region, the ocean surface is expected to radiate microbaroms. Additionally, as the storm moves through the open ocean, this region of counter propagating waves travels with the storm. Thus, a large maritime storm in the open ocean not only produces microbaroms at a predictable location relative to the background swell, but also carries this source region with it as it moves through the ocean.

When observed along propagation paths away from the storm center, horizontal refraction is weak and the back azimuth of the received signal is expected to be oriented towards the microbarom source region. However, geometric propagation methods have predicted that, along propagation paths which interact with the strong winds near the storm center, strong horizontal refraction can produce a localized region in which the observed back azimuth of the microbarom signal is oriented towards the storm center. It has been shown here that this refraction is produced by the steep radial gradient in the cyclonic winds near the storm eye. Due to this dependence on the wind gradient in the storm eye, the region in which these arrivals are present is expected to increase in

size with increased storm intensity. From these predictions, one can expect that characteristics of this signal might be used to infer some measure of the winds in the storm center.

Infrasonic data has been collected during the 2010 and 2011 Atlantic hurricane seasons from locations along the eastern coast of the United States. From this data set, five storms which reached at least Category 1 intensity and moved through the open Atlantic have been analyzed using beamforming methods to evaluate the back azimuths of the received microbarom signals. It has been found that observations of microbaroms which have weakly interacted with the storm are in agreement with predictions of the source and propagation models discussed here: observations from south of the storm latitude consistently indicate a source region hundreds of kilometers south of the storm center, which is perpendicular to the dominantly westward background swell in the open Atlantic.

When observed from north of the storm latitude, microbaroms are weaker in intensity and oriented with back azimuths directed towards the storm center as predicted by the propagation modeling. These microbaroms with back azimuths oriented around the storm center are observed only when the storm is south of an array's latitude. The asymmetry of these observations is inconsistent with a microbarom source located at the storm center, but is expected for a source to the south of the storm center from which microbaroms propagate through the strong winds around the storm eye. The observations obtained during this work are more accurately explained using the microbarom generation mechanism proposed by Hetzer et al. combined with the propagation methods presented here than using the generation mechanism proposed by Stopa et al..

Additional observations of storms using a larger array network would clarify the extent of the asymmetries in the microbarom signal which appears to emanate from the storm center. In the case that additional research is planned regarding microbaroms generated by large maritime storms, it would be advantageous to attempt observations from additional locations around the storm, particularly locations to the east of likely storm paths. The array locations in this work have been limited to areas of the east coast of the United States, however additional locations at various Atlantic islands would likely provide very useful observations to study the asymmetries of the signal emanating from the storm center. Infrasound data is recorded worldwide on the IMS network, which includes a location at Bermuda, however, data recorded on the IMS Bermuda array has been found to contain excessive levels of wind noise and is unable to provide useful

beamforming results. It should be noted that, in addition to monitoring Atlantic hurricanes, it is likely that observations of typhoons in the Pacific might provide additional insight into the asymmetries of the anomalous signal from the storm center. It would be beneficial for future work to deploy array networks in the Atlantic and Pacific with emphasis on obtaining observations from multiple locations around large maritime storms.

In addition to an expanded array network, improvements to the individual arrays are required to resolve the multi-pathing predicted by the propagation modeling. The four and six element arrays used in this project have been able to detect the presence of the anomalous arrivals northwest of the storm and have been able to identify the source location to the south of each storm as it moves through the Atlantic. However, the propagation predictions indicate that within the region of anomalous arrivals, a weakly interacting signal also contributes to the observed signal. The two signals are expected to differ in back azimuth by at little as 10^o and in amplitude by approximately 10 dB depending on the stratospheric winds. The four and six element arrays used here cannot resolve these separate signals and therefore improved array design is required for continued work. It has been found that in order to resolve two such signals, the array must contain at least $10 - 12$ elements distributed pseudo-randomly over $4 - 6$ kilometers such that the nearest neighbor element spacing is approximately half-wavelength, 850 meters for microbaroms.

The work presented here is an initial step in understanding the manner in which the infrasonic signal observed far from a large maritime storm might be used to estimate some characteristics of the storm structure. The observations presented here indicate that the generation of microbaroms by a large maritime storm can be easily understood by examining the manner in which the surface waves produced by the storm interact with the background oceanic swell. Further, the geometric propagation model used in this work provides insight into the physical mechanism by which the infrasonic signal interacts with the winds in the storm and influences the signal observed far from the storm center. Additional observations and research are required to advance the model and determine whether the predictions made by it are accurate. Given such additional observations and refinement of the model, inversion methods might be developed to passively probe the interior structure of a large maritime storm and continuously monitor wind speeds and wind gradients in the storm center by analyzing characteristics of the infrasonic signal observed at a multitude of locations around the storm.

LIST OF REFERENCES

LIST OF REFERENCES

[1] M. S. Longuet-Higgins. A theory of the origins of microseisms. *R. Soc. Lond.*, 243:A. 857, 1950.

[2] R.K. Cessaro. Sources of primary and secondary microseisms. *Bull Seismol. Soc. Am.*, 84:899–907, 1994.

[3] Claus H. Hetzer, Roger Waxler, Kenneth Gilbert, and Hank Bass. Infrasound from hurricanes: dependence on the ambient ocean surface wave field. *Geophys. Res. Lett.*, 35:L14609, 2008.

[4] A. Le Pichon, E. Blanc, and A Hauchecorne. *Infrasound Monitoring for Atmospheric Studies*. Springer, New York, NY, 2010.

[5] K.T. Law and J.S. Hobgood. A statistical model to forecast short-term atlantic hurricane intensity. *Weather Forecast*, pages 967 – 981, 2007.

[6] Allan D. Pierce. *Acoustics: An Introduction to its Physical Principles and Applications*. Acoustical Society of America, Woodbury, NY, 1981.

[7] L.D. Landau and E.M. Lifshitz. *Fluid Mechanics*, volume 6 of *Course of Theoretical Physics*. Butterwork-Heinemann, Burlington, MA, 1959.

[8] Leonid M. Brekhovskikh and Oleg A. Godin. *Acoustics of Layered Media I: Plane and Quasi-Plane Waves*, volume 5 of *Springer Series on Wave Phenomena*. Springer-Verlag, Berlin, Germany, 1998.

[9] Leonid M. Brekhovskikh and Oleg A. Godin. *Acoustics of Layered Media II: Point Sources and Bounded Beams*, volume 10 of *Springer Series on Wave Phenomena*. Springer-Verlag, Berlin, Germany, 1999.

[10] J.R. Bowmann, G.E. Baker, and M. Bahavar. Ambient infrasound noise. *Geophys. Res. Letters*, 23:L09803, 2005.

[11] Guilhem Barroul, Domanique Raymond, Fabrice R. Fontaine, Olvier Hyverhaud, Vincent Maurer, and Keitapu Maamaatuaiahutapu. Characterizing swells in the southern pacific from seismic and infrasonic noise analyses. *Geophys. J. Int.*, 164:516 – 542, 2005.

[12] William L. Donn and David Rind. Microbaroms and the temperature and wind of the upper atmosphere. *J Atmo. Sciences*, 29:156–172, 1971.

[13] M. Garces, M. Willis, C. Hetzer, A. Le Pichon, and D. Drob. On using ocean swells for continuous infrasonic measurements of winds and temperature in the lower, middle, and upper atmosphere. *Geophys. Res. Letters*, 31:L19304, 2004.

[14] A. Le Pichon, L. Ceranna, M. Garces, D. Drob, and C. Millet. On using infrasound from interacting ocean swells for global continuous measurements of wind and temperature in the stratosphere. *J. Geophys. Res.*, 111:D11106, 2006.

[15] David Rind and William L. Donn. Further use of natural infrasound as a continuous monitor of the upper atmosphere. *J. Atmos. Sciences*, 32:1694–1704, 1975.

[16] David Rind and William L. Donn. Infrasound observations of variability during stratospheric warmings. *J. Atmos. Sciences*, 35:546–553, 1977.

[17] J.R. Benioff and B. Gutenberg. Wave and currents recorded by electromagnetic barographs. *Bull. Am. Met. Soc.*, 20, 1939.

[18] H.F. Baird and C.J. Banwell. Recording of air-pressure oscillations associated with microseisms at christchurch. *N Z J Sci Tech*, 1940.

[19] William L. Donn and Bhoopal Naini. Sea wave origin of microbaroms and microseisms. *J. Geophys. Res.*, 70(21):4482–4488, 1973.

[20] S.K. Banerji. Microseisms associated with disturbed weather in the indian seas. *Phil. Trans. Roy Soc London*, 229:287 – 328, 1930.

[21] K. Hasselmann and D. Olbers. A statistical analysis of the generation of microseisms. *Rev. Geophys.*, 1(2):177–210, 1963.

[22] Roger Waxler and Kenneth Gilbert. The radiation of atmospheric microbaroms by ocean waves. *J. Acoust. Soc. Am.*, 119(5):2651–2664, 2006.

[23] Steve Ardent and David Fritts. Acoustic radiation by ocean surface waves. *J. Fluid Mech.*, 415:1–21, 2000.

[24] Laslo. G. Evers and P. Siegmund. Infrasonic signature of the 2009 major sudden stratospheric warming. *Geophys. Res. Letters*, 36:L23808, 2009.

[25] J.X. Dessa, J. Virieux, and S. Lambotte. Infrasound modeling in a spherically heterogeneous atmosphere. *Geophys. Res. Lett.*, 2005.

[26] Kristoffer T Walker. Evaluating the opposing wave interaction hypothesis for the generation of microbaroms in the eastern north pacific. *Journal of Geophysical Research: Oceans (1978–2012)*, 117(C12), 2012.

[27] Justin E Stopa, Kwok Fai Cheung, Milton A Garcés, and David Fee. Source of microbaroms from tropical cyclone waves. *Geophysical Research Letters*, 38(5), 2011.

[28] Justin E Stopa, Kwok Fai Cheung, Milton A Garcés, and Nickles Badger. Atmospheric infrasound from nonlinear wave interactions during hurricanes felicia and neki of 2009. *Journal of Geophysical Research: Oceans (1978–2012)*, 117(C12), 2012.

[29] I. M. Brekhovskikh, V. V. Goncharov, V. M. Kurtepov, and K. A. Naugol'nykh. The radiation of infrasound into the atmosphere by surface waves on the ocean.

[30] Blair Kinsman. *Wind Waves: Their Generation and Propagation on the Ocean Surface*. Prentice Hall, Englewood Cliffs, NJ, 1965.

[31] G. J. Komen, L. Cavaleri, K. Hasselmann, S. Hasselmann, and P. A. E. M. Janssen. *Dynamics and Modeling of Ocean Waves*. Cambridge, U.P. Cambridge, 1996.

[32] Alexander L. Fetter and John Dirk Walecka. *Theoretical Mechanics of Particles and Continua*. Dover, Mineola, NY, 1980.

[33] M. F. Hamilton and C. L. Morfey. *Model Equations*, chapter 3. Academic, New York, 1998.

[34] J. H. Ginsberg. *Perturbation Methods*, chapter 10. Academic, New York, 1998.

[35] Donald A. McQuarrie. *Mathematical Methods for Scientists and Engineers*. University Science Books, Herndon, VA, 2003.

[36] Sir Horace Lamb. *Hydrodynamics*. Dover, New York, NY, 6 edition, 1879.

[37] Roland B. Stull. *Meteorology for Scientists and Engineers*. Brooks/Cole, Pacific Grove, CA, 2000.

[38] H. Riehl. A model for hurricane formation. *J. Appl. Phys.*, 21:917–925, 1950.

[39] E. Kleinschmidt Jr. Gundlagen einer theorie des tropischen zyklonen. *Archiv fur Meteorologie, Geophysik, und Bioklimatologie*, 4:53–72, 1951.

[40] G.J. Holland. An analytic model of the wind and pressure profiles in a hurricane. *Mon. Weather Rev.*, 108:1212–1218, 1980.

[41] G.J. Holland. A revised model for radial profiles of hurricane winds. *Mon. Weather Rev.*, 136:3432–3445, 2010.

[42] Roger K. Smith. A simple model of the hurricane boundary layer. *Q. J. R. Meteorol. Soc.*, 129:1007–1027, 2003.

[43] H. E. Willoughby. *Mature Structure and Motion*. World Meteorological Organization, Geneva, 1995.

[44] J. S. Malkus and H. Riehl. On the dynamics and energy transformations in steady-state hurricanes. *Tellus*, 12:1–20, 1960.

[45] E. Mittelstaedt. The ocean boundary along the northwest african coast: Circulation and oceanographic properties of the sea surface. *Progress in Oceanography*, 26:307–355, 1991.

[46] R.G. Peterson, L. Stromma, and G. Kortum. Early concepts and charts of ocean circulation. *Progressing Oceanography*, 37:1–115, 1996.

[47] P.G. Franks, P.G. Bergmann, and A. Yaspan. Ray acoustics. *Summary Tech. Rept.*, pages 41–49 and 51–54 and 59–68, n.d.

[48] Finn B. Jensen, William A. Kuperman, Michael B. Porter, and Henrik Schmidt. *Computational Ocean Acoustics*. Sheridan Books, Ann Arbor, MI, 2000.

[49] Philip Blom and Roger Waxler. Impulse propagation in the nocturnal boundary layer: Analysis of the geometric component. *J. Acoust. Soc. Am.*, 131(5):3680 – 3690, 2012.

[50] J.R. Garratt. *The Atmospheric Boundary Layer*. Cambridge, New York, NY, 1992.

[51] Mark D. Powell. Evaluations of diagnostic marine boundary-layer models applied to hurricanes. *Monthly Weather Review*, 108:757–766, 1980.

[52] Peter G Black, Eric A D'Asaro, Thomas B Sanford, William M Drennan, Jun A Zhang, Jeffrey R French, Pearn P Niiler, Eric J Terrill, and Edward J Walsh. Air-sea exchange in hurricanes: Synthesis of observations from the coupled boundary layer air-sea transfer experiment. *Bulletin of the American Meteorological Society*, 88(3):357–374, 2007.

[53] William C Skamarock, Joseph B Klemp, Jimy Dudhia, David O Gill, Dale M Barker, Wei Wang, and Jordan G Powers. A description of the advanced research wrf version 2. Technical report, DTIC Document, 2005.

[54] DP Drob, JT Emmert, G Crowley, JM Picone, GG Shepherd, W Skinner, P Hays, RJ Niciejewski, M Larsen, CY She, et al. An empirical model of the earth's horizontal wind fields: Hwm07. *Journal of Geophysical Research: Space Physics (1978–2012)*, 113(A12), 2008.

[55] Jun A Zhang, William M Drennan, Peter G Black, and Jeffrey R French. Turbulence structure of the hurricane boundary layer between the outer rainbands. *Journal of the Atmospheric Sciences*, 66(8):2455–2467, 2009.

[56] Joseph F Lingevitch, Michael D Collins, and William L Siegmann. Parabolic equations for gravity and acousto-gravity waves. *The Journal of the Acoustical Society of America*, 105:304, 1999.

[57] Julius S. Bendat and Allan G. Piersol. *Random Data: Analysis and Measurement Procedures*. Wiley, 4 edition, 2010.

[58] Hamid Krim and Mats Viberg. Two decades of array signal processing research. *IEEE, Signal Processing Magazine*, 13(4):67 – 94, 1996.

[59] J. C. Samson. Descriptions of the polarization states of vector processes: applications to ulf magnetic fields. *Geophys. J. R. Astron. Soc.*, 34:403, 1973.

[60] John V. Olson. Noise suppression using data-adaptive polarization filters: applications to infrasonic array data. *J. Acoust. Soc. Am.*, 72(5):1456 – 1460, 1982.

[61] William H. Press, Saul A. Teukolsky, William T. Vetterling, and Brian P. Flannery. *Numerical Recipes in C++*. Cambridge, New York, NY, c++ edition, 1988.

[62] James W. Cooley and John. W. Tukey. An algorithm for the machine calculation of the complex fourier series. *Mathematics of Computation*, 19(90):297 – 301, 1965.

[63] G.C. Danielson and C. Lanczos. Some improvements in practical fourier analysis and their application to x-ray scattering from liquids. *J. Franklin. Inst.*, 233:365 – 380, 1942.

[64] Matteo Frigo and Steven G. Johnson. The fastest Fourier transform in the west. Technical Report MIT-LCS-TR-728, Massachusetts Institute of Technology, 1997.

[65] James A. Cadzow. Multiple source location - the signal subspace approach. *IEEE Trans. on Acoustics, Speech, and Sig. Proc.*, 1990.

[66] M. S. Bartlett. Smoothing periodograms from times series with continuous spectra. *Nature*, 161:686–687, 1948.

[67] J. Capon. High-resolution frequency-wavenumber spectrum analysis. *Proc. IEEE*, 57(8):1408 – 1418, 1969.

[68] R.T. Lacoss. Data adaptive spectral analysis methods. *Geophysics*, 36(4):661–675, 1971.

[69] B.D. Van Veen and K.M. Buckley. Beamforming: A versatile approach to spatial filtering. *IKKK ASSP Magazine*, pages 4–24, 1988.

[70] Ralph Schmidt. Multiple emitter location and signal parameter estimation. *Antennas and Propagation, IEEE Transactions on*, 34(3):276–280, 1986.

[71] Douglas A. Abraham and Norm L. Owsley. Beamforming with dominant mode rejection. *Proc. IEEE Oceans*, pages 470 – 475, 1990.

[72] Joseph E. Cavanaugh. Unifying the derivations for the akaike and corrected akaike information criteria. *Statistics and Probability Letters*, 33(2):201 – 208, 1999.

[73] S. Kullback and R.A. Leibler. On information and sufficiency. *The Annals of Mathematical Statistics*, 22(1):79–86, 1951.

[74] H. Akaike. *A new look at the statistical model identification*, volume AC-19, pages 267 – 281. 1974.

[75] Nariaki Sugiura. Further analysts of the data by akaike's information criterion and the finite corrections.

[76] Clifford M. Hurvich, Chih-Ling Tsai, and Jeffrey S. Simmonoff. Smoothing parameter selection in nonparametric regression using an improved akaike information criterion. *Jour. of the Royal Statistical Soc.*, 60:271–293, 1998.

[77] Y Kim and DL Jaggard. The fractal random array. *Proceedings of the IEEE*, 74(9):1278–1280, 1986.

[78] Rudolph Emil Kalman et al. A new approach to linear filtering and prediction problems. *Journal of basic Engineering*, 82(1):35–45, 1960.

[79] Richard J. Pasch and Todd B. Kimberlain. Tropical cyclone report - hurricane igor. Technical Report AL112020, National Hurricane Center, NOAA, February 2011.

[80] Lixion A. Avila and John P. Cangialosi. Tropical cyclone report - hurricane irene. Technical Report AL092011, National Hurricane Center, NOAA, December 2011.

[81] Stacy R. Stewar. Tropical cyclone report - hurricane katia. Technical Report AL122011, National Hurricane Center, NOAA, January 2012.

[82] Michael J Brennan. Tropical cyclone report - hurricane ophelia. Technical Report AL162011, National Hurricane Center, NOAA, December 2011.

[83] John P. Cangialosi. Tropical cyclone report - hurricane maria. Technical Report AL142011, National Hurricane Center, NOAA, January 2012.

[84] Allan D Pierce. Guided infrasonic modes in a temperature-and wind-stratified atmosphere. *J. Acoust. Soc. Am.*, 41(3):597–611, 1967.

[85] O. A. Godin. An effective quiescent medium for sound propagating through an inhomogeneous, moving fluid. *J. Acoust. Soc. Am.*, 112(4):1269 – 1275, 2002.

LIST OF APPENDICES

APPENDIX A: CALCULATING AMPLITUDES IN GEOMETRIC ACOUSTICS

APPENDIX A

CALCULATING AMPLITUDES IN GEOMETRIC ACOUSTICS

The amplitude coefficient $\mathcal{P}_0(\vec{x})$ can be found by taking the terms in Eq. (78) proportional to k_0.

$$\left(1-\frac{\vec{v}_0\cdot\vec{\nu}}{c_0}\right)\vec{\mathcal{V}}_1-\frac{1}{\rho_0 c_0}\mathcal{P}_1\vec{\nu}$$
$$=\frac{1}{c_0}\left[\vec{v}_0\cdot\vec{\nabla}\vec{\mathcal{V}}_0+\vec{\mathcal{V}}_0\cdot\vec{\nabla}\vec{v}_0+\frac{1}{\rho_0}\vec{\nabla}\mathcal{P}_0-\frac{\mathcal{D}_0}{{\rho_0}^2}\vec{\nabla}p_0\right]=\vec{b}, \tag{160a}$$

$$\left(1-\frac{\vec{v}_0\cdot\vec{\nu}}{c_0}\right)\mathcal{D}_1-\frac{\rho_0}{c_0}\vec{\nu}\cdot\vec{\mathcal{V}}_1=\frac{1}{c_0}\vec{\nabla}\cdot\left(\mathcal{D}_0\vec{v}_0+\rho_0\vec{\mathcal{V}}_0\right)=b_1, \tag{160b}$$

$$\mathcal{P}_1-c^2\mathcal{D}_1=\frac{1}{c\nu}\left[\vec{\mathcal{V}}_0\cdot\vec{\nabla}p_0+\vec{v}_0\cdot\vec{\nabla}\mathcal{P}_0-c^2\vec{v}_0\cdot\vec{\nabla}\mathcal{D}_0-\frac{\mathcal{P}_0}{c^2}\vec{v}_0\cdot\vec{\nabla}c^2-c^2\vec{\mathcal{V}}_0\cdot\vec{\nabla}\rho_0\right]=b_2, \tag{160c}$$

where $\mathcal{C}_0\vec{v}_0\cdot\vec{\nabla}\rho_0$ in Eq. (78) has been replaced by $\frac{\mathcal{P}_0}{c^2}\vec{v}_0\cdot\vec{\nabla}c^2$ [9]. Using Eq. (81), the left hand sides of these equations can be combined in a manner which goes to zero.

$$\begin{cases}\nu\vec{\mathcal{V}}_1-\frac{1}{\rho_0 c_0}\mathcal{P}_1\vec{\nu}=\vec{b}\\ \nu\mathcal{D}_1-\frac{\rho_0}{c_0}\vec{\nu}\cdot\vec{\mathcal{V}}_1=b_1\\ \mathcal{P}_1-c^2\mathcal{D}_1=b_2\end{cases}\quad\rightarrow\quad\frac{c_0\rho_0}{\nu}\vec{\nu}\cdot\vec{b}+c_0cb_1+\nu b_2=0. \tag{161}$$

Replacing $\vec{\mathcal{V}}_0$ and $\mathcal{D}_0$ with $\mathcal{P}_0$ from Eq. (79), each term can be calculated and simplified before

combining all three. One has,

$$\begin{aligned}
\frac{c_0\rho_0}{\nu}\vec{\nu}\cdot\vec{b} &= \frac{c_0\rho_0}{\nu}\vec{\nu}\cdot\frac{1}{c_0}\left[\vec{v}_0\cdot\vec{\nabla}\vec{\mathcal{V}}_0+\vec{\mathcal{V}}_0\cdot\vec{\nabla}\vec{v}_0+\frac{1}{\rho_0}\vec{\nabla}\mathcal{P}_0-\frac{\mathcal{D}_0}{{\rho_0}^2}\vec{\nabla}p_0\right]\\
&= \frac{\rho_0}{\nu}\vec{\nu}\cdot\left[\left(\vec{v}_0\cdot\vec{\nabla}\right)\left(\frac{\mathcal{P}_0}{\rho_0 c\nu}\vec{\nu}\right)+\frac{\mathcal{P}_0}{\rho_0 c\nu}\left(\vec{\nu}\cdot\vec{\nabla}\right)\vec{v}_0+\frac{1}{\rho_0}\vec{\nabla}\mathcal{P}_0-\frac{\mathcal{P}_0}{c^2{\rho_0}^2}\vec{\nabla}p_0\right]\\
&= \frac{\rho_0}{\nu}\vec{\nu}\cdot\left(\vec{v}_0\cdot\vec{\nabla}\right)\left(\frac{\mathcal{P}_0}{\rho_0 c\nu}\vec{\nu}\right)+\frac{\mathcal{P}_0}{c\nu^2}\vec{\nu}\cdot\left(\vec{\nu}\cdot\vec{\nabla}\right)\vec{v}_0+\frac{\vec{\nu}}{\nu}\cdot\vec{\nabla}\mathcal{P}_0-\frac{\mathcal{P}_0}{c^2\rho_0\nu}\vec{\nu}\cdot\vec{\nabla}p_0\\
&= \rho_0\nu\left(\vec{v}_0\cdot\vec{\nabla}\right)\left(\frac{\mathcal{P}_0}{\rho_0 c\nu}\right)+\frac{\mathcal{P}_0}{c\nu^2}\left[\vec{\nu}\cdot\left(\vec{v}_0\cdot\vec{\nabla}\right)\vec{\nu}+\vec{\nu}\cdot\left(\vec{\nu}\cdot\vec{\nabla}\right)\vec{v}_0\right]+\frac{\vec{\nu}}{\nu}\cdot\vec{\nabla}\mathcal{P}_0-\frac{\mathcal{P}_0}{c^2\rho_0\nu}\vec{\nu}\cdot\vec{\nabla}p_0\\
&= \rho_0\nu\left(\vec{v}_0\cdot\vec{\nabla}\right)\left(\frac{\mathcal{P}_0}{\rho_0 c\nu}\right)+\frac{\mathcal{P}_0}{c\nu^2}\vec{\nu}\cdot\vec{\nabla}\left(\vec{v}_0\cdot\vec{\nu}\right)+\frac{\vec{\nu}}{\nu}\cdot\vec{\nabla}\mathcal{P}_0-\frac{\mathcal{P}_0}{c^2\rho_0\nu}\vec{\nu}\cdot\vec{\nabla}p_0, \qquad (162a)
\end{aligned}$$

$$\begin{aligned}
c_0 c b_1 &= \frac{1}{c_0}\vec{\nabla}\cdot\left(\mathcal{D}_0\vec{v}_0+\rho_0\vec{\mathcal{V}}_0\right)\\
&= c\vec{\nabla}\left[\frac{\mathcal{P}_0}{c^2}\vec{v}_0+\frac{\mathcal{P}_0}{c\nu}\vec{\nu}\right]\\
&= c\vec{\nabla}\left[\frac{\mathcal{P}_0}{c^2}\left(\vec{v}_0+c\frac{\vec{\nu}}{\nu}\right)\right]\\
&= c\vec{\nabla}\left[\frac{\mathcal{P}_0}{c^2}\vec{c}_p\right]\\
&= \frac{1}{c}\vec{\nabla}\cdot\left(\mathcal{P}_0\vec{c}_p\right)+c\mathcal{P}_0\vec{c}_p\cdot\vec{\nabla}\frac{1}{c^2}, \qquad (162b)
\end{aligned}$$

$$\begin{aligned}
\nu b_2 &= \frac{1}{c}\left[\vec{\mathcal{V}}_0\cdot\vec{\nabla}p_0+\vec{v}_0\cdot\vec{\nabla}\mathcal{P}_0-c^2\vec{v}_0\cdot\vec{\nabla}\mathcal{D}_0-\frac{\mathcal{P}_0}{c^2}\vec{v}_0\cdot\vec{\nabla}c^2-c^2\vec{\mathcal{V}}_0\cdot\vec{\nabla}\rho_0\right]\\
&= \frac{1}{c}\left[\frac{\mathcal{P}_0}{\rho_0 c\nu}\vec{\nu}\cdot\vec{\nabla}p_0+\vec{v}_0\cdot\vec{\nabla}\mathcal{P}_0-c^2\vec{v}_0\cdot\vec{\nabla}\frac{\mathcal{P}_0}{c^2}-\frac{\mathcal{P}_0}{c^2}\vec{v}_0\cdot\vec{\nabla}c^2-c^2\frac{\mathcal{P}_0}{\rho_0 c\nu}\vec{\nu}\cdot\vec{\nabla}\rho_0\right]\\
&= \frac{\mathcal{P}_0}{\rho_0 c^2\nu}\vec{\nu}\cdot\vec{\nabla}p_0+\frac{1}{c}\vec{v}_0\cdot\vec{\nabla}\mathcal{P}_0-\frac{1}{c}\vec{v}_0\cdot\vec{\nabla}\mathcal{P}_0-\mathcal{P}_0 c\vec{v}_0\cdot\vec{\nabla}\frac{1}{c^2}-\frac{\mathcal{P}_0}{c^3}\vec{v}_0\cdot\vec{\nabla}c^2-\frac{\mathcal{P}_0}{\rho_0\nu}\vec{\nu}\cdot\vec{\nabla}\rho_0\\
&= \frac{\mathcal{P}_0}{\rho_0 c^2\nu}\vec{\nu}\cdot\vec{\nabla}p_0-\frac{\mathcal{P}_0}{c}\left[c^2\vec{v}_0\cdot\vec{\nabla}\frac{1}{c^2}+\frac{1}{c^2}\vec{v}_0\cdot\vec{\nabla}c^2\right]-\frac{\mathcal{P}_0}{\rho_0\nu}\vec{\nu}\cdot\vec{\nabla}\rho_0. \qquad (162c)
\end{aligned}$$

The last term in Eq. (162a) and the first term in Eq. (162c) cancel. Additionally the two terms in brackets in Eq. (162c) can be written in logarithm form

$$c^2\vec{v}_0\cdot\vec{\nabla}\frac{1}{c^2}+\frac{1}{c^2}\vec{v}_0\cdot\vec{\nabla}c^2=\vec{v}_0\cdot\nabla\left[\ln\frac{1}{c^2}+\ln c^2\right]=0.$$

Thus only the last term in νb_2 contributions. If the remaining terms are scaled by $c\mathcal{P}_0$,

$$\mathcal{P}_0\left(\vec{v}_0\cdot\vec{\nabla}\right)\mathcal{P}_0+\mathcal{P}_0^2\left(\rho_0 c\nu\right)\left(\vec{v}_0\cdot\vec{\nabla}\right)\left(\frac{1}{\rho_0 c\nu}\right)+\frac{\mathcal{P}_0^2}{\nu^2}\vec{\nu}\cdot\vec{\nabla}\left(\vec{v}_0\cdot\vec{\nu}\right)+\mathcal{P}_0 c\frac{\vec{\nu}}{\nu}\cdot\vec{\nabla}\mathcal{P}_0$$
$$+\mathcal{P}_0\vec{\nabla}\cdot\left(\mathcal{P}_0\vec{c}_p\right)+\mathcal{P}_0^2c^2\vec{c}_p\cdot\vec{\nabla}\frac{1}{c^2}-\frac{\mathcal{P}_0^2}{\rho_0}c\frac{\vec{\nu}}{\nu}\cdot\vec{\nabla}\rho_0=0. \tag{163}$$

Noting that $\vec{c}_p=\vec{v}_0+c\frac{\vec{\nu}}{\nu}$, the first and fourth terms combine to give $\mathcal{P}_0\left(\vec{c}_p\cdot\vec{\nabla}\right)\mathcal{P}_0$. The second, sixth, and seventh terms can all be written in logarithmic form.

$$\mathcal{P}_0^2\left(\rho_0 c\nu\right)\left(\vec{v}_0\cdot\vec{\nabla}\right)\left(\frac{1}{\rho_0 c\nu}\right)=-\mathcal{P}_0^2\vec{v}_0\cdot\nabla\ln\left(\rho_0 c\nu\right), \tag{164a}$$

$$\mathcal{P}_0^2c^2\vec{c}_p\cdot\vec{\nabla}\frac{1}{c^2}=-\mathcal{P}_0^2\vec{c}_p\cdot\vec{\nabla}\ln c^2, \tag{164b}$$

$$\frac{\mathcal{P}_0^2}{\rho_0}c\frac{\vec{\nu}}{\nu}\cdot\vec{\nabla}\rho_0=-\mathcal{P}_0^2c\frac{\vec{\nu}}{\nu}\cdot\vec{\nabla}\ln\rho_0. \tag{164c}$$

Finally, in the fourth term, $\vec{v}_0\cdot\vec{\nu}=\left(\vec{c}_p-c\frac{\vec{\nu}}{\nu}\right)\cdot\vec{\nu}=c_0-c\nu$, and therefore,

$$\begin{aligned}\frac{\mathcal{P}_0^2}{\nu^2}\vec{\nu}\cdot\vec{\nabla}\left(\vec{v}_0\cdot\vec{\nu}\right)&=\frac{\mathcal{P}_0^2}{\nu^2}\vec{\nu}\cdot\vec{\nabla}\left(c_0-c\nu\right)\\&=-\mathcal{P}_0^2c\frac{\vec{\nu}}{\nu}\cdot\vec{\nabla}\ln\left(c\nu\right).\end{aligned} \tag{164d}$$

By combining terms and writing all differentiation in terms of $\vec{c}_p\cdot\vec{\nabla}$,

$$\mathcal{P}_0\left(\vec{c}_p\cdot\vec{\nabla}\right)\mathcal{P}_0+\mathcal{P}_0\vec{\nabla}\cdot\left(\mathcal{P}_0\vec{c}_p\right)-\mathcal{P}_0^2\left(\vec{c}_p\cdot\vec{\nabla}\right)\ln\left(\rho_0c^3\nu\right)=0. \tag{165}$$

The first two terms here can be combined using $\mathcal{P}_0\vec{\nabla}\cdot\left(\mathcal{P}_0\vec{c}_p\right)=\nabla\cdot\left(\mathcal{P}_0^2\vec{c}_p\right)-\mathcal{P}_0\vec{c}_p\cdot\nabla\mathcal{P}_0$, resulting in the transport equation,

$$\vec{\nabla}\cdot\left(\mathcal{P}_0^2\vec{c}_p\right)=\mathcal{P}_0^2\vec{c}_p\cdot\vec{\nabla}\ln\left(\rho_0c^3\nu\right), \tag{166}$$

and the amplitude coefficient,

$$\mathcal{P}_0\left(s,\theta,\phi\right)=\mathcal{P}_0\left(0,\theta,\phi\right)\left|\frac{\rho_0\left(s\right)\nu\left(s\right)c^3\left(s\right)}{\rho_0\left(0\right)\nu\left(0\right)c^3\left(0\right)}\frac{c_p\left(0\right)D\left(0,\theta,\phi\right)}{c_p\left(s\right)D\left(s,\theta,\phi\right)}\right|^{\frac{1}{2}}, \tag{167}$$

where the angular dependences of ρ_0, ν, c, and c_p have been suppressed and $D\left(s,\theta,\phi\right)$ denotes the

Jacobian determinant describing the coordinate transformation from Cartesian (x, y, z) into ray coordinates (s, θ, ϕ). One can assumed spherical spreading near the source due to there being a constant sound speed for very small s. Thus, $P_0(s,\theta,\phi)|_{s\downarrow 0} = \frac{1}{4\pi s^2}$ and $D(s,\theta,\phi)|_{s\downarrow 0} = s^2\cos\theta$, which results in a coefficient of the form,

$$\mathcal{P}_0(s,\theta,\phi) = \frac{1}{4\pi}\left|\frac{\rho_0(s)\,\nu(s)\,c^3(s)}{\rho_0(0)\,\nu(0)\,c^3(0)}\frac{c_p(0)\cos\theta}{c_p(s)\,D(s,\theta,\phi)}\right|^{\frac{1}{2}}. \tag{168}$$

The Jacobian determinant is dependent on the variations in $\vec{x}$ with respect to changes in s, θ, and ϕ. Denoting $\frac{\partial}{\partial s} = \partial_s$, the determinant has the form,

$$\begin{aligned} D(s,\theta,\phi) = {} & \partial_s x\,(\partial_\theta y\,\partial_\phi z - \partial_\phi y\,\partial_\theta z) \\ & - \partial_\theta x\,(\partial_s y\,\partial_\phi z - \partial_\phi y\,\partial_s z) \\ & + \partial_\phi x\,(\partial_s y\,\partial_\theta z - \partial_\theta y\,\partial_s z). \end{aligned} \tag{169}$$

The s derivatives are easily obtained using Eq. (85), however, the angular derivatives are more difficult to calculate. Consider defining auxiliary variables which are the angular derivatives $\frac{\partial\vec{x}}{\partial(\measuredangle)} = \vec{\mathcal{X}}^{(\measuredangle)}$ and $\frac{\partial\vec{\nu}}{\partial(\measuredangle)} = \vec{\mu}^{(\measuredangle)}$. Then, we can determine how such variables vary along a ray path by taking the angular derivatives of Eq. (85). Presented here is the θ derivative for $\vec{x}$ and $\vec{\nu}$, the ϕ derivative is identical.

Taking the θ derivative of Eq. (85) and exchanging the order of operations gives,

$$\frac{\partial\vec{\mathcal{X}}^{(\theta)}}{\partial s} = \frac{\partial}{\partial\theta}\left(\frac{\vec{c}_p}{c_p}\right), \qquad \frac{\partial\vec{\mu}^{(\theta)}}{\partial s} = \frac{\partial}{\partial\theta}\left(-\frac{1}{c_p}\left[\nu\frac{\partial c}{\partial x_i} + \sum_{j=1}^{3}\nu_j\frac{\partial v_{0,j}}{\partial x_i}\right]\right). \tag{170}$$

The magnitude of c_p can be expressed as $c_p = c\sqrt{\sum_{j=1}^{3}\left(\frac{v_{0,j}}{c} + \frac{\nu_j}{\nu}\right)^2}$ and we can simplify notation by defining $\mathcal{C}_p^{(\theta)} = \frac{\partial c_p}{\partial\theta}$. Derivatives with respect to θ can be performed using the chain rule, $\frac{\partial}{\partial\theta} = \left(\partial_\theta\vec{x}\cdot\vec{\nabla}\right)$. Consider first the position equation,

$$\begin{aligned} \frac{\partial\vec{\mathcal{X}}^{(\theta)}}{\partial s} &= -\frac{\vec{c}_p}{{c_p}^2}\frac{\partial c_p}{\partial\theta} + \frac{1}{c_p}\left(\frac{\partial\vec{v}_0}{\partial\theta} + \frac{\partial}{\partial\theta}\left(\frac{c}{\nu}\vec{\nu}\right)\right) \\ &= -\frac{\vec{c}_p}{{c_p}^2}\mathcal{C}_p^{(\theta)} + \frac{1}{c_p}\left[\frac{\partial\vec{v}_0}{\partial\theta} + \frac{\vec{\nu}}{\nu}\frac{\partial c}{\partial\theta} + c\frac{\partial}{\partial\theta}\frac{\vec{\nu}}{\nu}\right]. \end{aligned} \tag{171}$$

Thus all that remains is to calculate $\frac{\partial}{\partial\theta}\frac{\vec{\nu}}{\nu}$ and $\mathcal{C}_p^{(\theta)}$. Some simple manipulation produces,

$$\begin{aligned}\frac{\partial}{\partial\theta}\frac{\vec{\nu}}{\nu} &= \frac{\vec{\mu}^{(\theta)}}{\nu} - \frac{\vec{\nu}}{\nu^2}\frac{\partial}{\partial\theta}\sqrt{\sum_{j=1}^{3}{\nu_j}^2} \\ &= \frac{\partial_\theta\vec{\nu}}{\nu} - \frac{\vec{\nu}}{2\nu^3}\left(\sum_{j=1}^{3}2\nu_j\frac{\partial\nu_j}{\partial\theta}\right) \\ &= \frac{\partial_\theta\vec{\nu}}{\nu} - \frac{\vec{\nu}}{\nu^2}\frac{\vec{\nu}\cdot\vec{\mu}^{(\theta)}}{\nu} = \frac{\partial_\theta\vec{\nu}}{\nu} - \frac{\vec{\nu}}{\nu^2}\frac{\partial\nu}{\partial\theta}.\end{aligned} \tag{172}$$

Note that in the last term we've used the shortened form, $\frac{\partial\nu}{\partial\theta} = \frac{\vec{\nu}\cdot\vec{\mu}^{(\theta)}}{\nu}$. The derivative of the propagation velocity is more complicated,

$$\begin{aligned}\frac{\partial c_p}{\partial\theta} &= \sqrt{\sum_{j=1}^{3}\left(\frac{v_{0,j}}{c}+\frac{\nu_j}{\nu}\right)^2}\frac{\partial c}{\partial\theta} + c\frac{\partial}{\partial\theta}\sqrt{\sum_{j=1}^{3}\left(\frac{v_{0,j}}{c}+\frac{\nu_j}{\nu}\right)^2} \\ &= \frac{c_p}{c}\frac{\partial c}{\partial\theta} + \frac{c}{2}\left(\sum_{j=1}^{3}\left(\frac{v_{0,j}}{c}+\frac{\nu_j}{\nu}\right)^2\right)^{-\frac{1}{2}}\sum_{j=1}^{3}\frac{\partial}{\partial\theta}\left(\frac{v_{0,j}}{c}+\frac{\nu_j}{\nu}\right)^2 \\ &= \frac{c_p}{c}\frac{\partial c}{\partial\theta} + \frac{c^2}{2c_p}\sum_{j=1}^{3}\left[2\left(\frac{v_{0,j}}{c}+\frac{\nu_j}{\nu}\right)\left(\frac{\partial}{\partial\theta}\frac{v_{0,j}}{c}+\frac{\partial}{\partial\theta}\frac{\nu_j}{\nu}\right)\right] \\ &= \frac{c_p}{c}\frac{\partial c}{\partial\theta} + \frac{c}{c_p}\sum_{j=1}^{3}\left(v_{0,j}+c\frac{\nu_j}{\nu}\right)\left(\frac{1}{c}\frac{\partial v_{0,j}}{\partial\theta} - \frac{v_{0,j}}{c^2}\frac{\partial c}{\partial\theta} + \frac{\partial_\theta\nu_j}{\nu} - \frac{\nu_j}{\nu^2}\frac{\partial\nu}{\partial\theta}\right).\end{aligned} \tag{173}$$

And so finally, the propagation velocity derivative can be expressed by,

$$\mathcal{C}_p^{(\theta)} = \frac{c_p}{c}\left[\frac{\partial c}{\partial\theta} + \frac{c^2}{c_p^2}\vec{c}_p\cdot\left(\frac{1}{c}\frac{\partial\vec{v}_0}{\partial\theta} - \frac{\vec{v}_0}{c^2}\frac{\partial c}{\partial\theta} + \frac{\partial_\theta\vec{\nu}}{\nu} - \frac{\vec{\nu}}{\nu^2}\frac{\partial\nu}{\partial\theta}\right)\right]. \tag{174}$$

The same operations can be performed on the momentum equation,

$$\frac{\partial\mu_i^{(\theta)}}{\partial s} = \frac{1}{{c_p}^2}\frac{\partial c_p}{\partial\theta}\left(\nu\frac{\partial c}{\partial x_i} + \sum_{j=1}^{3}\nu_j\frac{\partial v_{0,j}}{\partial x_i}\right) - \frac{1}{c_p}\frac{\partial}{\partial\theta}\left(\nu\frac{\partial c}{\partial x_i} + \sum_{j=1}^{3}\nu_j\frac{\partial v_{0,j}}{\partial x_i}\right). \tag{175}$$

The first term can be expressed in terms of $\mathcal{C}_p^{(\theta)}$. The second term requires some additional manip-

ulation,

$$\frac{\partial}{\partial\theta}\left(\nu\frac{\partial c}{\partial x_i}+\sum_{j=1}^{3}\nu_j\frac{\partial v_{0,j}}{\partial x_i}\right)=\frac{\partial\nu}{\partial\theta}\frac{\partial c}{\partial x_i}+\nu\frac{\partial^2 c}{\partial\theta\partial x_i}+\sum_{j=1}^{3}\left(\partial_\theta\nu_j\frac{\partial v_{0,j}}{\partial x_i}+\nu_j\frac{\partial^2 v_{0,j}}{\partial\theta\partial x_i}\right). \tag{176}$$

And so the resulting momentum equation can be written as

$$\begin{aligned}\frac{\partial\mu_i^{(\theta)}}{\partial s}=\frac{\mathcal{C}_p^{(\theta)}}{{c_p}^2}\left(\nu\frac{\partial c}{\partial x_i}+\vec{\nu}\cdot\frac{\partial\vec{v}_0}{\partial x_i}\right)\\ -\frac{1}{c_p}\left[\frac{\partial\nu}{\partial\theta}\frac{\partial c}{\partial x_i}+\nu\frac{\partial^2 c}{\partial\theta\partial x_i}+\vec{\mu}^{(\theta)}\cdot\frac{\partial\vec{v}_0}{\partial x_i}+\vec{\nu}\cdot\frac{\partial^2\vec{v}_0}{\partial\theta\partial x_i}\right].\end{aligned} \tag{177}$$

To summarize, the system of equations in Eq. (85) can be expanded to include,

$$\frac{\partial\vec{\mathcal{X}}^{(\measuredangle)}}{\partial s}=-\frac{\vec{c}_p}{{c_p}^2}\mathcal{C}_p^{(\measuredangle)}+\frac{1}{c_p}\left[\frac{\partial\vec{v}_0}{\partial\left(\measuredangle\right)}+\frac{\vec{\nu}}{\nu}\frac{\partial c}{\partial\left(\measuredangle\right)}+c\left(\frac{\vec{\mu}^{(\measuredangle)}}{\nu}-\frac{\vec{\nu}}{\nu^2}\frac{\partial\nu}{\partial\left(\measuredangle\right)}\right)\right], \tag{178a}$$

$$\begin{aligned}\frac{\partial\mu_i^{(\measuredangle)}}{\partial s}=\frac{\mathcal{C}_p^{(\measuredangle)}}{{c_p}^2}\left(\nu\frac{\partial c}{\partial x_i}+\vec{\nu}\cdot\frac{\partial\vec{v}_0}{\partial x_i}\right)\\ -\frac{1}{c_p}\left[\frac{\partial\nu}{\partial(\measuredangle)}\frac{\partial c}{\partial x_i}+\nu\frac{\partial^2 c}{\partial(\measuredangle)\partial x_i}+\vec{\mu}^{(\measuredangle)}\cdot\frac{\partial\vec{v}_0}{\partial x_i}+\vec{\nu}\cdot\frac{\partial^2\vec{v}_0}{\partial(\measuredangle)\partial x_i}\right].\end{aligned} \tag{178b}$$

where $\measuredangle=\theta,\phi$, $\mathcal{C}_p^{(\measuredangle)}$ is given in Eq. (174), $\frac{\partial\nu}{\partial(\measuredangle)}=\frac{\vec{\nu}\cdot\partial_{(\measuredangle)}\vec{\nu}}{\nu}$, and angular derivatives are taken by $\frac{\partial}{\partial(\measuredangle)}=\left(\vec{\mathcal{X}}^{(\measuredangle)}\cdot\vec{\nabla}\right)$. The results of this system can be used with Eq. (169) to compute the transfer function, Eq. (168), along each geometric ray path in three dimensions.

Initializing and Reflecting Ray Paths in Three-Dimensions

The initial conditions for the angular derivative can be found by differentiating Eq. (87) and (91) with respect to θ and ϕ. One obtains,

$$\vec{\mathcal{X}}^{(\theta)}=\vec{\mathcal{X}}^{(\phi)}=\begin{pmatrix}0\\0\\0\end{pmatrix}, \tag{179a}$$

$$\vec{\mu}^{(\theta)}(0,\theta,\phi) = \frac{\partial}{\partial\theta}\vec{\nu}(0,\theta,\phi) = \begin{pmatrix} -\sin\theta\cos\phi \\ -\sin\theta\sin\phi \\ \cos\theta \end{pmatrix}, \tag{179b}$$

$$\vec{\mu}^{(\phi)}(0,\theta,\phi) = \frac{\partial}{\partial\phi}\vec{\nu}(0,\theta,\phi) = \begin{pmatrix} -\cos\theta\sin\phi \\ \cos\theta\cos\phi \\ \sin\theta \end{pmatrix}. \tag{179c}$$

The reflection conditions can also be derived in a similar fashion as to those in Chapter 3. However, let's consider first the simpler 2D case in which we write Eq. (92) instead in terms of the arrival range r and altitude z,

$$\begin{pmatrix} r(s,\theta) \\ z(s,\theta) \end{pmatrix} = \begin{pmatrix} r_0(\theta) + (s - s_0(\theta))\cos\theta_{\text{ref}} + O\left([s - s_0(\theta)]^2\right) \\ |s - s_0(\theta)|\sin\theta_{\text{ref}} + O\left([s - s_0(\theta)]^2\right) \end{pmatrix}. \tag{180}$$

We can use the auxiliary parameter $\mathcal{R}^{(\theta)} = \frac{\partial r}{\partial\theta}$ to determine the reflection behavior of $\mathcal{X}^{(\theta)}$ and $\mathcal{Y}^{(\theta)}$. One finds,

$$\begin{aligned} \mathcal{R}^{(\theta)}\left(s_0 + 0^+, \theta\right) &= \frac{\partial}{\partial\theta}\left(r_0(\theta) + (s - s_0(\theta))\cos\theta_{\text{ref}}\right) + O(s - s_0(\theta)) \\ &= \mathcal{R}_0(\theta) + \frac{\partial r}{\partial s}\Big|_{s_0}\frac{\partial s_0}{\partial\theta} - \frac{\partial s_0}{\partial\theta}\cos\theta_{\text{ref}} + O(s - s_0). \end{aligned} \tag{181}$$

Simple geometric analysis shows that in the case that $\vec{v}_0(x,y,0) = 0$, $\frac{\partial r}{\partial s}\Big|_{s_0} = \cos\theta_{\text{ref}}$ and therefore $\mathcal{R}^{(\theta)}$ is continuous across the reflection. From this result we can infer that $\mathcal{X}^{(\theta)}$ and $\mathcal{Y}^{(\theta)}$ are also continuous across the reflection in three dimensions.

Repeating this differentiation on $z(s,\theta)$,

$$\begin{aligned} \mathcal{Z}^{(\theta)}\left(s_0 + 0^+, \theta\right) &= \frac{\partial}{\partial\theta}\left(|s - s_0(\theta)|\sin\theta_{\text{ref}}\right) + O(s - s_0(\theta)) \\ &= -\frac{\partial s_0}{\partial\theta}\sin\theta_{\text{ref}} + O(s - s_0(\theta)). \end{aligned} \tag{182}$$

As in Reference [49], quantities associated with the intercept of the incident ray path and can be defined by the location at which the incident ray path meets the ground, $z_0(\theta,\phi) = z(s_0(\theta,\phi),\theta,\phi) =$

0. Differentiating the intercept condition with respect to $(\measuredangle) = \theta$ or ϕ,

$$\begin{aligned}\frac{dz_0}{d(\measuredangle)} &= \frac{\partial z}{\partial(\measuredangle)}\Big|_{s_0} + \frac{\partial z}{\partial s}\Big|_{s_0}\frac{\partial s_0}{\partial(\measuredangle)} \\ &= \mathcal{Z}_0^{(\measuredangle)} + \nu_{z0}\frac{\partial s_0}{\partial(\measuredangle)} = 0,\end{aligned} \tag{183}$$

and it can immediately be seen,

$$\frac{\partial s_0}{\partial(\measuredangle)} = -\frac{\mathcal{Z}_0^{(\measuredangle)}}{\nu_{z0}} = \frac{\mathcal{Z}_0^{(\measuredangle)}}{\sin\theta_{\text{ref}}}. \tag{184}$$

where we've used the result from Eq. (93a) to write $\nu_{z,0}$ in terms of θ_{ref}. From this result it is immediately clear that $\mathcal{Z}_0^{(\theta)}$ is discontinuous by a change in sign across the reflection. It is straight forward to extend the above results for the three dimensional case and show that,

$$\mathcal{X}^{(\measuredangle)}\left(s_0 + 0^+, \theta, \phi\right) = \mathcal{X}_0^{(\measuredangle)}, \qquad \mathcal{Y}^{(\measuredangle)}\left(s_0 + 0^+, \theta, \phi\right) = \mathcal{Y}_0^{(\measuredangle)},$$

$$\mathcal{Z}^{(\measuredangle)}\left(s_0 + 0^+, \theta, \phi\right) = -\mathcal{Z}_0^{(\measuredangle)}. \tag{185}$$

This leaves the reflection relations for $\vec{\mu}^{(\measuredangle)}$ to determine. Consider one element of this vector,

$$\begin{aligned}\mu_j\left(s_0 + 0^+, \theta, \phi\right) &= \frac{\partial}{\partial\left(\measuredangle\right)}\nu_{j,0} + \frac{\partial \nu_j}{\partial s}\Big|_{s_0}\frac{\partial s_0}{\partial\left(\measuredangle\right)} \\ &= \frac{\partial}{\partial\left(\measuredangle\right)}\left(\frac{c_0}{c}\frac{\partial r_j}{\partial s}\right)_{s_0} - \frac{\partial \nu_j}{\partial s}\Big|_{s_0}\frac{\mathcal{Z}_0^{(\measuredangle)}}{\nu_{z,0}} \\ &= -\frac{c_0}{c^2}\frac{\partial c}{\partial\left(\measuredangle\right)}\frac{\partial r_j}{\partial s}\Big|_{s_0} + \frac{c_0}{c}\frac{\partial^2 r_j}{\partial s \partial\left(\measuredangle\right)} - \frac{\partial \nu_j}{\partial s}\Big|_{s_0}\frac{\mathcal{Z}_0^{(\measuredangle)}}{\nu_{z,0}}.\end{aligned}$$

In the first term, $\frac{\partial c}{\partial(\measuredangle)}$ can be expanded into,

$$\frac{\partial c}{\partial\left(\measuredangle\right)} = \frac{\partial \vec{x}}{\partial\left(\measuredangle\right)}\cdot\vec{\nabla}c = \frac{\partial \vec{x}_\perp}{\partial\left(\measuredangle\right)}\Big|_{s_0}\cdot\vec{\nabla}_\perp c + \frac{\partial z}{\partial(\measuredangle)}\Big|_{s_0}\frac{\partial c}{\partial z}, \tag{186}$$

and since this result is calculated at s_0 where the ray intercepts the ground, we have $\frac{\partial z}{\partial(\measuredangle)}\Big|_{s_0} = 0$. Further, by our choice of propagation medium description, we've defined c such that $c\left(x, y, 0\right)$ is

constant and therefore the other term is also zero. Thus, the first term in this result does not contribute.

The factor $\frac{c_0}{c}$ goes to unity at the reflection surface and therefore we are left with

$$\mu_j\left(s_0+0^+,\theta,\phi\right)=\frac{\partial^2 r_j}{\partial s\partial\left(\measuredangle\right)}+\frac{\partial\nu_j}{\partial s}\Big|_{s_0}\frac{\mathcal{Z}_0^{(\measuredangle)}}{\nu_{z,0}}. \tag{187}$$

In the first term, one has $\frac{\partial}{\partial(\measuredangle)}\frac{\partial r_j}{\partial s}\Big|_{s_0}$ which we can evaluate for each component of j and each angle ϕ. However, it is more beneficial at this point to return to the 2D results. Consider,

$$\frac{\partial r}{\partial s}\Big|_{s_0}=\cos\theta_{\text{ref}}\quad\rightarrow\quad\frac{\partial}{\partial\theta}\frac{\partial r}{\partial s}=-\sin\theta_{\text{ref}}\frac{\partial\theta_{\text{ref}}}{\partial\theta}, \tag{188a}$$

$$\frac{\partial z}{\partial s}\Big|_{s_0}=\sin\theta_{\text{ref}}\quad\rightarrow\quad\frac{\partial}{\partial\theta}\frac{\partial z}{\partial s}=\cos\theta_{\text{ref}}\frac{\partial\theta_{\text{ref}}}{\partial\theta}, \tag{188b}$$

where,

$$\theta_{\text{ref}}=-\text{asin}\ \nu_{z,0}=\text{acos}\ \nu_{r,0}.$$

The derivative $\frac{\partial\theta_{\text{ref}}}{\partial\theta}$ can be evaluated using the relations between θ_{ref} and $\vec{\nu}$. One finds,

$$\begin{aligned}\frac{\partial\theta_{\text{ref}}}{\partial\theta}&=\frac{\partial}{\partial\theta}\left(-\text{asin}\ \nu_{z,0}\right)=-\frac{1}{\sqrt{1-\nu_{z,0}^2}}\frac{\partial\nu_{z,0}}{\partial\theta}\Big|_{s_0}\\&=-\frac{1}{\sqrt{1-\nu_{z,0}^2}}\left(\mu_{z,0}+\frac{\partial\nu_z}{\partial s}\Big|_{s_0}\frac{\partial s_0}{\partial\theta}\right),\end{aligned} \tag{189a}$$

$$\begin{aligned}\frac{\partial\theta_{\text{ref}}}{\partial\theta}&=\frac{\partial}{\partial\theta}\left(\text{acos}\ \nu_{r,0}\right)=\frac{1}{\sqrt{1-\nu_{r,0}^2}}\frac{\partial\nu_{r,0}}{\partial\theta}\Big|_{s_0}\\&=\frac{1}{\sqrt{1-\nu_{r,0}^2}}\left(\mu_{r,0}+\frac{\partial\nu_r}{\partial s}\Big|_{s_0}\frac{\partial s_0}{\partial\theta}\right).\end{aligned} \tag{189b}$$

And so finally,

$$\frac{\partial}{\partial\theta}\frac{\partial r}{\partial s} = -\sin\theta\frac{\partial\theta_{\text{ref}}}{\partial\theta} = \frac{\nu_{z,0}}{\sqrt{1-\nu_{r,0}^2}}\left(\mu_{r,0} + \frac{\partial\nu_r}{\partial s}\Big|_{s_0}\frac{\partial s_0}{\partial\theta}\right)$$
$$= \frac{\sqrt{1-\nu_{r,0}^2}}{\sqrt{1-\nu_{r,0}^2}}\left(\mu_{r,0} + \frac{\partial\nu_r}{\partial s}\Big|_{s_0}\frac{\partial s_0}{\partial\theta}\right), \tag{190}$$

and similarly,

$$\frac{\partial}{\partial\theta}\frac{\partial z}{\partial s} = -\frac{\sqrt{1-\nu_{z,0}^2}}{\sqrt{1-\nu_{z,0}^2}}\left(\mu_{z,0} + \frac{\partial\nu_z}{\partial s}\Big|_{s_0}\frac{\partial s_0}{\partial\theta}\right). \tag{191}$$

Because $\frac{\partial\nu_r}{\partial s} \propto \frac{\partial c}{\partial r}$ is zero at the reflection point, this produces the result that $\mu_r^{(\theta)}$ must be continuous across a reflection. Therefore $\mu_x^{(\measuredangle)}$ and $\mu_y^{(\measuredangle)}$ must be continuous across a reflection point. The remaining reflection conditions on $\mu_z^{(\measuredangle)}$ require one last bit of analysis to correctly derive. In calculating $\frac{\partial\theta_{\text{ref}}}{\partial\theta}$, we are interested in the incident values of the quantities. Because ν_z and $\mathcal{Z}$ change sign in the reflection and these terms behave as $\frac{\partial\nu_z}{\partial s}\frac{\mathcal{Z}_0}{\nu_z}$, the contributions add together instead of canceling and one finds,

$$\mu_z^{(\measuredangle)}\left(s_0 + 0^+, \theta, \phi\right) = -\mu_{z,0}^{(\measuredangle)} - \frac{2}{c_0}\frac{\partial c_0}{\partial z}\frac{\mathcal{Z}_0^{(\measuredangle)}}{\nu_{z,0}}. \tag{192}$$

Thus, $\mu_z^{(\measuredangle)}$ changes sign in the reflection, but picks up additional change due to the gradient of the sound speed profile at the ground. Using these boundary conditions, geometric ray paths and geometric attenuation can be calculated for any propagation medium for which $c\,(x, y, 0)$ is a constant and $\vec{v}\,(x, y, 0)$ goes to zero.

APPENDIX B: AN ASIDE ON THE EFFICIENCY OF THE BOUNDARY LAYER DUCT

APPENDIX B

AN ASIDE ON THE EFFICIENCY OF THE BOUNDARY LAYER DUCT

It was mentioned in Chapter 3 that the physical characteristics of the duct in the boundary layer could produce errors in the predictions of geometric acoustics. This is due to a combination of the large wind gradient near the ocean surface and the limited vertical extent of the duct. In order for geometric acoustics to accurately describe the propagation, the refractive index must satisfy,

$$\lambda_0 \, \hat{n}_\nu \cdot \vec{\nabla} \, n \, (\vec{x}) \ll 1 \quad \rightarrow \quad \hat{n}_\nu \cdot \vec{\nabla} \, n \, (\vec{x}) \ll \frac{f}{c_0} = \frac{0.2 \text{ Hz}}{0.34 \frac{\text{km}}{\text{s}}} = 0.588 \text{ km}^{-1},$$

which is not guaranteed to be true for the vertical wind gradients in the boundary layer of the storm. Additionally, the wind increase from zero at the ocean surface to their maximum at approximately 1-2 kilometers altitude [37]. This results in a vertically thin acoustic duct which limits the number of modes interacting strongly with the storm winds in the boundary layer. Because of this, geometric acoustics overestimates the efficiency with which the duct traps energy in the boundary layer. As the sound propagates through this duct, some fraction of the energy may leak out and therefore not be refracted by the horizontal wind gradients.

Developing A Full Wave Solution

In this section, the mathematical basis of a modal expansion for propagation in an atmosphere with stratified temperature and horizontal winds is reviewed [84, 8, 9]. The wave equation for sound propagating in a stratified medium can be solved using horizontal eigenvalue expansion in the horizontal wave number, $k_\perp$. Consider the wave equation for propagation using the effective

sound speed approximation,

$$\left[\nabla_\perp^2 + \rho_0 \frac{\partial}{\partial z}\frac{1}{\rho_0}\frac{\partial}{\partial z} + \frac{\omega^2}{c_{\text{eff}}^2}\right]\hat{p}\left(\vec{x},\omega\right) = 0, \tag{193}$$

where ρ_0 and c_{eff} are functions only of z and $c_{\text{eff}} = c + \vec{v}_0 \cdot \hat{n}_{k_\perp}$ is the effective sound speed defined by the sum of the thermodynamic sound speed with the wind in the direction of propagation [85]. In such a case, one can expand in horizontal wavenumber,

$$\left[\frac{d^2}{dz^2} + \mathcal{F}\left(\rho_0\right) + \frac{\omega^2}{c_{\text{eff}}^2(z)} - k_j^2\right]\tilde{p}_j\left(z\right) = 0, \qquad \hat{p}\left(\vec{x},\omega\right) = \sum_j \frac{\tilde{p}_j\left(z\right)}{\sqrt{\rho_0}} H_0^{(+)}\left(k_j r\right), \tag{194}$$

where we've used a cylindrical expansion but kept only zeroth order outgoing Hankel function, $H_0^{(+)}\left(k_j r\right)$, because of the azimuthal symmetry. The function $\mathcal{F}$ is a result of changing $\hat{p} \to \frac{\tilde{p}}{\sqrt{\rho_0}}$ in order to remove the first order derivative term and has the form,

$$\mathcal{F}\left(\rho_0\right) = \frac{1}{2}\frac{\rho_0''}{\rho_0} - \frac{3}{4}\frac{\rho_0'^2}{\rho_0^2}. \tag{195}$$

The resulting one dimensional eigenfunction problem can be solved numerically by solving the eigenvector equation,

$$\boldsymbol{M}\vec{\tilde{p}}_j\left(z\right) = k_j^2\vec{\tilde{p}}_j\left(z\right), \qquad \boldsymbol{M} = \boldsymbol{D}_2 + \left[\mathcal{F}\left(\rho_0\right) + \frac{\omega^2}{c_{\text{eff}}^2(z)}\right]\boldsymbol{I}, \tag{196}$$

where $\boldsymbol{D}_2$ is the matrix operator which produces the discrete second derivative and $\vec{\tilde{p}}_j$ is a vector of the pressure at discrete altitude steps,

$$\vec{\tilde{p}}_j = \begin{pmatrix} \tilde{p}_j(0) \\ \tilde{p}_j(\delta z) \\ \tilde{p}_j(2\delta z) \\ \vdots \\ \tilde{p}_j(N\delta z) \end{pmatrix}, \qquad \boldsymbol{D}_2 = \frac{1}{\delta z^2}\begin{pmatrix} \mathcal{B} & 1 & 0 & 0 & \cdots \\ 1 & -2 & 1 & 0 & \cdots \\ 0 & 1 & -2 & 1 & \cdots \\ \vdots & \vdots & \vdots & \vdots & \ddots \end{pmatrix}. \tag{197}$$

In this last matrix, $\mathcal{B}$ is determined by the boundary condition at the ground, $\left.\frac{\partial\hat{p}}{\partial z}\right|_{z=0} = 0$, which

requires $\mathcal{B} = \frac{1}{1+\frac{\delta z}{2}\frac{\rho_0'}{\rho_0}} - 2$.

Propagation Through the Atmosphere Around a Large Maritime Storm

The propagation scheme discussed above is valid only for an atmosphere which is independent of range. Therefore, we have chosen to use the vertically varying atmosphere at a single point within the storm. For this analysis, we've chosen to examine the ducting at the radius of maximum winds directly east of the eye column. The effective sound speed profiles at this point for propagation north and west in such at atmosphere are shown in the left-most panel of Figure 41. The red line in the figure is for westward propagation and the blue is that for northward. The wind field alone are shown in the other panel on the left. Shown in this figure is a category 3 storm with maximum winds of 55 $\frac{\text{m}}{\text{s}}$, a surface roughness of 10 m, and a westward directed stratospheric jet with speed 60 $\frac{\text{m}}{\text{s}}$.

The right side of Figure 39 shows the transmission loss for propagation at various azimuths though this atmosphere. Unlike the geometric analysis, the source is located at the origin for this plot. Directly to the west of the source, the stratospheric jet produces the expected ducting for a stratospheric duct. The energy reaching the ground to the south is the result of the strong decrease

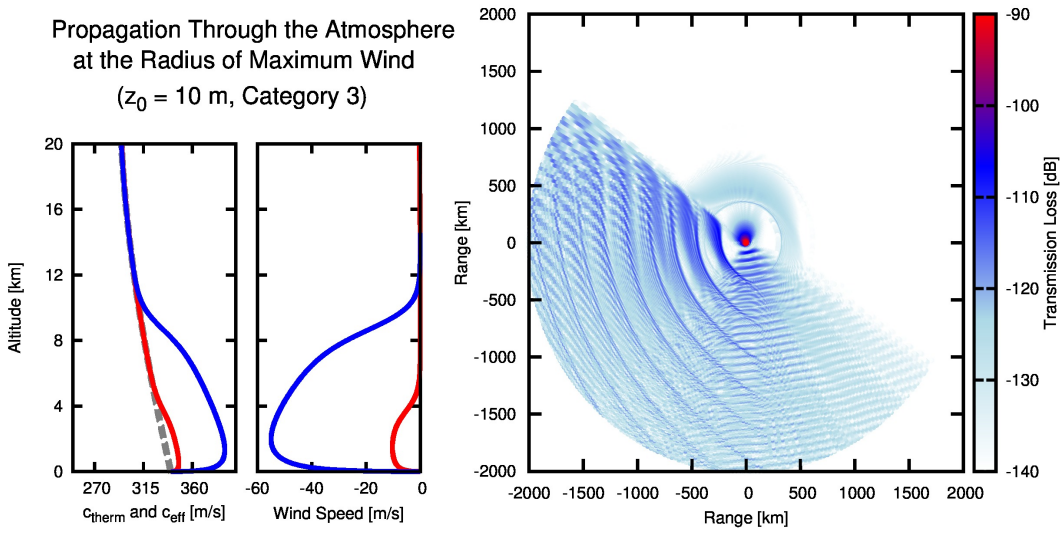

Fig. 39: The effective sound speed profiles (left) and arrival field (right) for propagation through the atmosphere at the radius of maximum winds in a direction east of the eye column of a Category 3 storm with boundary layer surface roughness of 10 meters.

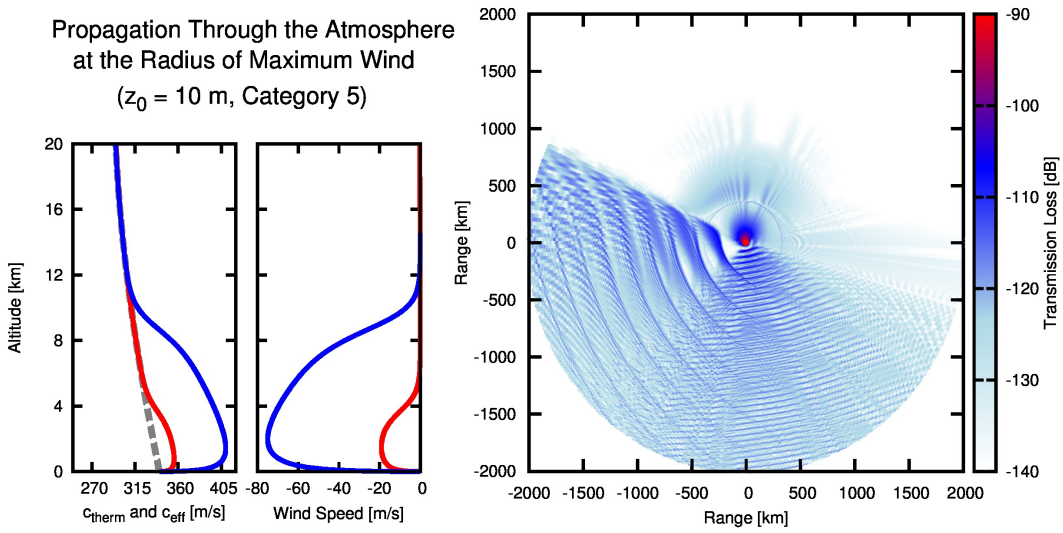

Fig. 40: The effective sound speed profiles (left) and arrival field (right) for propagation through the atmosphere at the radius of maximum winds in a direction east of the eye column of a Category 5 storm with boundary layer surface roughness of 10 meters.

in winds at the top of the storm in the troposphere. Within a few hundred kilometers of the source, ducting is observed in the direction of the storm winds (northward), however the duct is leaky and the energy is no longer contained within a propagation distance of a few hundred kilometers.

In the case of a stronger storm, it can be expected that the larger magnitude of the winds will increase the duct's efficiency. In Fig. 40, the overall storm intensity has been increased to that of a Category 5 storm, with a maximum wind speed of 75 $\frac{\text{m}}{\text{s}}$. The ducting to the north of the storm is much more effective and energy is contained in the boundary layer to a range of over 1,000 kilometers. In this case, one would expect a majority of the energy which enters the duct in the boundary layer to propagate through the storm winds in the boundary layer and produce the refraction effects predicted in Chapter 3.

In addition to variations in storm intensity, it was mentioned in Chapter 3 that the surface roughness could be larger than the 10 m used in the above examples. As an example of how the duct would be modified for a weaker wind gradient at the ocean surface, consider the result of Fig. 41. In this case, the strength of the storm has been left at a Category 3, while the surface roughness in the boundary layer has been increased to 100 m. It is immediately obvious that in this case the duct becomes more efficient and a large fraction of the energy will remain in the storm boundary layer and as a result be strongly refracted by the horizontal wind gradients.

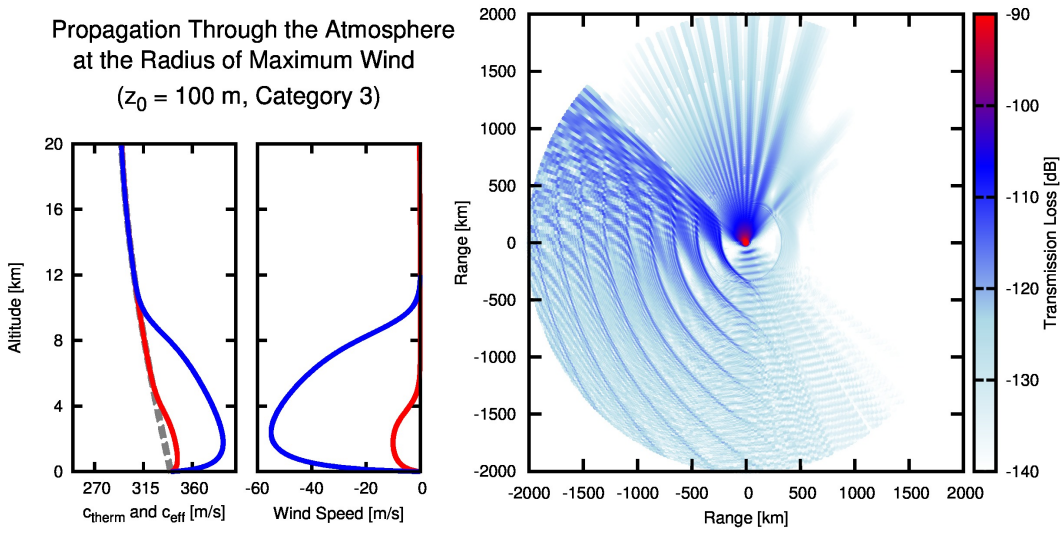

Fig. 41: The effective sound speed profiles (left) and arrival field (right) for propagation through the atmosphere at the radius of maximum winds in a direction east of the eye column of a Category 3 storm with boundary layer surface roughness increased to 100 meters.

From these results we can infer that the results of Chapter 3 are possible under the conditions that the storm winds are sufficiently strong or the wind gradients near the ocean surface are sufficiently weak that an efficient duct is produced. However, some care must be taken in using the predicted amplitudes of the refracted arrival since some fraction of the energy would be lost through the inefficiency of the boundary layer duct. These results also imply that there could be a minimum storm intensity, below which the boundary layer cannot form a sufficiently strong acoustic duct and energy will not be strongly refracted. Additional observations would be necessary to determine if a minimum storm intensity for ducting exists and what other conditions might influence the ducting efficiency.

APPENDIX C: EXPERIMENT DETAIL - ARRAY GEOMETRIES

APPENDIX C

EXPERIMENT DETAIL - ARRAY GEOMETRIES

In order to obtain sensor locations in appropriate units, the latitude and longitude coordinates each sensor recorded were converted to the new universal international map standard (UTM) coordinates. UTM divides the earth into 60 north-south zones each 6^o wide in longitude. Within each zone, distances are measured in Easting and Northing from the zone boundaries in meters. The relative UTM locations of the sensors in each array are listed in Tables 2 and 3. The array response for a plane wave incident on the array from the east (0 degrees) is shown in Fig. 42 and 43 for 2010 and 2011 respectively. This response is calculated using the Bartlett spatial spectra with a synthetic planewave incident at the selected azimuth and no noise.

Array Geometry: Croatan (2010)				
Sensor ID	GPS (Lat.)	GPS (Long.)	UTM (x)	UTM (y)
172	34.725675	76.958710	706 m	-434 m
200	34.733768	76.964311	210 m	473 m
213	34.726234	76.971874	-499 m	-349 m
214	34.729462	76.966509	0 m	0 m
Array Geometry: Francis Marion (2010)				
Sensor ID	GPS (Lat.)	GPS (Long.)	UTM (x)	UTM (y)
203	33.161155	79.746462	231 m	922 m
210	33.152862	79.749058	0 m	0 m
212	33.149289	79.746651	229 m	-393 m
216	33.158829	79.758561	-895 m	651 m
Array Geometry: McCoy (2010)				
Sensor ID	GPS (Lat.)	GPS (Long.)	UTM (x)	UTM (y)
99	34.933585	79.548829	-606 m	117 m
102	34.927326	79.538768	323 m	-564 m
148	34.932448	79.542213	0 m	0 m
202	34.936029	79.540514	149 m	399 m
Array Geometry: Ocala (2010)				
Sensor ID	GPS (Lat.)	GPS (Long.)	UTM (x)	UTM (y)
207	29.269756	81.685118	-883 m	-305 m
209	29.276640	81.676530	-45 m	452 m
215	29.272558	81.676042	0 m	0 m

Table 3: The array design in GPS coordinates and relative New Universal International Map Standard (UTM) for the deployments in 2010.

Array Geometry: Bass River (2011)				
Sensor ID	GPS (Lat.)	GPS (Long.)	UTM (x)	UTM (y)
71	39.64654	74.39501	519.0	-362.8
75	39.65386	74.40080	16.8	446.3
121	39.64684	74.40691	-502.3	-336.3
172	39.64984	74.40103	0.0	0.0
Array Geometry: Brookhaven National Laboratory (2011)				
Sensor ID	GPS (Lat.)	GPS (Long.)	UTM (x)	UTM (y)
67	40.87163	72.86021	0.0	0.0
84	40.86848	72.84649	1165.0	-321.3
137	40.86517	72.89490	-2906.2	-788.2
140	40.88063	72.85096	755.1	1017.8
166	40.88180	72.88631	-2226.9	1074.8
187	40.87166	72.88771	-2317.0	-53.1
Array Geometry: Croatan (2011)				
Sensor ID	GPS (Lat.)	GPS (Long.)	UTM (x)	UTM (y)
99	34.72606	76.97256	-659.3	-174.2
113	34.73328	76.96424	118.3	611.9
157	34.72774	76.96540	0.0	0.0
199	34.72573	76.95865	614.4	-235.1
Array Geometry: Francis Marion (2011)				
Sensor ID	GPS (Lat.)	GPS (Long.)	UTM (x)	UTM (y)
95	33.15994	79.75531	-332.7	367.1
110	33.15659	79.75179	0.0	0.0
235	33.15117	79.74872	293.6	-597.9
208	33.15871	79.74613	525.9	241.6
Array Geometry: McCoy (2011)				
Sensor ID	GPS (Lat.)	GPS (Long.)	UTM (x)	UTM (y)
55	34.93685	79.53912	360.0	556.0
87	34.92737	79.53861	422.1	-494.5
125	34.93188	79.54315	0.0	0.0
182	34.93353	79.55127	-744.6	171.2
Array Geometry: Ocala (2011)				
Sensor ID	GPS (Lat.)	GPS (Long.)	UTM (x)	UTM (y)
37	29.27001	81.67060	525.4	-288.6
185	29.27655	81.67615	-9.4	439.6
246	29.26987	81.67866	-257.1	-300.1
252	29.27259	81.67603	0.0	0.0
Array Geometry: Pachaug (2011)				
Sensor ID	GPS (Lat.)	GPS (Long.)	UTM (x)	UTM (y)
178	41.61997	71.87594	-550.6	420.7
194	41.61635	71.86917	0.0	0.0
237	41.61164	71.86740	130.8	-528.3

Table 4: The array design in GPS coordinates and relative New Universal International Map Standard (UTM) for the deployments in 2011.

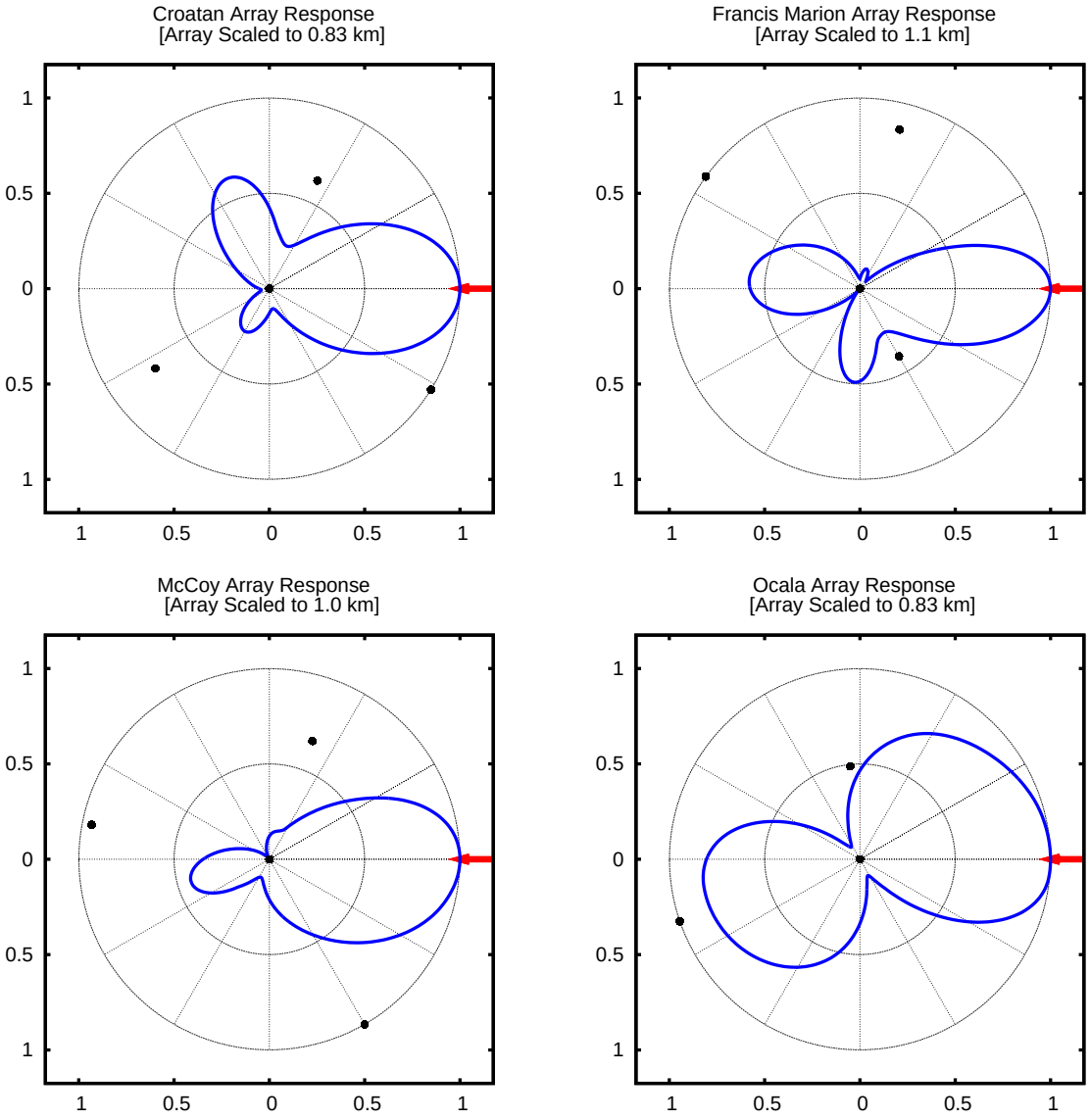

Fig. 42: The Bartlett spatial spectra response for the deployments in 2010.

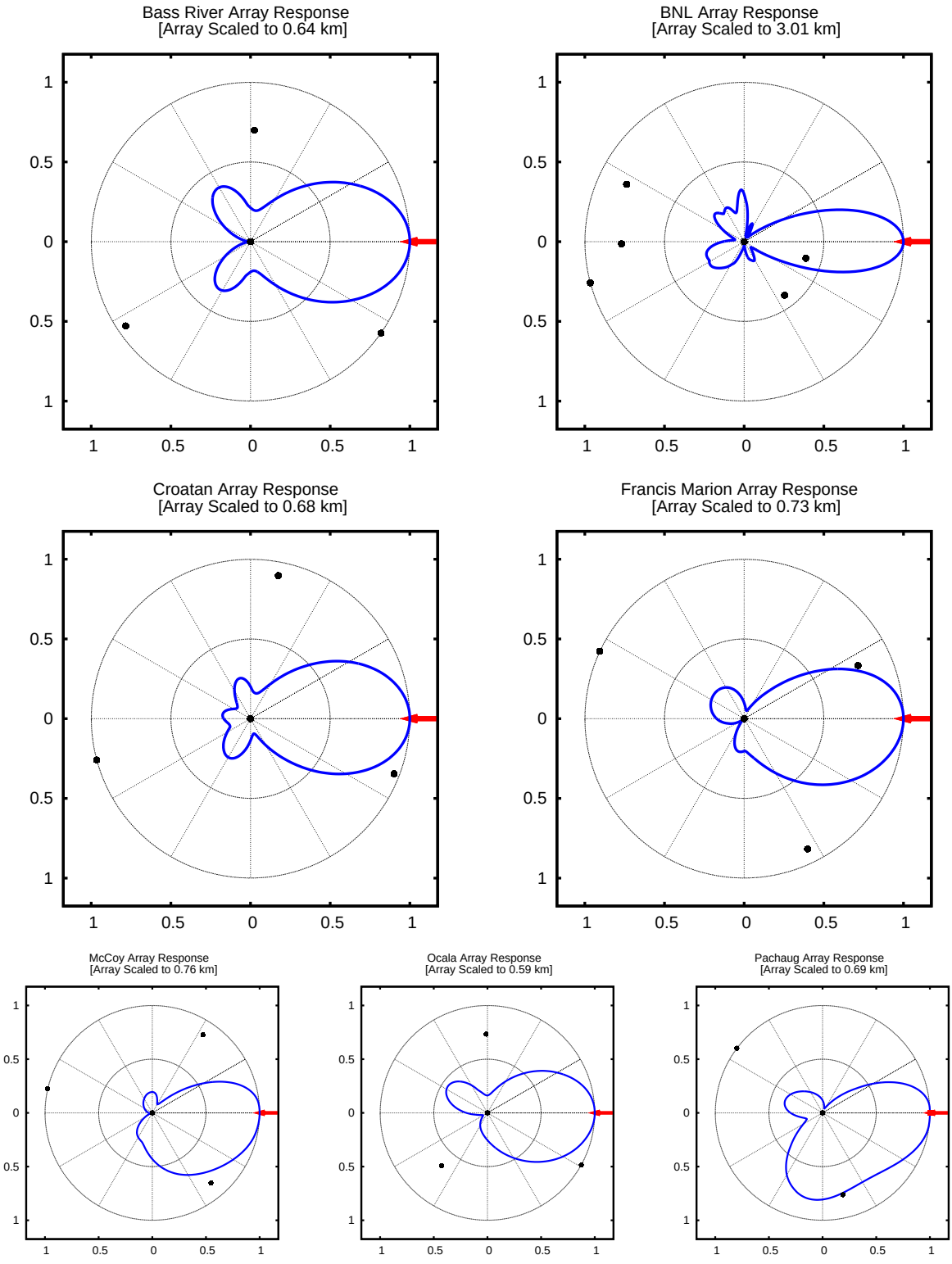

Fig. 43: The Bartlett spatial spectra response for the deployments in 2011.

VITA

Philip Blom

University of Mississippi
Jamie Whitten National Center for Physical Acoustics
1 Coliseum Dr, MS 38677

Personal

Born November 2, 1983
United States Citizen

Education

- Doctor of Philosophy in Physics, University of Mississippi, 2013
  - Thesis: Interaction of the Cyclonic Winds with the Infrasonic Signal Generated by a Large Maritime Storm
- Master of Science in Physics, University of Mississippi, 2010
  - Thesis: Analysis and Use of Anomalous Fast Arrivals in Impulse Propagation in the Nocturnal Boundary Layer
- Bachelor of Science in Physics, University of Louisville, 2006
  - Minors: Mathematics, Philosophy

Professional Associations

- Acoustical Society of America
- American Geophysical Union

Awards

- Graduate Achievement Award in Physics and Astronomy; University of Mississippi, 2012
- Zdravko Stipcevic Honors Scholarship; University of Mississippi, 2007 - 2012
- Graduated Cum Laude; University of Louisville, 2006
- Trustees Academic Scholarship and Maximum KEES Academic Scholarship; University of Louisville, 2002
- Graduated Salutatorian; Heritage Academy, 2002

Employment

- University of Mississippi 2007–2013.
- Center of Science and Industry (COSI) 2007.
- University of Louisville, 2005–2006.

Publications

Journal Articles

- Impulse Propagation in the Nocturnal Boundary Layer: Analysis of the Geometric Component, coauthor: Roger Waxler, *J. Acoust. Soc. Am., Vol 131 (5), p 3680-3690 (2012)*

Academic

- Analysis and Use of Anomalous Fast Arrivals in Impulse Propagation in the Nocturnal Boundary Layer, 2010, *Masters Thesis, University of Mississippi.*
- Interaction of the Cyclonic Winds with the Microbarom Signal Generated by a Large Maritime Storm, 2013, *Ph.D. Dissertation Thesis, University of Mississippi.*